

## Aerosol modelling : spatial distribution and effects on radiation

**Citation for published version (APA):**

Henzing, J. S. (2006). *Aerosol modelling : spatial distribution and effects on radiation*. [Phd Thesis 2 (Research NOT TU/e / Graduation TU/e), Applied Physics and Science Education]. Technische Universiteit Eindhoven. <https://doi.org/10.6100/IR601939>

**DOI:**

[10.6100/IR601939](https://doi.org/10.6100/IR601939)

**Document status and date:**

Published: 01/01/2006

**Document Version:**

Publisher's PDF, also known as Version of Record (includes final page, issue and volume numbers)

**Please check the document version of this publication:**

- A submitted manuscript is the version of the article upon submission and before peer-review. There can be important differences between the submitted version and the official published version of record. People interested in the research are advised to contact the author for the final version of the publication, or visit the DOI to the publisher's website.
- The final author version and the galley proof are versions of the publication after peer review.
- The final published version features the final layout of the paper including the volume, issue and page numbers.

[Link to publication](#)

**General rights**

Copyright and moral rights for the publications made accessible in the public portal are retained by the authors and/or other copyright owners and it is a condition of accessing publications that users recognise and abide by the legal requirements associated with these rights.

- Users may download and print one copy of any publication from the public portal for the purpose of private study or research.
- You may not further distribute the material or use it for any profit-making activity or commercial gain
- You may freely distribute the URL identifying the publication in the public portal.

If the publication is distributed under the terms of Article 25fa of the Dutch Copyright Act, indicated by the "Taverne" license above, please follow below link for the End User Agreement:

[www.tue.nl/taverne](http://www.tue.nl/taverne)

**Take down policy**

If you believe that this document breaches copyright please contact us at:

[openaccess@tue.nl](mailto:openaccess@tue.nl)

providing details and we will investigate your claim.

# **Aerosol Modelling**

## **Spatial Distribution and Effects on Radiation**

PROEFSCHRIFT

ter verkrijging van de graad van doctor aan de  
Technische Universiteit Eindhoven, op gezag van de  
Rector Magnificus, prof.dr.ir. C.J. van Duijn, voor een  
commissie aangewezen door het College voor  
Promoties in het openbaar te verdedigen  
op maandag 6 maart 2006 om 16.00 uur

door

**Jeroen Sebastiaan Henzing**

geboren te Alkemade

Dit proefschrift is goedgekeurd door de promotoren:

prof.dr. H.M. Kelder

en

prof.dr.ir. G.J.F. van Heijst

Copromotor:

dr. P.F.J. van Velthoven

**Cover:** Photos of various mixtures of atmospheric aerosol taken with an electronic microscope. By courtesy of Olga Mayol-Bracero, Joachim Huth and Günter Helas, MPI for Chemistry, Mainz, Germany.

Druk: Universiteitsdrukkerij Technische Universiteit Eindhoven

Omslagontwerp: Paul Verspaget, verspaget.bruinink@wxs.nl

CIP- DATA LIBRARY TECHNISCHE UNIVERSITEIT EINDHOVEN

Henzing, J.S.

Aerosol modelling : spatial distribution and effects on radiation / by J.S.

Henzing. – Eindhoven : Technische Universiteit Eindhoven, 2006. –

Proefschrift.

ISBN-10: 90-386-2431-X

ISBN-13: 978-90-386-2431-0

NUR 932

Trefwoorden: aërosolen / klimatologie / atmosferische straling / troposfeer / atmosferische chemie

Subject headings: aerosol / climatology / atmospheric radiation / troposphere / atmospheric chemistry

# Contents

<b>Samenvatting</b>	<b>7</b>
<b>1. General introduction</b>	<b>13</b>
1.1 Background and motivation	13
1.2 This thesis	14
<b>2. Aerosols and climate</b>	<b>17</b>
2.1 Radiative forcing	17
2.1.1 Well-mixed greenhouse gases	18
2.1.2 Scattering aerosols	18
2.1.3 Absorbing aerosols	19
2.2 Precipitation – hydrological cycle	22
<b>3. The effect of aerosols on the downward shortwave irradiances at the surface – Measurements versus calculations with modtran4.1</b>	<b>27</b>
3.1 Introduction	27
3.2 Experimental approach	28
3.2.1 Selection of cloudless days	29
3.2.2 Instrumentation	30
3.3 Surface irradiance measurements	32
3.3.1 Direct irradiance	32
3.3.2 Diffuse irradiance	33
3.3.3 Global irradiance	35
3.4 Radiative transfer model and its input data	35
3.4.1 modtran4.1 description	35
3.4.2 Overview of required input data	35
3.4.2.1 Solar irradiance	35
3.4.2.2 Gases and thermal structure	36
3.4.2.3 Surface albedo	36
3.4.2.4 Aerosol characteristics	36
3.4.3 Measurements of model input data	38
3.4.3.1 Spectral aerosol optical thickness	38
3.4.3.2 Aerosol absorption coefficient	38
3.4.3.3 Aerosol scattering coefficient	39
3.4.3.4 Aerosol asymmetry parameter	39
3.4.3.5 Water vapor column	40
3.4.3.6 Ozone column	41
3.4.3.7 Surface albedo	41
3.5 Sensitivity study of model calculations of shortwave irradiances on cloudless days	42
3.5.1 modtran4.1 calculations	42
3.5.2 Sensitivity study	43
3.5.2.1 Sensitivity to aerosol optical thickness errors	44
3.5.2.2 Sensitivity to absorption coefficient errors	45
3.5.2.3 Sensitivity to scattering coefficient errors	48

3.5.2.4 Sensitivity to asymmetry parameter errors	48
3.5.2.5 Sensitivity to water vapor column errors	49
3.5.2.6 Sensitivity to surface albedo errors	49
3.5.3 Total error in the calculated irradiances	49
3.6 Comparison between modeled and measured downward shortwave irradiances on cloudless days	50
3.6.1 Comparison strategy	50
3.6.2 Direct irradiances	50
3.6.3 Diffuse irradiances	50
3.6.4 Global irradiances	50
3.6.5 Discussion of possible sources of the disagreement between calculated and measured irradiances	51
3.6.5.1 Spectral aerosol optical thickness	51
3.6.5.2 Surface albedo	53
3.6.5.3 Zero offset of pyranometer measurements	53
3.6.5.4 Vertical aerosol distribution	53
3.7 Discussion of a possible agreement between modeled and measured diffuse irradiances	54
3.8 Conclusions	57
<b>4. A parameterization of size resolved below cloud scavenging of aerosols by rain</b>	<b>59</b>
4.1 Introduction	59
4.2 Below cloud scavenging coefficient	60
4.2.1 Explicit calculation	60
4.2.1.1 Rain droplet velocity	60
4.2.1.2 Rain droplet size distribution	60
4.2.1.3 Raindrop-aerosol collection efficiency	61
4.2.2 Parameterization	61
4.3 Global chemistry transport model TM4	63
4.3.1 Sea salt source function	63
4.3.2 Aerosol sinks	65
4.3.2.1 Large scale cloud systems	65
4.3.2.2 Dry deposition	66
4.3.2.3 Convective cloud systems	67
4.4 Results	67
4.4.1 Emission, load, and lifetime	67
4.4.2 Partitioning between below-cloud scavenging and other sinks	69
4.5 Remaining uncertainties	70
4.5.1 Rain droplet spectrum	70
4.5.2 Particle humidity growth	71
4.5.3 Precipitation and evaporation	71
4.6 Conclusions	72
<b>5. Global aerosol modeling with TM4 – application to the aerosol optical depth over Europe</b>	<b>75</b>
5.1 Introduction	75
5.2 Transport Model TM4	75
5.2.1 Emissions	75
5.2.2 Chemistry	76

---

5.3 Aerosol module	76
5.3.1 Aerosol sources	76
5.3.2 Aerosol sinks	77
5.3.2.1 Dry deposition	78
5.3.2.2 In-cloud scavenging and convective scavenging	78
5.3.2.3 Below-cloud scavenging	79
5.3.3 Aerosol optical parameters	80
5.3.3.1 Hydrophobic carbonaceous aerosol	80
5.3.3.2 Internal mixtures of carbonaceous and secondary inorganic aerosols	81
5.3.3.3 Pure secondary inorganic aerosol	82
5.3.3.4 Sea salt aerosol	83
5.4 Application to Europe – comparison to observations	86
5.4.1 Comparison to AERONET observations	89
5.4.2 Sensitivity studies	91
5.4.2.1 Sources	91
5.4.2.2 Water vapor redistribution	92
5.4.2.3 Sources and water vapor redistribution	93
5.5 Discussion and conclusions	95
<b>6. Perspectives on the assimilation of aerosol optical depth – development of an aerosol assimilation system for TM4 and application to Europe</b>	<b>99</b>
6.1 Introduction	99
6.2 Transport model TM4 aerosol module	99
6.3 Assimilation system	99
6.3.1 Satellite observation error	101
6.3.2 Model error	102
6.4 Application of the system	103
6.4.1 Satellite observations	103
6.4.2 Results and discussion	107
6.4.2.1 Case 1: March 2000	107
6.4.2.2 Case 2: May 2000	107
6.4.2.3 General results	107
6.5 Discussion and conclusions	110
<b>7. Summary and conclusions</b>	<b>111</b>
<b>8. Outlook and recommendations</b>	<b>115</b>
<b>References</b>	<b>117</b>
<b>List of acronyms and abbreviations</b>	<b>135</b>
<b>Dankwoord</b>	<b>137</b>
<b>Curriculum vitae</b>	<b>139</b>



# Samenvatting

## Verklaring van de titel van dit proefschrift

De titel van dit proefschrift laat zich vertalen als: “Aërosolmodellering – de ruimtelijke verdeling en de effecten op straling”. Een aërosol is gedefinieerd als een nevel waarin kleine vaste en vloeibare deeltjes zweven. In de klimaatwetenschap wordt vaker gesproken over aërosolen, aërosoldeeltjes, of worden met het woord “aërosol” alleen de deeltjes bedoeld. In dit proefschrift wordt op twee manieren aan *aërosolmodellering* gedaan. Op basis van waarnemingen wordt een *aërosolmodel* gemaakt dat als basis dient voor stralingstransport berekeningen. Met deze berekeningen worden de *aërosoleffecten op de instraling* van de zon aan de grond onderzocht. Het andere *aërosolmodel* dat wordt ontwikkeld in dit proefschrift heeft als doel de *ruimtelijke verdeling* van aërosol te kunnen simuleren op mondiale schaal.

## Achtergrond en motivatie

Weer en klimaat zijn van groot belang voor het leven op Aarde. Het weer beïnvloedt ons leven dagelijks en klimaatveranderingen kunnen onze gezondheid, voedselproductie en het algemeen welbevinden in gevaar brengen. Het is daarom essentieel om het klimaat te begrijpen en om betrouwbare verwachtingen van klimaatveranderingen te kunnen maken. Het klimaat kent continu veranderingen op alle tijdschalen. De laatste miljoen jaren hebben ijstijden en warme perioden elkaar afgewisseld, voornamelijk als gevolg van variaties in de baanparameters van de Aarde. De laatste tienduizend jaren lijken juist redelijk stabiel te zijn geweest. In recent onderzoek wordt gesuggereerd dat het klimaat op het noordelijke halfrond de laatste duizend jaar gekarakteriseerd wordt door een onregelmatige (bijv. Middeleeuws optimum en kleine ijstijd) maar gestage afkoeling, gevolgd door een sterke opwarming in de twintigste eeuw. Gebaseerd op deze analyses kent de opwarming vanaf de twintigste eeuw zijn gelijke niet in het laatste millennium; op geologische tijdschalen is een opwarming van deze grootte niet ongevoel. Reconstructies van klimaatgegevens hebben er echter toe geleid dat klimaatwetenschappers, die zijn aangesloten bij het internationale panel voor klimaatverandering (IPCC), concluderen dat het onwaarschijnlijk is dat de opwarming in de twintigste eeuw geheel natuurlijk is en dat de opwarming van de laatste vijftig jaar waarschijnlijk toe te schrijven is aan menselijke activiteiten.

Menselijke activiteiten zullen de atmosferische samenstelling in de toekomst blijven veranderen. Toenames van koolstofdioxide en andere broeikasgassen lijken onafwendbaar. De lange verblijftijd van de meeste broeikasgassen in de atmosfeer zorgt ervoor dat hun concentraties blijven toenemen, zelfs als effectieve maatregelen worden getroffen die hun emissies aanzienlijk verlagen. Microscopisch kleine atmosferische deeltjes komen in onze atmosfeer terecht door bronnen zoals opwaaiend stof en zeezout en door emissies van biogene vluchtige organische stoffen.



De concentraties van deze deeltjes zijn door activiteiten van de mens ook verhoogd boven de natuurlijke concentraties. De belangrijkste activiteit die leidt tot antropogene atmosferische deeltjes is het verbranden van fossiele brandstoffen. Bestaande emissiescenario's voor antropogene aerosolen voor de komende eeuw laten zowel toenames als afnamen zien, afhankelijk van veranderingen in het gebruik van fossiele brandstoffen en het succes van maatregelen om de uitstoot te beperken. De relatief korte verblijftijd van deeltjes in de atmosfeer heeft als gevolg dat lagere emissies snel gevolgd zullen worden door lagere concentraties. Ondanks de grote onzekerheid in emissiescenario's en in klimaatvariatiëën geïnduceerd door complexe interacties tussen atmosfeer, oceaan, land, ijs en biosfeer, laten de projecties voor de volgende eeuw een toename van de temperatuur zien. Het belang van aerosolen wordt duidelijk als de geprojecteerde temperaturen uit het laatste IPCC rapport worden vergeleken met die uit het vorige rapport. In het laatste rapport is de variatie tussen de verschillende projecties groter en zijn de geprojecteerde temperatuurstijgingen groter. De reden hiervoor is vooral dat in het laatste rapport de zwaveldioxide emissies veel lager worden geprojecteerd, waardoor ook de te verwachten concentratie van zwavelhoudende deeltjes veel lager uitkomt.

Betrouwbare scenario's voor klimaatveranderingen in de toekomst zijn essentieel voor beleidsondersteuning en politieke strategieën op de lange termijn. Een betrouwbare klimaatprojectie kan alleen gemaakt worden als het huidige klimaat en de rol van aerosolen daarin begrepen wordt en nauwkeurig gesimuleerd kan worden met modellen. Omdat de atmosferische circulatie primair wordt gedreven door de verdeling van zonne-energie, is het theoretische begrip van stralingstransport essentieel, en in het bijzonder de rol van aerosolen daarin. Het is daarom verontrustend dat zelfs de meest geavanceerde stralingstransportmodellen nog niet in staat zijn om de zonnestraling aan het oppervlak en de absorptie van zonnestraling in de atmosfeer nauwkeurig genoeg te berekenen. Een ander punt van aandacht is dat een recente vergelijkingsstudie tussen aerosolmodellen aanzienlijke verschillen in de gesimuleerde aerosolconcentraties laat zien, zelfs als de modellen dezelfde emissies als invoer gebruiken, en dat de gemodelleerde concentraties niet overeenkomen met onafhankelijke metingen binnen acceptabele grenzen. Mede gezien de onzekerheden rond aerosolen in stralingstransportberekeningen en het correct modelleren van atmosferische aerosolconcentraties, schat het IPCC de wetenschappelijke kennis met betrekking tot aerosol effecten op het klimaat nog steeds zeer laag in.

## Dit proefschrift

In dit proefschrift wordt een bijdrage geleverd aan de onderwerpen, die hierboven in algemene termen zijn besproken. De rol van aerosolen op de instraling van de zon aan het oppervlak wordt onderzocht door middel van processtudies op een beperkt aantal "wolkenvrije" dagen. De driedimensionale verdeling van aerosolen wordt verbeterd door de parametrisaties voor de verwijdering van atmosferisch aerosol te optimaliseren en door gebruik te maken van een assimilatietechniek.

In **Hoofdstuk 1** wordt, bij wijze van algemene inleiding, een kort overzicht gegeven van waargenomen en geprojecteerde klimaatveranderingen.

**Hoofdstuk 2** bevat de wetenschappelijke inleiding van dit proefschrift. De rol van aerosolen op *temperatuur* en de *hydrologische cyclus* wordt besproken. We maken

daarbij onderscheid tussen het directe aerosol effect, het indirecte aerosol effect en het semi-directe aerosol effect. Het directe aerosol effect betreft de directe interactie tussen aerosolen en zonnestraling. Weerkaatsing van zonlicht door aerosolen zal leiden tot een afname van de energie-inhoud van het deel van de atmosfeer waar ons weer zich afspeelt en absorptie van zonlicht door aerosolen zal leiden tot een toename van deze energie-inhoud. Aerosolen hebben een indirect effect door de prominente rol van aerosolen in de microfysica van wolken. Een verandering in aerosol concentraties leidt tot verandering in de optica van wolken (het eerste indirecte effect) maar ook tot een verandering in de ruimtelijke en temporele verdeling van wolken (het tweede indirecte effect). Het semi-directe effect betreft de verandering in wolken ten gevolge van veranderingen in de temperatuur opbouw van de atmosfeer door het directe aerosol effect. De verschillende aerosol effecten worden in hoofdstuk 2 besproken vanuit een conceptueel perspectief en door bespreking van bestaande literatuur.

Hoe de wereldgemiddelde *temperatuur* wordt beïnvloed door de verschillende aerosol effecten wordt traditioneel besproken door gebruik te maken van het concept van stralingsforcering. Essentieel uitgangspunt van dit concept is dat stralingsforcering ten gevolge van verschillende klimaatverstoringen een vergelijkbare klimaatrespons (temperatuur) hebben. In hoofdstuk 2 wordt geconcludeerd dat aan deze basis conditie niet voldaan kan worden voor de indirecte en semi-directe aerosol effecten. Het is daarom noodzakelijk om het klimaat te simuleren met mondiale circulatiemodellen waarin alle interacties tussen klimaat en aerosolen zijn meegenomen. Dit soort simulaties is tot op heden echter zeer schaars vooral omdat de mondiale driedimensionale verdeling van aerosolen nog niet met voldoende hoge kwaliteit gesimuleerd kan worden. Ondanks al deze onvolledigheden en onzekerheden is er een consensus dat aerosolen een netto koeling van het klimaat tot gevolg hebben, die de verwarming ten gevolge van in de atmosfeer aanwezige broeikasgassen ten dele compenseert.

Stralingsforcering is als concept onbruikbaar voor het voorspellen van de grootte en zelfs het teken van de veranderingen in de *hydrologische cyclus* veroorzaakt door aerosolen. In hoofdstuk 2 wordt de discussie over de invloed van aerosolen op de hydrologische cyclus daarom besproken vanuit een theoretisch oogpunt. Het is aannemelijk dat de atmosfeer meer waterdamp zal bevatten in een warmer klimaat. Een toename van waterdamp zal over het hele neerslagspectrum leiden tot intensere neerslag als er geen systematische veranderingen optreden in de dimensies and frequentie van weersystemen met neerslag. Bovendien, zal het vrijkomen van extra latente warmte waarschijnlijk leiden tot versterking van de meest intense neerslag systemen. Gebaseerd op fysische argumenten en ondersteunend bewijs van enkele case studies, wordt in hoofdstuk 2 aannemelijk gemaakt dat aerosolen neerslag zullen onderdrukken, met als uitzondering de meest intense neerslag systemen. Verhoogde concentraties broeikasgassen en aerosolen zorgen dus voor een verschuiving in het neerslagspectrum naar hogere intensiteiten. Het antwoord op de vraag of de totale hoeveelheid neerslag af- of toeneemt in een veranderend klimaat hangt af van de competitie tussen broeikasgassen (toename) en aerosolen (afname) en van de energie die beschikbaar is voor verdamping. Verdamping is op de lange termijn in balans met de neerslag en is dus de drijvende kracht achter de hydrologische cyclus. Toe- of afname van zoninstraling aan de grond heeft dus grote consequenties voor de hydrologische cyclus. De weinige modelstudies die alle relevante broeikasgassen en interacties tussen aerosolen en klimaat bevatten, laten een netto verzwakking van de

hydrologische cyclus zien. Waarnemingen bevestigen deze verzwakking niet. De verzwakking van de hydrologische cyclus door aërosolen is blijkbaar te sterk in deze simulaties. Het is belangrijk hier een verklaring voor te vinden omdat projecties voor de toekomst een beperkte waarde hebben als de achterliggende mechanismen niet goed zijn begrepen. Het is waarschijnlijk dat atmosferische aërosol concentraties in de toekomst zullen toenemen over grote delen van de wereld door de toename in energiegebruik. Toename van broeikasgasconcentraties is vrijwel zeker en deze toename is waarschijnlijk groter dan die van aërosolen door de lange atmosferische verblijftijd van de meeste broeikasgassen. De hypothese is daarom dat de competitie tussen aërosolen en broeikasgassen in de toekomst zal leiden tot een netto toename van de hydrologische cyclus.

**In hoofdstuk 3** wordt de analyse van metingen en modelberekeningen van de zonneinstraling aan het oppervlak gepresenteerd voor 18 zorgvuldig geselecteerde wolkenloze situaties in Nederland in het jaar 2000. Het zwaartepunt van de analyse ligt op de invloed van de optische en fysische eigenschappen van aërosolen op de simulatie van de directe en diffuse zonneinstraling op het oppervlak. De eigenschappen van aërosolen in de grenslaag zijn afgeleid van grondmetingen, waarbij is aangenomen dat al het aërosol zich in een goed gemengde atmosferische grenslaag bevindt. De simulaties van de instraling zijn uitgevoerd met het stralingstransport model MODTRAN4, versie 1.1. Uit de analyse blijkt dat metingen en modelberekeningen van de directe instraling met elkaar overeenkomen binnen de geschatte foutenmarges. Voor de diffuse instraling blijken er verontrustende verschillen tussen metingen en berekeningen te zijn. Het model overschat de gemeten diffuse instraling systematisch, waarbij de verschillen variëren van 7 tot 44  $\text{Wm}^{-2}$  (gemiddeld 25  $\text{Wm}^{-2}$ ). Op basis van de geschatte onzekerheid van 18  $\text{Wm}^{-2}$  in het verschil, blijkt dat voor 13 van de 18 situaties de overschatting significant is. Dit aantal neemt af wanneer instrumentele fouten (bijvoorbeeld pyranometer zero-offset) en alternatieven voor modelinvoer (bijvoorbeeld met betrekking tot de golflengte afhankelijkheid van de oppervlakte reflectie) in beschouwing worden genomen. Hoe het ook zij, de gepresenteerde analyse wijst op een persistente en significant positief verschil tussen het model en metingen van de diffuse instraling. De grootte van het verschil bedraagt typisch 1-4% van de inkomende irradiantie aan de top van de atmosfeer. In hoofdstuk 3 wordt gesuggereerd dat de reden van het verschil gezocht moet worden in de aanwezigheid van ultrakleine absorberende deeltjes, die niet werden waargenomen door het instrument dat werd gebruikt om de absorptie van aërosol te meten. Een andere mogelijkheid is dat deze kleine deeltjes niet aan het oppervlak voorkomen, ten gevolge van droge depositie, maar wel hogerop in de grenslaag, waar zij bedragen aan de totale extinctie.

**In hoofdstuk 4** wordt een parametrisatie ontwikkeld voor de verwijdering van aërosolen door vallende regendruppels. De verwijderingscoëfficiënten zijn expliciet berekend als een functie van de deeltjesgrootte en de neerslagintensiteit waarbij de volledige interactie tussen het spectrum van regeldruppels en aërosolen is meegenomen. De uiteindelijke parametrisatie is een eenvoudige en nauwkeurige fit door de berekende verwijderingscoëfficiënten. De parametrisatie is toegepast in het mondiale chemie-transportmodel TM4 en het relatieve belang van de verwijdering van aërosolen door vallende regendruppels ten opzichte van andere verwijderingsmechanismen is onderzocht voor zeezoutaërosol. Gebaseerd op een simulatie van een heel jaar (het jaar 2000), vinden we dat vallende regendruppels

verantwoordelijk zijn voor 12% van de totale verwijdering van grof zeezout (aërosolen met een straal groter dan 1 micrometer). Op gematigde breedtegraden van beide halfronden is de relatieve bijdrage van vallende regendruppels op de totale verwijdering ongeveer 30%, met regionale maxima groter dan 50%. Vallende regendruppels reduceren de gemiddelde atmosferische verblijftijd van grof zeezout (ongeveer 2 dagen) met 13% in onze simulaties. Ondanks de grote onzekerheid in neerslag, relatieve vochtigheid en water opname door zeezout aërosolen, concluderen we in hoofdstuk 4 dat vallende regendruppels waarschijnlijk een belangrijke bijdrage leveren aan de verwijdering van grof zeezout en dat dit proces niet verwaarloosd kan worden wanneer de aërosolgrootte verdeling wordt gemodelleerd.

**In hoofdstuk 5** wordt het aërosol model dat in hoofdstuk 4 werd gebruikt verder ontwikkeld zodat simulatie van de optische dikte van het aërosol mogelijk wordt gemaakt. De modelresultaten worden vergeleken met waarnemingen boven Europa voor het jaar 2000. De gemiddelde gesimuleerde aërosol optische dikte (0.17) is 15% lager dan de gemiddelde waargenomen aërosol optische dikte. De hoge ruimtelijke variabiliteit van atmosferisch waterdamp, die niet goed wordt opgelost in ons model, wordt aangedragen als mogelijke verklaring voor dit verschil. De relatie tussen de massa en de optische dikte van aërosol is sterk niet-lineair, als gevolg van opname van waterdamp. Voor een perfect gesimuleerde aërosol massa leidt de homogene verdeling van waterdamp in model gridcellen tot een systematische onderschatting van de aërosol optische dikte. Dit effect wordt belangrijker voor toenemende relatieve vochtigheid. Een andere mogelijke verklaring voor de onderschatting van de gemiddelde optische dikte is de manier waarop verdamping is meegenomen in het model. Neerslag die in wolken wordt gevormd, wordt geschaald met de neerslag die uiteindelijk de grond bereikt. Impliciet betekent dit dat aërosolen door verdamping in de wolk weer vrijkomen, waar ze onderhevig blijven aan verwijdering door vorming van regendruppels. In de echte atmosfeer zal veel van de verdamping onder de wolk plaatsvinden, waar verwijdering door vallende regendruppels veel minder effectief is. De variantie van de gesimuleerde aërosol optische dikte is kleiner dan de variantie van de door AERONET waargenomen aërosol optische dikte. We suggereren dat de grove ruimtelijke resolutie van het model bijdraagt aan de onderschatting. Middeling van aërosol massa concentraties over grote gebieden zorgt voor een nivellering van extreme waarden.

**In hoofdstuk 6** wordt een systeem voor de assimilatie van aërosol optische dikte ontwikkeld. Het systeem is toepast over Europa waarbij gebruik is gemaakt van ATSR-2 waarnemingen. Gemiddeld leidt de assimilatie tot hogere gesimuleerde aërosol optische diktes, zodat gesimuleerde waarden beter overeenkomen met onafhankelijke aërosol optische dikte waarnemingen (AERONET). De correlatie tussen deze twee tijdreeksen neemt echter niet toe door de assimilatie. Als een mogelijke verklaring hiervoor wordt aangedragen dat de assimilatie van aërosol optische dikte misschien niet de beste manier is om gesimuleerde aërosol concentraties te verbeteren. De variabiliteit van de aërosol optische dikte wordt voor een belangrijk deel bepaald door de ruimtelijke en temporele variabiliteit van waterdamp. Onzekerheden in de verdeling van waterdamp leiden tot grote onzekerheden in de gesimuleerde aërosol optische dikte. Een verschil tussen gesimuleerde en geassimileerde aërosol optische dikte leidt tot een aanpassing van de aërosol massa. Wanneer de gesimuleerde optische dikte afwijkt van de echte waarde als een gevolg van fouten in de relatieve vochtigheid in plaats van afwijkingen in de

gesimuleerde aërosol massa concentraties, dan is de aanpassing onterecht. De verbetering van de gesimuleerde aërosol optische dikte is ook teleurstellend omdat de kwaliteit van de ATSR-2 data beperkt is. De correlatie tussen alle gelijktijdige grondwaarnemingen en satellietwaarnemingen is verwaarloosbaar (0.03). We laten in hoofdstuk 6 zien dat deze zwakke correlatie niet het gevolg is van het samenstellen van super-observaties uit de hoge resolutie data. De correlatie van de  $0.1^\circ \times 0.1^\circ$  dataset is ook zwak (0.13). Als we er vanuit gaan dat het grootste deel van het probleem met waterdamp wordt opgelost als de simulaties met een hogere horizontale resolutie worden gedaan, is het te verwachten dat aërosolsimulaties verbeteren door de assimilaties van aërosol optische dikte wanneer in de toekomst betere waarnemingen beschikbaar komen.

# 1

## General introduction

### 1.1 Background and motivation

Weather and climate have a profound influence on life on Earth. They are part of the daily experience of human beings and climate changes directly endanger health, food production and well-being. Understanding and predicting climate change is therefore of utmost importance. Climate varies naturally on all time-scales. During the last million years or so, glacial periods and interglacials have alternated as a result of variations in the Earth's orbital parameters. The last 10,000 years appear to have been relatively stable. Recent analyses suggest that the Northern Hemisphere climate of the past 1,000 years was characterized by an irregular (e.g. the medieval Climate Optimum, the Little Ice Age) but steady cooling, followed by a strong warming during the 20<sup>th</sup> century. Based on these analyses, the warming of the late 20<sup>th</sup> century appears to have been unprecedented during the millennium, but the warming is not uncommon on geological timescales. However, based on reconstructions of climate data, the Intergovernmental Panel on Climate Change (IPCC, 2001) concludes that it is unlikely that the warming during the 20<sup>th</sup> century is entirely natural in origin and that most of the observed warming over the last 50 years is likely attributable to human activities.

Human influences will continue to alter the atmospheric composition throughout the 21<sup>st</sup> century. Increases in CO<sub>2</sub> and other greenhouse gases are virtually certain. The long atmospheric lifetime of most greenhouse gases ensures that burdens will further increase above natural levels even if effective measures are taken to lower the emissions considerably. Levels of microscopic-small atmospheric particles that arise from natural sources such as wind-borne dust, sea salt and emission of biogenic volatile organic compounds, are also raised above natural levels by human activities. The main activities responsible for anthropogenic aerosols are the combustion of fossil fuels and biomass. Emitted directly as particles (primary aerosols) or formed in the atmosphere by conversion of gaseous precursors (secondary aerosols), these so called aerosol particles range in size from a few nanometers to tens of micrometers. Existing anthropogenic emission scenarios of aerosols and their precursor gases for the coming century include the possibility of either increases or decreases, depending on the extent of fossil fuel use and policies to abate polluting emissions. Aerosol particles have relatively short lifetimes, as a result lower emissions almost instantaneously lead to lower atmospheric burdens. Despite, large uncertainties in emission scenarios and in climate fluctuations induced by complex interactions between the atmosphere, ocean, land, cryosphere, and biosphere, global temperatures

are projected to rise in the coming century under all IPCC scenarios (IPCC, 2001). The important role of aerosol particles becomes apparent when projected temperatures of the IPCC Third Assessment Report (TAR) are compared to the projections of the Second Assessment Report (SAR). In the TAR a wider range and higher projected temperature increases are found as compared to the SAR due primarily to the lower projected sulfur dioxide emissions, which eventually lead to the formation of sulfate-containing aerosol particles.

Reliable scenarios for future climate change are essential for long term policy strategies. A reliable climate projection can only be made if the current climate and the role of aerosols therein is well-understood and can be simulated accurately with models. Since atmospheric circulation is primarily governed by the distribution of absorbed solar radiation at the surface, the theoretical understanding of radiative transfer is of crucial importance. It is therefore of great concern that even the most sophisticated radiative transfer models cannot predict the surface irradiance and the absorption of solar radiation within the atmosphere correctly as yet (Fouquart et al., 1991; Kinne et al., 1998; Barker et al., 2003). Another point of concern is that recent aerosol model intercomparisons such as AeroCom (AeroCom, 2005; Textor et al., 2005) show considerable differences between predicted aerosol loadings even when using same emissions and that modeled fields do not agree with observations within acceptable limits. In view of the difficulties with radiative transfer and the prediction of atmospheric aerosol loadings, the level of scientific understanding of the effects of aerosols on climate is rated very low (IPCC, 2001). This dissertation contributes to both important issues. The role of aerosols on the downward shortwave irradiances at the surface is investigated by means of a process study on a limited number of days and the prediction of the global three dimensional distributions of aerosol particles is improved by the use of an assimilation technique and improved parameterizations of removal mechanisms.

## 1.2 This thesis

Atmospheric aerosol particles directly influence the distribution of energy within our atmosphere by scattering and absorbing (mainly) solar radiation. Through their role as cloud condensation nuclei, atmospheric aerosol particle concentrations critically affect the droplet number and ice particle concentrations within clouds thereby determining cloud optical properties. Moreover, the abundance of droplet number and ice particle concentrations is crucial with respect to cloud lifetime and the timing of the onset of precipitation. Changes in precipitation and cloud extent directly impact the global hydrological cycle and subsequently impact local water resources and regionally change atmospheric dynamics driven by latent and sensible heat flux. In chapter 2 of this thesis an overview of current understanding of aerosol-climate interactions is given.

The fact that radiation transfer models cannot predict the surface irradiance and the absorption of solar radiation within the atmosphere correctly even for the relatively simple cloud-free case, has led to the suggestion that an anomalous absorber is present in our atmosphere (Kato et al., 1997; Halthore et al., 1998). As a narrowband gaseous absorber is unlikely to have remained undetected (Solomon et al., 1998; Mlawer et al., 2000), it is necessary to explore the possibility that aerosols could be

responsible for the missing absorption. To do so, we carefully selected absolutely cloud-free days on which we measured all physical and optical aerosol characteristics that are relevant for climate. The aerosol characteristics, together with other measured radiatively active gaseous species, were used as input for a state-of-the-art radiation transfer model in order to accurately obtain calculated surface irradiances. Finally, the calculated irradiances were compared to downward solar irradiances measured at the surface. The results of this comparison are included in chapter 3 of this thesis.

The importance of particle size to the behavior and effects of atmospheric aerosol is well known, e.g. scattering and absorption of solar radiation by aerosols is highly dependent on the particle size, the impact of aerosols on cloud properties is strongly size dependent, and the hygroscopic growth of particles depends strongly on the actual size of the particles. Size resolved aerosol modeling is therefore expected to become increasingly important in the future. Particle sizes are determined by their emission sources, and they are modulated by coagulation, cloud-cycling, and size dependent removal mechanisms. An important modulator is the size dependent scavenging of aerosol particles by falling hydrometeors. In chapter 4 a parameterization for the scavenging of aerosol particles by falling rain droplets is developed. The parameterization provides the scavenging coefficient as a function of particle size and precipitation intensity. The parameterization is directly applicable to most models that estimate atmospheric aerosol concentrations.

To study or estimate the climatic impact of aerosols, the three dimensional global distribution of aerosol must be known continuously in time. Surface networks cannot provide this information since they do not have a sufficient global coverage. Databases that contain aerosol products retrieved from satellite observed radiances, do not have continuous global coverage either as pixels are contaminated with clouds, satellites are geo-stationary or they do not cover the globe with sufficient temporal resolution, or the retrieval algorithms are only available over certain surface types. Aerosol modeling can provide the wanted three dimensional distribution of aerosols continuously in time. In Chapter 5, the development of such an aerosol model, based on an existing global chemistry transport model, is described. The model is run for the year 2000 and simulated fields are compared with independent ground based observations.

In the general introduction, the scientific understanding of the role of aerosols in our climate is rated very low. Simulations of aerosol concentrations and aerosol optical properties are often qualitatively poor. A combination of (global satellite) observations and global modeling may therefore be a good alternative to optimally benefit from both observations and modeling. Of course, the assimilation itself cannot be viewed as a substitute for improvements of the aerosol model. For climate projections a comprehensive model is needed that predicts reliable aerosol concentrations. However, assimilation can serve as a powerful diagnostic tool for characterizing errors in the model physics through careful analysis of the corrections applied by assimilation as is common in weather forecast models. For the global chemistry transport model TM4 a data assimilation system has been developed. In chapter 6, the data assimilation scheme is described and applied to Europe for the year 2000.



Chapter 7 contains the conclusions of this thesis and model improvements are suggested.

Apart from the important climatic impact of aerosols, the interest in aerosols is also great because of their effect on human health. Epidemiological studies show that an increase in aerosol mass concentration by  $10 \mu\text{g m}^{-3}$  results in an increase of 0.5-1.5% in premature total mortality in case of short term/episodic exposure, and in an increase up to 5% in premature total mortality in case of long term/life long exposure (Wilson and Spengler, 1996). As yet, there is no indication which physical or chemical aerosol characteristic is responsible for these effects. However, recent research seems to indicate that the total mass of particles with aerodynamic diameters smaller than  $2.5 \mu\text{m}$  (PM<sub>2.5</sub>) is associated with cardio-vascular diseases and the total mass of particles smaller than  $10 \mu\text{m}$  (PM<sub>10</sub>) is associated with respiratory responses (Wyzga, 2002). The effect of aerosols on human health is outside the subject of this thesis. However, in chapter 8, I will shortly discuss the potential contribution of the developed model to this important health issue.

# Aerosols and climate

Anthropogenic activities have led to changes in the composition of the atmosphere. Increased levels of atmospheric gases that are mainly active in the longwave part of the energy spectrum are responsible for the well-known enhancement of the natural greenhouse effect. Increased levels of atmospheric aerosol particles lead to increased reflectivity of the planetary boundary layer. This whitehouse effect of aerosols is important as it counteracts the warming caused by increased levels of greenhouse gases. However, discussing the effect of aerosol via its whitehouse effect does not convey all aerosol-climate interactions. Some types of aerosols also warm the atmosphere locally by absorption of direct sunlight and trapping solar radiation that is reflected at the surface thereby reducing the amount of solar radiation that is reflected back to space. The ratio of scattering to absorption is critical for the net (temperature) effect. Aerosols also play a key role in cloud microphysics by acting as cloud condensation nuclei and ice nuclei. Moreover, changes in local heating rates caused by absorbing aerosols have important implications for various cloud properties. All of the (potential) aerosol impacts discussed hereabove, change the distribution of radiation in the earth's atmosphere and consequently change the temperature. Through their impact on clouds, aerosols also have the potential to change precipitation characteristics. Arguably, the impact of precipitation changes, that are likely to occur in our changing climate, has a larger societal impact than changes in surface temperature. Therefore, it is of utmost importance to understand and quantify changes in the hydrological cycle. This chapter deals with the question how aerosols impact on precipitation and temperature, the latter is (most conveniently) discussed using the concept of radiative forcing.

## 2.1 Radiative forcing

Changes in the amount of radiatively active atmospheric constituents, incoming solar radiation, and surface reflectance, perturb the radiation balance at the surface, tropopause, and top of the atmosphere. These imbalances in the radiation budget lead to changes in climate parameters and thus eventually result in a new equilibrium state of the climate system. The stratosphere adjusts to imposed radiative perturbations much faster (few months) than the surface-troposphere system (decades) and it is the remaining 'adjusted forcing' (rather than the 'instantaneous forcing') that is a relevant indicator of the climate response (Hansen et al., 1997). The Intergovernmental Panel on Climate Change - IPCC (Ramaswamy et al., 2001) therefore defines the radiative forcing of the surface-troposphere system as the change in net irradiance at the tropopause caused by a perturbation, after allowing for stratospheric temperatures to

re-adjust to radiative-dynamical equilibrium, but with surface and tropospheric temperatures and state held fixed at the unperturbed values.

### 2.1.1 Well-mixed greenhouse gases

For small perturbations in well-mixed greenhouse gases, climate model experiments indicate that the equilibrium change in global-mean surface temperature ( $\Delta T_s$ ) is approximately linearly related to the radiative forcing ( $\Delta F$ ) so that:  $\Delta T_s = \lambda \Delta F$ , where  $\lambda$  is the climate sensitivity parameter. Although the value of parameter  $\lambda$  can vary from one model to another, within each model  $\lambda$  is found to be remarkably constant for long-lived greenhouse gas radiative perturbations. Owing to the near-invariance of  $\lambda$ , comparison of different forcings is of great value as it directly provides the relative importance of the forcing agents considered. Moreover, experiments involving greenhouse gases tend to confirm that individual forcings can be linearly added to obtain the total surface temperature response to the sum of forcings (Haywood et al., 1997). Another practical benefit of the radiative forcing concept is that the need to actually run and analyse equilibrium-response General Circulation Model (GCM) simulations can be bypassed. Instead simpler models, e.g. Chemistry Transport Models (CTMs), together with more sophisticated Radiation Transport Models (RTMs) can be applied to obtain radiative forcing estimates.

### 2.1.2 Scattering aerosols

The concept of radiative forcing has proven its usefulness for changes in well-mixed greenhouse gases and spectrally uniform solar constant variations. Therefore, it is appealing to apply the concept also to aerosols. The introduction or increase in atmospheric (back) scattering by aerosols leads to a change in planetary albedo and the resulting effect on climate may be similar to that of a reduction in solar irradiance. Indeed, using various GCMs, examinations of the applicability of the concept of radiative forcing for scattering aerosols such as sulfate confirm climate sensitivities similar to those for greenhouse gases, and even the linear additivity concept seems to hold within acceptable limits (e.g. Wang et al., 1992; Cox et al., 1995; Hansen et al., 1997). Aforementioned GCM simulations included various feedbacks including cloud feedbacks. However, they did not take into account the effect of aerosol on the microphysical properties of clouds. Aerosol particles do not only *directly* scatter solar radiation; they also act as cloud condensation nuclei. For fixed cloud liquid water content this *indirectly* results in more and smaller cloud droplets and thus brighter clouds (Twomey, 1974). This effect is traditionally referred to as the first indirect effect. Clouds that contain smaller droplets are less efficient at releasing precipitation (Albrecht, 1989). Therefore, it is expected that aerosol-contaminated clouds live longer; an effect that is referred to as the second indirect effect. Both the direct and the first and second indirect effects will cool the surface-troposphere system. In the discussion of aerosol radiative forcing the direct and indirect aerosol effects are separated.

The aerosol direct radiative forcing is most conveniently calculated with a RTM that is connected to a global CTM that includes aerosols. To estimate the indirect radiative forcings several options exist that all require application of a GCM. The first indirect effect can be obtained from the difference in radiation fields that are obtained by two

radiative transfer calculations using input from equilibrium runs with a GCM. The first calculation provides the radiation fields for the equilibrium atmospheric state, excluding interaction between aerosols and clouds. For the second radiation calculation, all fields (cloud water and -dimensions, water vapor, lapse rate, etc.) are kept constant except the cloud droplet spectrum that is changed in accordance with the modeled aerosol fields. The difference between the two radiation calculations provides the first indirect effect. Another way to estimate the first indirect effect is to compare the radiation fields of two distinct GCM runs, i.e. one with and one without aerosol-cloud interaction. Many of the forcing estimates that are given in the IPCC TAR (Penner et al., 2001) were obtained in this way. Apart from the first indirect effect they also include some dynamical and water vapor feedbacks. In a strict sense these estimates can therefore not be considered radiative forcings. However, Rotstayn and Penner (2001) have shown that for the first indirect effect changes in their forcing estimates due to the so-included feedbacks stayed within acceptable limits. Estimates of the second indirect effect can only be obtained from two distinct equilibrium GCM runs, because by definition feedbacks to the liquid-water path and cloud amount have to be included. Radiative forcing of the second indirect effect is therefore wrong nomenclature. Nevertheless, the estimated forcing caused by second indirect effect, calculated from the difference in net irradiance at the tropopause between an equilibrium run with the feedbacks and a run without the feedbacks, is valuable. The reason is that the radiation perturbations caused by imposed cloud optical depth and cloud extension have climate sensitivities comparable to doubled CO<sub>2</sub> and/or spectrally invariant +2% solar constant changes (Hansen et al., 1997). It thus remains useful to mutually compare the different radiative forcings.

### 2.1.3 Absorbing aerosols

For (partly) absorbing aerosols the situation becomes more complicated. Absorbing aerosol may either have small positive or negative direct radiative forcing depending on the single scattering albedo, which is the ratio of scattering and the sum of scattering and absorption. Recent field campaigns (e.g. TARFOX, ACE-II, INDOEX) reveal that this near-zero radiative forcing at the tropopause is accompanied by a disproportionately larger change in surface incoming irradiance and tropospheric heating (e.g. Lohmann and Feichter, 2001; Ramanathan et al., 2001a). How this finally translates to a change in global yearly-average surface temperature depends on the coupling between surface and overlying atmosphere. The fundamental assumption underlying the radiative forcing concept is that the surface and the troposphere are strongly coupled by convective heat transfer processes, i.e. the earth-troposphere system is in a state of (or close to) radiative-convective equilibrium. The net result of radiative-convective equilibrium is that the vertical temperature profile within the troposphere is largely determined by convective heat transport, while the vertically averaged surface-troposphere temperature is regulated by radiative balance at the tropopause. Mixing will thus redistribute heat and restore lapse rates. In this way absorbing aerosols short-circuit the hydrological cycle by depositing heat directly into a layer that would otherwise be heated by the latent heat originating from heat absorbed at the surface and lost through evaporation (Menon et al., 2002). Small direct radiative forcings may thus indicate that the direct effect of aerosols on the global yearly-mean temperature is small.

Reduced incoming irradiance at the surface combined with increased atmospheric heating may however change the surface-atmosphere coupling significantly so that the lapse rate is not restored. Indeed, for small TOA aerosol forcing, Ramanathan et al (2001a) showed that perturbation of the distribution of solar energy can lead to a large regional surface cooling accompanied by a warming of the lower troposphere. Jacob et al. (2005) conclude that for absorbing aerosol the traditional radiative forcing is an erroneous metric for the impact of aerosol forcing on the surface temperature. They suggest calculating the global mean radiative forcing at the surface along with that at the top of atmosphere (which equals the radiative forcing at the tropopause in the case of stratospheric adjustment) so that information on how forcing affects the lapse rate can be inferred. The additional climate feedback of absorbing aerosol on the lapse rate has important implications due to subsequent changes in clouds. This effect of absorbing aerosols on clouds is referred to as the ‘semi-direct’ aerosol effect (Grassl, 1979; Hansen et al, 1997), distinguishing it from the indirect effect of aerosol on cloud microphysics and the classical direct effect in the absence of cloud interaction.

The semi-direct effect depends heavily on the altitude of the absorbing aerosols and the type of clouds considered. For conditions typical of Indian Ocean trade cumulus clouds Ackerman et al. (2000) found significant reductions in cloud liquid water path and cloud fraction using large eddy simulations with heating by absorbing aerosols focussed in a layer 900 m thick where clouds tend to form. For qualitatively similar aerosol heating rate profiles Feingold et al. (2005) found similar results. However, when confining the smoke aerosol to sub-cloud layers Feingold et al. found that the added heat destabilized the sub-cloud layer resulting in increased convection with subsequent increased liquid water content. Johnson et al. (2004) studied the effect of absorbing aerosol in the case of marine stratocumulus. They found that mildly absorbing aerosol in the boundary layer warmed sub-cloud and cloud layers thus enhancing the existing diurnal cycle, manifested by further reduced liquid water path during daytime. Aerosol over the boundary layer increased the temperature difference of the capping inversion, leading to a lower entrainment rate and a moister boundary layer and optically thicker clouds. For aerosol distributed over boundary layer and aloft, enhanced decoupling was found to be more important than the lowered entrainment thus yielding thinner clouds. An important implication of the above studies (Feingold et al. and Johnson et al.) is that the current widely accepted assumption that the semi-direct effect is always positive may not be true.

Because of the potentially small (top of atmosphere) radiative forcing of absorbing aerosol and its semi-direct effect on clouds, the basic condition that climate response has to have a fixed proportionality to the aerosol radiative forcing comparable to other forcings such as solar irradiance or well-mixed greenhouse gases, is violated. This violation has led to the introduction of the concept of efficacies of different forcing agents (Joshi et al., 2003; Hansen and Nazarenko, 2004). Efficacy,  $E$ , is defined as the ratio of the climate sensitivity parameter  $\lambda$  for a given forcing agent to  $\lambda$  for a doubling of  $\text{CO}_2$ . The efficacy is then used to define an effective forcing  $\Delta F_e = E \cdot \Delta F$ . Although elegant, the use of efficacies will not resolve the real problem that for critical single scattering albedos the radiative forcing or surface temperature response is (near) zero which will result in undetermined climate sensitivity.

The conclusion that the concept of radiative forcing is insufficient when comparing absorbing aerosol and greenhouse gas climate effects becomes even more acute if we

take into account that purely scattering aerosols are very rare. There is increasing awareness of the fact that aerosol particles are almost always internally mixed to some degree (Penner et al., 2001; Haywood and Boucher, 2000). The single scattering albedos of most Northern Hemisphere aerosol mixtures are in the 0.85 to 0.95 range (Jacobson, 2001), whereas the critical single scattering albedos at which the aerosol impact shifts from cooling to warming or positive forcings become negative, fall in that range (Hansen et al., 1997).

The above implies that for the calculation of aerosol indirect and semi-direct global-scale temperature responses equilibrium GCM simulations are required. This inspired Shine et al. (2003) to explore a new concept of forcing that was based on a suggestion by Hansen et al. (2002). The *adjusted troposphere and stratosphere forcing*,  $\Delta F_{ats}$ , is the top-of-atmosphere forcing calculated in a GCM by holding sea-surface and land-surface temperatures fixed and allowing temperature adjustment in the stratosphere and troposphere. The main difference with the IPCC radiative forcing definition is that tropospheric lapse rate and other characteristics such as cloud cover are relaxed to the new equilibrium. Shine et al. (2003) show that  $\Delta F_{ats}$  is an excellent predictor of the equilibrium surface temperature calculated with the same GCM; for different forcing agents the spread around the mean value of  $\lambda$  is about 10%. A major advantage of this definition of forcing, considering the fact that for absorbing aerosol a GCM has to be run anyway, is that owing to the fixed surface temperatures equilibrium is reached quickly and only relatively short integrations are required (a few years compared to decades for equilibrium runs with ‘active’ oceans). This allows inclusion of more sophisticated cloud schemes that are essential for full appreciation of the semi-direct and indirect aerosol effects. Main drawback of this newly defined forcing is that  $\Delta F_{ats}$  may not be readily comparable across models because of differences in model dynamics and hydrology. This is in contrast to the current definition of radiative forcing, for which forcing estimates given by different models are comparable and for which the climate sensitivity parameter, that translates forcings into temperature response, is the parameter that varies between models.

It can be concluded that the concept of radiative forcing has shown its value for well-mixed greenhouse gases and scattering aerosols. However, some aerosol-impacts on climate are not well captured by the current definition of radiative forcing. The second indirect aerosol effect on radiation provided by IPCC is not a real radiative forcing according to its own definition. For (partly) absorbing aerosol, radiative forcing may not be useful to study the semi-direct aerosol effect. When the forcing estimates are used to estimate yearly-averaged global mean surface temperatures, other problems arise in the sense that no best estimate is provided for the second indirect effect and that only few aerosol species are included in the presently provided model estimates.

What we do know is that greenhouse gases and aerosols have competing effects on the global mean temperature. Although considerable uncertainties remain with respect to the various radiative forcings the consensus is that greenhouse warming is stronger than aerosol (direct and indirect) cooling. This conclusion is based on both radiative forcing estimates and observed global warming

## 2.2 Precipitation – hydrological cycle

The competing effects of aerosols and greenhouse gases do not only encompass temperature but also the hydrological cycle. The traditional radiative forcing concept is inappropriate to predict the magnitude or even the sign of the global mean precipitation changes that are caused by aerosols. It is therefore essential to seek for other approaches or forcing estimates that facilitate the research of the hydrological cycle.

The ratio of precipitation formed from local moisture sources (evaporation) to precipitation formed from moisture advection is known as the recycling ratio. The recycling ratio varies substantially from low values in winter to high values in summer. Many attempts have been made to estimate recycling ratios for different scales (synoptic- and various meso-scales) using both models (e.g. Bosilovich and Schubert, 2002) and observations (e.g. Trenberth, 1999a). General conclusion from these studies is that moisture supply for moderate or heavy precipitation does not come from local evaporation but mainly from transport, and thus from convergence of low-level moisture elsewhere in the atmosphere. Although the distribution of precipitation events around the globe may change when climate is changing, there is (as yet) no compelling evidence for widespread systematic long-term changes of severe local weather (tornadoes, thunder days, lightning and hail), extra-tropical cyclones, and tropical storms (Folland et al., 2001). The character of precipitation does not depend on the nature of the precipitating system alone, but also on the available moisture. Therefore, it makes sense to study the potential changes in precipitation characteristics by considering the expected changes in atmospheric water vapor. The Clausius-Clapeyron equation predicts an increase of the water holding capacity of the atmosphere of ~7% per degree Celsius increase in temperature. An increase in the water holding capacity does not necessarily result in an increase in atmospheric water vapour (it is not self-evident that a larger bucket contains more water than a small one). However, in the boundary layer<sup>1</sup>, the increase in water vapour with temperature in proportion with the Clausius-Clapeyron relation is uncontroversial (Stocker et al., 2001). If the spatial dimensions and frequency of occurrence of precipitating systems are not changing themselves (Folland et al, 2001), advection of air that contains more moisture shifts all systems towards more intense precipitation. This increase proceeds at about the same rate as the moisture increase, namely 7% per degree Celsius (Trenberth et al., 2003). Moreover, additional latent heat release may further invigorate the precipitating systems, a process that is likely to be more important for the events with heavy precipitation.

The effect of aerosols on cloud microphysics may explain that not all precipitating systems produce more precipitation. Clouds that form in aerosol-polluted air initially consist of more small cloud droplets than those that form in unpolluted air, which leads to the earlier described first aerosol indirect effect on radiation. In warm clouds with moderate vertical extension, the growth of cloud droplets through coagulation is reduced because the collection efficiency strongly decreases with smaller radii. Droplets sufficiently large to precipitate are therefore less easily produced which leads to suppression of precipitation in warm polluted clouds. During the further

---

<sup>1</sup> The boundary layer is the turbulent, well-mixed shallow layer near the ground, which can be regarded as being directly moistened by evaporation from the surface.

vertical development of a convective cloud, the formation of frozen hydrometeors large enough for precipitation is likewise affected. For heterogeneous freezing (homogeneous freezing only occurs in cirrus clouds at very low temperatures), the probability of freezing is roughly proportional to the droplet volume. The formation of graupel by riming is also increasingly inefficient for small droplet and ice particle sizes. Hence, aerosols generally suppress precipitation, but not only that. Because of the inefficiency of the warm rain processes to generate precipitation, the onset of downdrafts by precipitating hydrometeors is delayed so that strong vertical convection can more easily develop. This leads to further invigoration of a deep convective cloud by the release of additional latent heat of freezing and thus potentially to enhanced precipitation intensities. Whether anthropogenic aerosol actually leads to suppressed precipitation or delayed onset of more vigorous precipitation depends on the background aerosol levels and the atmospheric stability (Khain et al., 2004). Overall it can be expected that the aerosol effect on cloud microphysics leads to stronger weather extremes. While precipitation formation in small cloud systems is efficiently suppressed, deep convective cloud systems are expected to feature delayed, but more intense precipitation due to dynamic invigoration.

The theory on suppressed or delayed onset of precipitation is supported by evidence from several case studies. Space borne measurements of ship tracks in marine stratocumulus provided the first evidence that effluents from ship stacks change cloud microstructure such that their water is redistributed into a larger number of smaller droplets (Coakley et al., 1987). Albrecht (1989) extrapolated these observations to clouds thick enough to precipitate and concluded that the effluents have the potential to suppress precipitation. Similar pollution tracks are created from pollution sources over Australia. Rosenfeld (2000) showed that clouds in a pollution plume had little coalescence, had not glaciated, and did not precipitate, whereas the unpolluted clouds had strong coalescence and were precipitating. Andreae et al. (2004) performed in-situ measurements of convective cloud systems over the Amazon basin and found that, on a large scale, biomass burning smoke significantly suppresses the warm rain processes in clouds that ingested the smoke compared to clouds in clean environments. Overall the microphysical effect of aerosol on precipitating clouds is probably to reduce precipitation intensity throughout most of the spectrum of possible intensities, but to intensify some of the heavy and extreme precipitating systems.

So far it has been shown that an increase in the moisture content of the atmosphere will likely increase the rate of precipitation by supplying more moisture and by local invigoration of precipitating systems through latent heat release (Trenberth, 1998, 1999b, 2003) and that increased levels of aerosol may reduce all precipitation intensities but the strongest. This may help us understand how precipitation characteristics may change, but it does not tell us whether total precipitation increases or decreases, i.e. how the hydrological cycle is changing. In a warmer climate the atmosphere can not only contain more water vapor, also the evaporation rates change. For different temperatures, the energy available at the surface (net total irradiance minus storage in the underlying surface) is redistributed over latent- and sensible heat fluxes in a different manner. It is known that evaporation consumes more of the available energy at the surface than sensible heat production at higher temperatures (Priestley and Taylor, 1972; Holtslag and Van Ulden, 1983). On the long-term evaporation is balanced by precipitation. In a warmer climate, we thus might expect an increase in total precipitation. However, the change in the ratio of latent heat to



sensible heat is not the dominant driver of evaporation; it still depends on the available energy at the surface. Energy available for evaporation and sensible heat mainly comes from incoming solar irradiance absorbed at the surface. Solar surface irradiance is therefore the single most important quantity that drives the hydrological cycle.

In the section on radiative forcing it was already mentioned that recent field campaigns reveal large reductions in surface incoming irradiances. From globally distributed radiometers it is known that surface incoming irradiances are reduced over the last decades. This reduction, referred to as “global dimming”, is not a temporal or regional feature. For the period 1964-1993, considerable (and significant) global dimming is observed over large regions of Africa, Asia, Europe and North America with the decrease of surface incoming irradiance averaging 2% per decade (Gilgen et al., 1998). When zonally-averaged, global dimming is positive everywhere. The degree of global dimming varies markedly with latitude, exceeding  $1 \text{ Wm}^{-2}$  per year (1958-1992) in the mid-latitudes of densely populated and industrialized Northern Hemisphere to slightly positive values over the southern most latitudes of the Antarctic (Stanhill and Cohen, 2001). The observed dimming in the (about) 35-years period prior to the early 1990s is most likely caused by a change in the transmissivity of the Earth’s atmosphere (Stanhill, 2005). Recently, Wild et al. (2005) used available surface observations that became available after 1990 to prolong the time series of the above studies and found that the dimming did not persist into the late 1990s. Instead, a widespread brightening has been observed since the late 1980s. They find that the transition from dimming to brightening over Europe and Japan is in line with a similar shift in transparency of the cloud-free atmosphere as determined from pyrheliometer measurements. Wild et al. relate the gradual recovery of the European atmospheric turbidity after the 1980s, to a decrease of aerosol burden due to more effective clean-air regulations and the decline in the economy with the political transition in Eastern European countries. Pinker et al. (2005) estimated global temporal variations of solar surface irradiance from satellite observations. For the period 1983 to 2001 they find over land slightly negative tendencies that are not statistically significant. For the same period they find over sea an overall increase in surface solar irradiance; this change is a combination of a decrease until about 1990, followed by a sustained increase.

Whether the globe is brightening or dimming has important consequences for the hydrological cycle. As mentioned, at the surface there is a balance between net incoming total irradiance, storage into the surface, latent heat flux, and sensible heat flux. One or all of these components will change to compensate for the change in incoming surface solar irradiance. Annually and globally averaged, 60 to 70 percent of the absorbed solar radiation at the surface is balanced by evaporation (Kiehl and Trenberth, 1997), and it is thus possible that a major fraction of the reduction or increase in surface solar radiation is balanced by a change in evaporation (Ramanathan et al., 2001b). On the long term changed evaporation will have to be balanced by a change in rainfall; consequently the hydrological cycle can become stronger or it spins down.

The remaining question is thus to what extent the increase in latent heat, at the expense of sensible heat, invigorates or compensates for the change in incoming irradiance. Presently, the only way to answer this question is to analyse the outcome

of complex coupled Ocean-Atmosphere GCM equilibrium simulations. The model used in such simulations should contain all processes relevant for aerosol radiative forcing and changes in aerosol concentrations should be fed back on the cloud (micro)physics and dynamics. Feichter et al. (2004) performed such a series of equilibrium experiments with pre-industrial and present day greenhouse gases and aerosols concentrations and found remarkable results. The global hydrological cycle in their model is almost three times more sensitive to aerosol forcing than to greenhouse forcing. When both forcings are combined, a global warming is simulated, while the hydrological cycle is slowed down. The simulated global warming is in agreement with other simulations and observations, confirming the usefulness of the concept of radiative forcing that predicts greenhouse warming to be stronger than aerosol cooling. The slowing down of the hydrological cycle is attributed to the radiative effect of aerosols that is mainly felt at the earth's surface. This slowing down is not confirmed by other model studies. Generally, models show that a global-mean surface warming will be accompanied by an increase in global precipitation of about 1 to 2% per degree Celsius increase (Folland et al., 2001). However it is recognized that none of these model studies have realistic absorbing aerosols to assess the quantitative importance of the aerosol effect on the hydrological cycle (Ramanathan et al., 2001b) and most of these studies only included the direct radiative forcing of sulfate aerosols, whereas only a few studies include both the direct and indirect radiative effects of sulfate. When performing the appropriate simulation, all models that included some aerosol forcing confirmed the expected competing effects of aerosols and greenhouse gases on the hydrological cycle. In only one model (Roeckner et al., 1999), that is an earlier version of the model used by Feichter et al., (2004), the effect of aerosols was large enough to reverse the effect of greenhouse gases on the hydrological cycle. This remarkable result cannot be compared to the outcome of other models that are equivalently complex, simply because they do not exist. From observations (Folland et al., 2001) the simulated slowing down of the hydrological cycle can not be confirmed. However, the general features look quit trustworthy, although simulated present-day precipitation is lower than observed everywhere. At mid- and high latitudes this bias in the present-day precipitation causes a reduction in precipitation compared to pre-industrial values, whereas an increase is observed over the last century. It is essential to understand the reason for this exaggerated (aerosol-induced) slowing-down of the hydrological cycle, because future projections are worthless if the current climate is not well understood (simulated). It is likely that in the future atmospheric aerosol concentrations increase over parts of the globe due to increased use of energy in developing regions such as East Asia. Likewise, greenhouse gas concentrations increase and this increase will most likely be stronger than that for aerosols due the long lifetimes of most greenhouse gases. One might therefore anticipate that in the future the competing effect of aerosol and greenhouse gases on the hydrological cycle will be such that the hydrological cycle becomes increasingly stronger.



# The effect of aerosols on the downward shortwave irradiances at the surface – Measurements versus calculations with MODTRAN4.1

## 3.1 Introduction

Atmospheric circulation is primarily governed by the distribution of incoming solar radiation. The theoretical understanding of radiative transfer is therefore of crucial importance when studying weather, climate, or changes in climate. The idea that radiation modeling has a well established physical basis is widespread in the climate community. However, using twenty-six models of various degrees of sophistication, the international program of Intercomparison of Radiation Codes Used in Climate Models (ICRCCM) revealed a considerable spread in the radiative response to same input atmospheric profiles for fifty-seven cases considered (Fouquart et al., 1991). After considerable effort throughout the nineties the spread in model results of radiation codes is still substantial. Using a selection of four (midlatitude summer) cloud- and aerosol-free ICRCCM standard cases in eight different models, Kinne et al. (1998) find differences in modeled solar broadband irradiances at the surface up to  $25 \text{ Wm}^{-2}$  at solar zenith angles of  $30^\circ$ . The most recent ICRCCM extension (Barker et al., 2003) focuses on the performance of one-dimensional solar radiative transfer codes when operating on partially cloudy atmospheres. The single cloudless case considered in this study reveals that the striking underestimated atmospheric absorption ( $20 \text{ Wm}^{-2}$  for overhead sun and standard tropical atmosphere) is only slightly less than found in studies performed 10–15 years ago.

Convergence of model results is desirable, but it is absolutely necessary that models and observations agree on the distribution of solar energy in the atmosphere. Cess et al. (1996), Conant et al. (1997,1998), Valero and Bush (1999), and Li and Moreau (1996) find agreement between observed and calculated atmospheric shortwave absorption for cloud-free situations, but others report poor agreement on the amount of energy absorbed by both the cloudy atmosphere (Cess et al., 1995, Ramanathan et al., 1995, Pilewskie and Valero, 1995) and the relatively simple cloud-free atmosphere (Wild et al., 1995, Arking 1996, 1999, Charlock and Alberta 1996, Kato et al., 1997, Kinne et al., 1998, Halthore et al., 1998, Wild 1999, Halthore and Schwartz 2000, Wendisch et al., 2002). These latter cloud-free studies reveal that, on

a global scale, observed absorption in the atmosphere is typically  $10 - 30 \text{ Wm}^{-2}$  larger than predicted by radiative transfer models. Differences are largest at low latitudes year round and for midlatitude summers, with measured absorption up to  $50 \text{ Wm}^{-2}$  larger than modeled. However, the bulk of the differences found is between 20 and  $35 \text{ Wm}^{-2}$ .

In this study we investigate the role aerosols play in this model-measurement discrepancy. To do so we choose to compare measured and modeled incoming solar broadband direct and diffuse irradiances at the surface into great detail on a limited number of cloudless days. The calculations are performed with the state-of-the-art radiative transfer code MODTRAN4.1 (Berk et al., 2000, and references therein). The input parameters used to run the model (aerosol optical thickness, aerosol absorption and scattering coefficients including relative humidity dependence, aerosol asymmetry parameter, boundary layer height, water vapor, ozone, and meteorological parameters) are obtained from comprehensive field observations during CLOSAeR. The CLOSAeR project was carried out in the framework of the Dutch National Research Programme on Global Air Pollution and Climate Change. The project aimed to study the effects of aerosol on closure of the regional short-wave radiation balance in the Netherlands in 2000 (Henzing et al., 2001).

Our study together with the LACE98 field campaign (Ansmann et al., 2002, Wendisch et al., 2002) are, to our knowledge, the only radiation closure studies performed in Europe. In the study of Wendisch and co-workers aerosol optical properties are obtained from Mie theory using measured microphysics, refractive index and humidity particle growth. In our study we choose not to calculate the aerosol optical properties but to obtain these properties independently from measurements, as was done e.g. by Halthore and Schwartz (2000). The advantage of this method is that sensitivities to model input parameters can be added. Moreover, we avoid that a measurement error in a single quantity propagates into all model input parameters. Another important feature of our study is that the selection of days is such that there are no layers above the boundary layer with raised aerosol concentrations. We, therefore, assume that all aerosols are contained within the rapidly overturning boundary layer (Veefkind et al., 1996). In this way aerosol characteristics measured at the surface provide valuable information on the vertical dependence of aerosol optical properties, that are used to obtain boundary layer averaged aerosol scattering and absorption coefficients.

In section 3.2, we present the experimental approach and we give an overview of the used set of instruments. In section 3.3 we discuss the radiation instruments and their measurement errors. The model and its input parameters are presented in section 3.4. In section 3.5 the errors in the model calculations are estimated from the model input parameter errors. The actual model-measurement comparison is done in section 3.6. In section 3.7 results are discussed. Conclusions are given in section 3.8.

## 3.2 Experimental approach

We study the effect of aerosols on shortwave surface irradiances on completely cloudless days. The reason for this restriction is three-fold. Firstly, the effect of aerosols on radiative transfer is best investigated when their effect is isolated, that is

when all other contributions are well known. Secondly, sun photometers cannot easily distinguish cloud optical thickness from aerosol optical thickness. Thirdly, reflections from clouds would affect the amount of diffuse radiation received.

Cloudless days are very rare in the Netherlands. In order to use all cloudless days in the year 2000, a stand-by warning was issued to the people that were responsible for the instruments that required manual operation or surveillance when the weather forecast was promising, so that crucial instruments would actually be operating. During the measurement days the absence of thin stratus or cirrus clouds was verified by visual inspection. Finally, the absence of clouds not visible to the naked eye was verified with lidars. However, we cannot exclude the presence of clouds away from zenith with certainty since the lidars only sample the zenith direction. In section 3.2.1 we discuss how lidars are used for the selection of cloudless days. In section 3.2.2 the instruments that are actually used in the model-measurement comparison are described and discussed. The instruments were deployed in the centre of the Netherlands at two locations less than 2 kilometers apart - De Bilt (52.100 °N, 5.183 °E) and Bilthoven (52.120 °N, 5.196 °E), unless stated otherwise (Figure 3.1). All instruments are listed in Table 3.1.



**Figure 3.1** The Netherlands with the measuring site De Bilt / Bilthoven in the centre

### 3.2.1 Selection of cloudless days

We use a troposphere lidar to detect clouds in the altitude range of 1 to 15 km (Sunesson et al., 1994, and Apituley et al., 1997). A boundary layer lidar routinely profiles the lowest 4 kilometers of the atmosphere. When the lidars detect a cloud the measurement day is excluded. Furthermore, the boundary layer lidar provides the height of the planetary boundary layer (Van Pul et al., 1994).

**Table 3.1** Overview of instrumentation and way of operation.

Location	Instrument	Operator	Parameters	Operation
Bilthoven	Boundary Layer Lidar	RIVM	PBL height, Backscatter profile	Automatic
	Tropospheric UV lidar	RIVM	Backscatter profile, Aerosol extinction profile	Operator controlled
	Aethalometer 1	RIVM	Aerosol absorption coefficient	Automatic
	Aethalometer 2	RIVM	Aerosol absorption coefficient	Automatic
	Nephelometer	ECN	Aerosol scattering coefficient	Automatic
De Bilt	Sun photometer	KNMI	Aerosol optical thickness	Automatic
	Pyrheliometer	KNMI	Direct irradiance	Automatic
	Pyranometer	KNMI	Diffuse irradiance	Automatic
	Radiosonde	KNMI	Water vapor column, relative humidity	Manual
	Brewer spectrometer	KNMI	Ozone column	Automatic
Petten	Impactor	ECN	Aerosol size distribution, composition	Manual

Sometimes high aerosol concentrations are present above the boundary layer. These so-called residual layers usually occur in the altitude range up to 3 km, and consist of aged polluted air masses transported on a continental scale. As a result of the growth of the boundary layer during the day the lowest nocturnal residual layers are often completely mixed into the boundary layer. Lidar data clearly marks the moment of mixing. The boundary layer lidar, measuring atmospheric backscatter, cannot discriminate between thin clouds and high aerosol concentrations. High aerosol concentrations above the boundary layer are seen as clouds and the measuring day is therefore excluded. Consequently, the lidar check does not only confirm the absence of clouds, but it also ascertains that no residual layers are present above the boundary layer.

Following this approach we select three cloudless days: 5 May, 14 May, and 19 June 2000. Nocturnal surface inversion layers and low level residual layers are cleared away by shallow convective overturning at about 14.00, 10.00, and 12.45 UT for 5 May, 14 May, and 19 June, respectively. The well-mixed surface aerosol layer found at later times, clearly identified by steady increase in radiosonde relative humidity with increasing height (Figure 3.2), was used in our study.

### 3.2.2 Instrumentation

In addition to the lidars that are used for the selection of cloudless measurement days, we use two types of instruments. The first type of instruments measures solar radiation. Solar broadband direct and diffuse surface solar irradiances are measured on a routine basis with a pyrheliometer and a shaded pyranometer, respectively. The second type of instruments provides the atmospheric input data needed for the radiative transfer model calculations. The main quantities here are the aerosol optical properties. The spectral aerosol optical thickness is obtained from a six-channel sun photometer. The aerosol absorption coefficient is deduced from measurements with a

standard commercial instrument that measures light-absorption (aethalometer). The aerosol light scattering coefficient is determined with (integrating) nephelometers. The sum of scattering and absorption coefficients defines the extinction coefficient. The aerosol single scattering albedo is defined as the fraction of extinction that is caused by scattering. The effect of water vapor on the scattering properties of aerosols is taken into account in the single scattering albedo using a radiosonde water vapor profile together with the relative-humidity dependence of the light-scattering as measured with a humidograph (Ten Brink et al., 2001). The asymmetry parameter of aerosols is not measured on site. However, the asymmetry parameter can be assessed using Mie theory and simultaneous aerosol size distribution measurements made in Petten, situated 80 kilometers to the northwest (downwind) of Bilthoven/De Bilt. The mixing height of the boundary layer is measured with the boundary layer lidar. The water vapor column is obtained from vertically integrated radiosonde data. The solar broadband surface albedo of the area surrounding Bilthoven/De Bilt is obtained from AVHRR satellite data. The total ozone column above the measuring site is measured with a Brewer spectrometer.

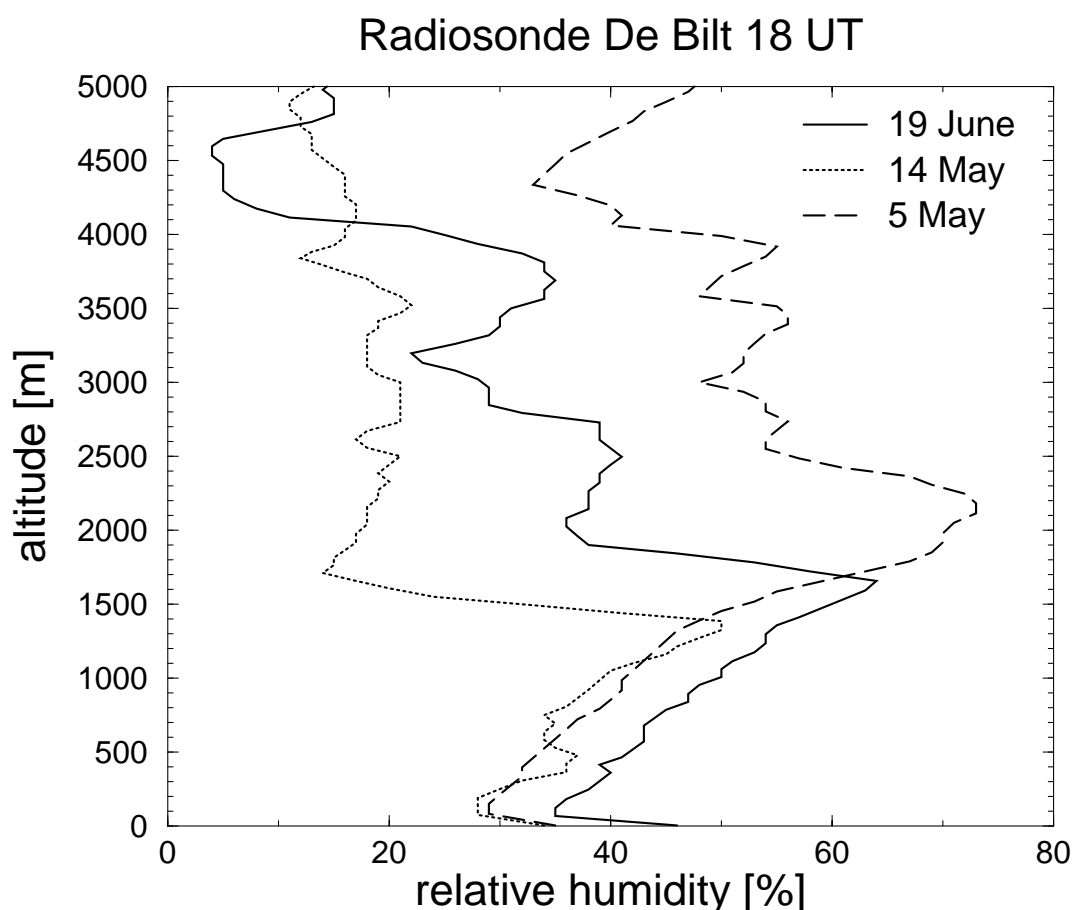


**Figure 3.2** Radiosonde relative humidity profiles for 5 May, 14 May and 19 June 2000. Relative humidity steadily increases from the surface, indicating that the boundary layer is well-mixed, until a sharp decrease occurs in relative humidity which marks the top of the boundary layer.



### 3.3 Surface irradiance measurements

Irradiance,  $E$ , is the radiative energy flux per unit time in a given wavelength interval through a horizontal surface of unit area. The irradiance is obtained by integrating the radiance, the radiative power per unit solid angle in a particular direction, weighted with the cosine of the viewing zenith angle,  $\mu = \cos \theta$ , over all viewing directions in a hemisphere of  $2\pi$  steradians. The irradiance is a function of wavelength:  $E(\lambda)$ , with the unit [ $\text{Wm}^{-2}\text{nm}^{-1}$ ]. Since we will mainly use spectrally integrated irradiances we define:

$$E = \int_{250\text{nm}}^{5000\text{nm}} E(\lambda) d\lambda, \quad (3.1)$$

with the unit [ $\text{Wm}^{-2}$ ]. The downward solar irradiance at the surface is often called the global irradiance, denoted by  $E_{glo}$ . It is useful to separate the downward irradiance at the surface in a direct part (unscattered radiation) and a diffuse part (scattered radiation), denoted by  $E_{dir}$  and  $E_{dif}$ , respectively. So, we have at the surface:

$$E_{glo} = E_{dir} + E_{dif}. \quad (3.2)$$

The direct irradiance measured perpendicular to the solar beam is called DNSI (direct normal solar irradiance). At the surface DNSI equals  $E_{dir}/\mu_0$ , where  $\mu_0$  is the cosine of solar zenith angle  $\theta_0$ . The DNSI at top-of-atmosphere (TOA) is denoted by  $E_0$ .

#### 3.3.1 Direct irradiance

Direct downward irradiance is measured on a routine basis with a Kipp & Zonen CH1 pyrhelimeter placed on a fully-automatic sun tracker. At the Royal Netherlands Meteorological Institute (KNMI) routine monitoring instruments are connected to standardized data acquisition systems that amplify the output voltage and convert the signal to the appropriate unit. The data acquisition system takes 12-second samples, which are averaged to 10-minute mean values that are used in this study. The pyrhelimeter measures DNSI received within a  $5^\circ$  field of view. DNSI is converted into direct solar irradiance by using the solar zenith angle.

Forward scattered light within the field of view of the pyrhelimeter is unjustly considered direct irradiance. We estimate the amount of diffuse irradiance due to molecular and particle scattering from the work of Box and Deepak (1979, equation (19)) and Deepak and Box (1978a, 1978b). Using 19 June 2000 aerosol optical thickness, phasefunction and solar zenith angle, we find diffuse/direct fractions at 500 nm that we apply to the whole spectrum. Doing that, we find 1.4 and 1.6  $\text{Wm}^{-2}$  diffuse irradiance contribution in the pyrhelimeter measurements for 12:30 and 15:30 UT, respectively.

The sensor in combination with a filter determines the spectral response and spectral range of the pyrhelimeter. The sensor is a thermal detector with an essentially flat spectral response from 0 to 50  $\mu\text{m}$ . The filter, which protects the blackened thermopile against weathering, is an infrasil I window of 2 mm thickness with a spectral range of 0.2 to 4  $\mu\text{m}$ .

**Table 3.2** Errors in measured and modeled irradiances, and the combination of both<sup>a</sup>.

Irradiance	Error measurement	Error calculation		Error combination	
		12:30 UT	15:30 UT	12:30 UT	15:30 UT
$E_{dir}$	10	12	10	16	14
$E_{dif}$	7	17	17	18	18
$E_{dir} + E_{dif} = E_{glo}$	12	17	16	21	20
$E_{\uparrow, TOA}$	-	22	15	-	-
$E_{abs}$	-	30	25	-	-

<sup>a</sup>Units are in  $\text{Wm}^{-2}$ . Error measurement: Pyrheliometer ( $E_{dir}$ ) and pyranometer ( $E_{dif}$ ) instrumental errors (Henzing and Knap, 2001). Global irradiance is obtained by taking the sum of direct and diffuse irradiances ( $E_{dir} + E_{dif}$ ). Error calculation: Error in MODTRAN4 model-calculated irradiances due to errors in model input parameters at two reference times on 19 June 2000 as explained in section 3.5. Error combination: Combined error in calculations and measurements as explained in section 3.6. All errors are positive and negative with equal probability.

Using the sun as a source, the pyrheliometer is calibrated directly to the World Standard Group (WSG) in Davos, Switzerland, which maintains the World Radiometric Reference (WRR) (Fröhlich, 1991, 1995). The WRR comprises 7 absolute cavity radiometers that ensure high absorptivity over the spectral range of interest for solar radiometry. This means that, although the CH1 pyrheliometer does not see solar radiation beyond the cut-off of the infrasil window (4 micron), this part is included by reference to the reading of the WSG. The pyrheliometer in our study thus measures the total solar spectrum.

In terms of the ISO 9060 standard, which has been accepted by WMO (1983), the CH1 is a ‘first class’ pyrheliometer. The largest source of error in our pyrheliometer measurements is caused by the temperature dependency of the thermocouple material. The maximum deviation, relative to 20 °C output signal, over the range [-20°C, 50°C] is estimated to be  $8 \text{ Wm}^{-2}$  at a cloudless solar noon in spring. The estimated uncertainties in pyrheliometer measurements are given in Table 3.2. For a complete discussion on the error associated with the pyrheliometer used in this study the reader is referred to Henzing and Knap (2001).

The measurements of direct irradiance for the three selected cloud-less days are presented in Figure 3.4 (p. 43).

### 3.3.2 Diffuse irradiance

The diffuse downward irradiance is measured on a routine basis with a shaded Kipp & Zonen CM11 pyranometer. The pyranometer is placed on the same sun tracker as the pyrheliometer. A shading sphere is fixed on the platform in such a way that the shading cone of the pyranometer is identical to the field of view of the pyrheliometer. From section 3.3.1 we estimate the missing diffuse irradiance for 19 June 2000 at 1.4 and  $1.6 \text{ Wm}^{-2}$  for 12:30 and 15:30 UT, respectively. As for the direct irradiance only 10-minute mean values of the diffuse irradiances are available.

The thermal detector of the pyranometer is easily affected by wind, rain, and thermal radiation losses to the environment. Therefore two Schott K5 glass domes, of 2 mm thickness each, shield the detector. The spectral range of the pyranometer is limited by the transmission of the glass; the 50% points are 335 nm and 2800 nm.

The pyranometer is calibrated at KNMI against the KNMI standard pyranometer using a lamp. The standard pyranometer was calibrated at the World Radiation Centre (WRC) in Davos according to the component summation method (WMO, 1996). In this method the pyranometer to be calibrated is operated unshaded. The output voltage of the pyranometer is then linked to the incident solar irradiance. The direct irradiance is determined using the WSG and the diffuse irradiance is measured using the shaded standard pyranometer of the WRC as stated in the WMO technical regulations. Both direct (WSG) and diffuse (WRC) standards measure the total solar range, so that the shaded pyranometer used in this study also yields results for the total solar range despite the spectral selection of the glass domes (Fröhlich et al., 1995).

A critical shortcoming of pyranometers is the existence of a zero offset. The pyranometer reads a zero offset, which is a voltage that is not caused by the absorption of solar radiation. Zero offset is mostly caused by the disturbance of the thermal equilibrium within the instruments. Longwave cooling of the pyranometer glass domes is the major source of zero offset for pyranometers under stable temperature conditions. Zero offset caused by longwave cooling of the domes is most easily recognised during the night in the absence of solar irradiance. The zero offset then leads to the well-known negative pyranometer readings.

It is unlikely that simple interpolations or extrapolations of nighttime offsets can be used to estimate daytime offsets and correct the measurements (Cess et al., 2000; Bush et al., 2000). Other surrogate methods to estimate the magnitude of daytime offsets are: 1) use of the temperature difference between the sensor and the dome (Bush et al. 2000), or 2) use of the net longwave downward irradiance as measured by an up looking pyrgeometer (Dutton et al., 2001, and Halthore and Schwartz, 2000). These methods were not applicable here, because method 1 requires instrument modification and method 2 requires pyrgeometer measurements that were not available on site.

In view of the fact that an accurate nighttime-to-daytime extrapolation is not trivial, and because pyranometer dome temperatures and longwave downward radiation were not measured, it was decided not to correct the pyranometer measurements for possible thermal zero-offsets, rather than applying an uncertain correction. Nevertheless, in section 3.6.5.3, a first order estimate of the daytime offset is given in view of the model-measurement intercomparison of irradiances.

The error in shaded pyranometer measurements is discussed by Henzing and Knap (2001) and given in Table 3.2. Table 3.2 contains the uncertainties in the irradiance measurements (as estimated by Henzing and Knap, 2001), in the model calculations (due to uncertainties in measured model input parameters, to be discussed in section 3.5), and the combination of both uncertainties (section 3.6). The measurements of diffuse irradiance for the three selected cloudless days are presented in Figure 3.4 (p. 43).

### 3.3.3 Global irradiance

Global irradiance can be measured with unshaded pyranometers. However, these measurements may suffer from relatively large errors due to the irregular cosine and azimuth response of the pyranometer. For measuring global irradiance the best accuracy is obtained by taking the sum of direct irradiance measured with a pyrliometer ( $E_{dir}$ ) and diffuse irradiance measured with a shaded pyranometer ( $E_{dif}$ ) (Flowers and Maxwell, 1985, Ohmura et al., 1998, Wardle et al., 1996, and Michalsky et al., 1999). We follow this approach. The global irradiances for the three selected cloudless days are presented in Figure 3.4 (p. 43).

Despite the absence of cirrus and other thin clouds, the curves of the measured direct, diffuse, and global irradiances, as shown in Figure 3.4 (p. 43), are not very smooth, especially around noon. This typical behavior (for the Netherlands) is caused by irregular boundary layer growth. 19 June, around 14 UT, direct irradiance is significantly lower than at adjacent times whereas diffuse irradiance is higher by about the same amount. Most probably, this increased extinction (scattering) is caused by a peak in the aerosol mass load and not by increased relative humidity as there is no significant change in the Angström parameter.

## 3.4 Radiative transfer model and its input data

### 3.4.1 MODTRAN4.1 description

For the calculation of irradiances we use the MODTRAN4 code (version 1.1, 17 April 2000) (see Berk et al., 2000, and references therein). MODTRAN4 is a spectral band radiative transfer model with a moderate spectral resolution (down to  $2 \text{ cm}^{-1}$ ). This is sufficient for our purpose of obtaining the spectrally integrated solar irradiance. In order to calculate molecular absorption in the presence of multiple scattering accurately, we use the correlated-k treatment using 17 absorption coefficients (k-values) per spectral bin of  $1 \text{ cm}^{-1}$ . Multiple scattering in MODTRAN4 is based on the use of multiple streams in the discrete-ordinates method (DISORT code of Stamnes et al., 1988); here we use 8 streams. The only missing element in MODTRAN4 is polarization. However, for irradiances the neglect of polarization yields only a very small error, far below 1 % for the spectral range of interest here (Lacis et al., 1998).

### 3.4.2 Overview of required input data

Atmospheric radiation modeling requires an adequate description of the incoming solar irradiance, the thermal structure of the atmosphere, the surface reflectance, and the composition and vertical profiles of atmospheric constituents (gases and aerosols). The optical ingredients of our model atmosphere are given below.

#### 3.4.2.1 Solar irradiance

For the top-of-atmosphere solar irradiance we use the MODTRAN built-in Kurucz (1995) spectral irradiance data file, that integrates to  $E_0 = 1368 \text{ Wm}^{-2}$  at 1 astronomical unit. Scaling of the solar irradiance accounts for the varying earth-to-sun distance throughout the year.

### 3.4.2.2 Gases and thermal structure

The Anderson et al. (1986) database describing the thermal and gaseous constituent profiles is incorporated into MODTRAN. In this study the standard midlatitude summer profiles of the database are used. The profiles of H<sub>2</sub>O and O<sub>3</sub> are scaled with the measured column densities. For CO<sub>2</sub> the volume mixing ratio of 365 ppmv as recommended by the IPCC (2001) is used for the scaling. The midlatitude summer reference pressure of 1013 hPa is used as the surface pressure. The use of the actual surface pressure, being 1013, 1021, and 1015 hPa on the respective measuring days 5 May, 14 May, and 19 June 2000, would only lead to minor modification in the Rayleigh scattering (less than 0.5 Wm<sup>-2</sup>). The profiles of NO<sub>2</sub>, CO, CH<sub>4</sub>, and 25 less radiatively active species are used unchanged.

### 3.4.2.3 Surface albedo

The surface albedo used in our MODTRAN calculations is spectrally flat. The actual surface albedo, however, has a wavelength dependence that is a function of surface type. To account for this wavelength dependence, while using a constant albedo, we weigh the spectral surface reflectance with modeled incoming global irradiance as will be explained in section 3.4.3.7. The consequence of this simplification is discussed in section 3.6.5.2.

### 3.4.2.4. Aerosol characteristics

In general aerosol concentrations in the free troposphere and stratosphere are much lower than in the boundary layer. In the absence of aerosol rich residual layers (see section 3.2.1) the total aerosol optical thickness is, therefore, very likely dominated by aerosol scattering and absorption in the boundary layer (Veefkind et. al., 1996). Therefore, we confine the aerosols in the model to the boundary layer. The height of the boundary layer,  $H_{bl}$ , was measured with a lidar. To represent the optical properties of the aerosols we specify the extinction optical thickness,  $\tau_{aer}$ , the single scattering albedo,  $a_{aer}$ , and the asymmetry parameter,  $g$ .

Aerosols of various chemical compositions and with different shapes and sizes are usually externally and internally mixed. We assume that this aerosol mixture can be regarded as an ensemble and that the scattering and absorption properties of this ensemble are determined by an average aerosol particle. The scattering cross-section of this ensemble average aerosol particle is denoted as:  $C_{sca}$  [m<sup>2</sup>]. Its absorption cross-section is denoted as:  $C_{abs}$  [m<sup>2</sup>]. The aerosol particle number density of the volume element is denoted by  $n$  [m<sup>-3</sup>]. The scattering coefficient,  $k_{sca}$  [m<sup>-1</sup>], of the ensemble can then be defined as:

$$k_{sca}(z) = n(z)C_{sca}(z) \quad . \quad (3.3)$$

Likewise, the absorption coefficient,  $k_{abs}$  [m<sup>-1</sup>], is defined as:

$$k_{abs}(z) = n(z)C_{abs}(z) \quad . \quad (3.4)$$

Due to rapid vertical mixing within the boundary layer on the selected days, the aerosol composition aloft in the boundary layer and the ensemble at the ground should strongly resemble each other. Changes in the scattering coefficient and absorption coefficient are caused by expansion of the volume element during uplift ( $n$  will

decrease) and by water uptake of the aerosols due to increasing ambient relative humidity during uplift ( $C_{sca}$  and  $C_{abs}$  will increase). The decrease in aerosol particle number density with increasing altitude is linearly proportional to the decrease in air density with increasing altitude. A humidification factor,  $f(RH)$  (i.e., the change in particle scattering or absorption due to water uptake by the particles) measured at the ground in combination with the relative humidity at a certain altitude yields the multiplication factor for the aerosol cross-sections at that height.

Including the aerosol water uptake and volume expansion, we obtain the boundary layer average scattering coefficient,  $\overline{k_{sca}}$ , and absorption coefficient,  $\overline{k_{abs}}$ :

$$\overline{k_i} = \frac{1}{H_{bl}} \int_{z=0}^{z=H_{bl}} k_i(z=0) \frac{\rho(z)}{\rho_0} f(RH(z)) dz \quad , \quad (3.5)$$

where  $z$  is the height,  $i$  stands for scattering or absorption,  $\rho(z)$  is the density of air at altitude  $z$ , and  $\rho_0$  the density of air at the ground. Multiplying these coefficients with the boundary layer height yields the boundary layer aerosol scattering optical thickness,  $\tau_{sca}^{bl}$ , and the boundary layer aerosol absorption optical thickness,  $\tau_{abs}^{bl}$ , respectively,

$$\tau_i^{bl} = H_{bl} \overline{k_i} \quad . \quad (3.6)$$

Because extinction is the sum of scattering and absorption, the boundary layer aerosol (extinction) optical thickness reads:

$$\tau_{ext}^{bl} = \tau_{sca}^{bl} + \tau_{abs}^{bl} \quad . \quad (3.7)$$

The (extinction) aerosol optical thickness of the total atmosphere,  $\tau_{aer}$ , is always greater than the aerosol optical thickness of the boundary layer,  $\tau_{ext}^{bl}$ , since aerosols are also present in the free atmosphere above the boundary layer. However, on the measurement days, extinction in the free atmosphere is expected to be small due to the absence of (aerosol rich) residual layers. Therefore, we assume in our study that all aerosols are in the boundary layer. The value of the measured  $\tau_{aer}$  is thus assigned to the boundary layer and plays the role of  $\tau_{ext}^{bl}$

$$\tau_{aer} = \tau_{ext}^{bl} \quad . \quad (3.8)$$

Below it is explained how the spectral aerosol optical thickness,  $\tau_{aer}(\lambda)$ , is obtained from measurements.

The aerosol single scattering albedo,  $a_{aer}$ , is the ratio between scattering and the sum of scattering and absorption. It expresses the chance that a scattered photon is not absorbed but will continue its journey as diffuse light. As we assume that all aerosols are confined to the boundary layer we can define:

$$a_{aer} = \frac{\overline{k_{sca}}}{\overline{k_{sca}} + \overline{k_{abs}}} \quad . \quad (3.9)$$

How to obtain the boundary layer average absorption and scattering coefficients from measurements will be explained in section 3.4.3.2 and 3.4.3.3, respectively. In section 3.4.3.4 it will be explained how the asymmetry parameter is obtained.

### 3.4.3 Measurements of model input data

#### 3.4.3.1 Spectral aerosol optical thickness

The spectral aerosol optical thickness is measured with the SPUV sun photometer placed on a sun tracker. The SPUV (YES, Inc.) measures the direct solar spectral irradiance at 368, 500, 670, 780, 870, and 940 nm. The SPUV is designed according to the WMO recommendations for sun photometers (Fröhlich and London, 1986). The 940 nm (water vapor) channel is not used in this study. The SPUV has been calibrated using the Langley method (Harrison and Michalsky, 1994). For the calibration, 22 cloudless mornings and afternoons in the three years preceding our study were used (for details see Henzing et al., 2001). Absolute calibration of the SPUV makes it possible to find the atmospheric optical thickness for a single cloudless event and to determine its variation during the day. The atmospheric optical thickness is caused by molecular scattering, gaseous absorption, and aerosol scattering and absorption. The first five SPUV channels are outside major absorption bands. For this reason aerosol optical thickness can be deduced by subtracting the Rayleigh scattering and ozone absorption (Chappuis band) optical thickness from the total atmospheric optical thickness. In Figure 3.3 the aerosol optical thicknesses at 368, 500, and 870 nm are shown for the three selected days. The aerosol optical thicknesses at the five SPUV wavelengths are extrapolated to longer wavelengths to cover the entire solar spectrum. Using the Angström relationship,  $\tau_{aer}(\lambda) = \beta\lambda^{-\alpha}$ , the aerosol optical thicknesses at 1000, 1500, 2000, 3000, and 5000 nm are found. The aerosol optical thicknesses for all 10 wavelengths are used in the model calculations. In between these 10 wavelengths the aerosol optical thickness is linearly interpolated.

#### 3.4.3.2 Aerosol absorption coefficient

The absorption coefficient,  $k_{abs}$ , is measured with a ground-based aethalometer (Magee Scientific Corp, model AE-10-M). Details of the instrument and method of analysis are described by Hansen and Schnell (1991) and Hansen (2002). The aethalometer is designed to measure the absorbing (black) fraction of the aerosol. The instrument collects the aerosol from ambient air on a quartz fiber filterband, while a continuous, calibrated airflow passes through it. The optical attenuation of light by the aerosol on the filterband is measured as a function of time, using a white light filament lamp and a photodetector at opposite sides of the band. The lamp and photodetector cover a wide spectral range. The exact range of the lamp is unknown and the detector is sensitive to wavelengths up to 1100 nm. The transmitted light intensity is measured and stored at 5-minute intervals, and from the observed decrease in transmission and the known volume of the sampled air, the absorption coefficient is calculated. In this study the 5-minute values are averaged to hourly mean values. The variation in light absorption due to water uptake by the particles is not measured and is assumed to be negligible. In section 3.5.2.3, we will show that the effect of the relative humidity dependence of the scattering coefficient is small due to low relative humidities at our comparison days. In general the humidity-sensitivity of the absorption coefficient is smaller than the humidity-dependence of the scattering coefficient. Therefore, we use equation (3.5) with  $f(RH) = 1$  to calculate the average boundary layer aerosol absorption coefficient,  $\overline{k_{abs}}$ .

### 3.4.3.3 Aerosol scattering coefficient

The aerosol scattering coefficient,  $k_{sca}$ , is determined with ground-based integrating nephelometers. The output of the instruments is the total scattering coefficient. After subtraction of the Rayleigh scattering contribution, the aerosol scattering coefficient is obtained. The effective wavelength of the instruments (Belfort Instruments MRI 1560) is 475 nm. The scattering coefficient at the measuring wavelength is translated to that at 500 nm using the Angström parameter as derived from sun photometry.

The standard procedure in nephelometry is to dry the air (including aerosol) by heating (Ten Brink et al., 1996; Dougle et al., 1998). This avoids complications with uptake and loss of water by the hygroscopic aerosol components during sampling and protects the optics against condensation. To limit evaporative losses of semi-volatile compounds such as ammonium nitrate, heating is limited to 40°C (Dougle and Ten Brink, 1996). The measurement of the RH-dependence of the scattering coefficient,  $f(RH)$ , is performed in a humidograph (Ten Brink et al., 2001). The relative humidity profile is measured with a radiosonde at 6-hr intervals.

Inserting the measurements of the nephelometers, the humidograph and the radiosonde into equation (3.5) yields the boundary layer average scattering coefficient,  $\overline{k_{sca}}$ , which is used in this study.

The single scattering albedo,  $a_{aer}$ , is obtained from  $\overline{k_{sca}}$  and  $\overline{k_{abs}}$  using equation (3.9). The thus obtained  $a_{aer}$  is valid at about 500 nm. Since multispectral measurements of  $\overline{k_{sca}}$  and  $\overline{k_{abs}}$  are not available,  $a_{aer}$  is assumed identical at all wavelengths.

### 3.4.3.4 Aerosol asymmetry parameter

The asymmetry parameter of the aerosol is not measured in this study. However, the aerosol size distribution, resolved by eight size bins, was measured in Petten (Henzing et al., 2001). From the measured aerosol size distribution, the asymmetry parameter can be computed using Mie theory, assuming spherical particles. We use a Mie program (De Rooij and Van der Stap, 1984) assuming a lognormal size distribution with a median radius  $r_g = 0.055$  micron and standard deviation  $\sigma = 1.8$ . We assume that the real part of the refractive index,  $\text{Re}(m)$ , is 1.5 at all wavelengths. This is a typical value for water-soluble aerosols (WCP-55, 1983). The imaginary part,  $\text{Im}(m)$ , is taken from water-soluble aerosol (WCP-55, 1983), but fixed to the average value of 0.01 in the near-IR. The results are tabulated in Table 3.3 for the selected wavelengths. It can be seen that  $g$  decreases rather strongly with increasing wavelength.



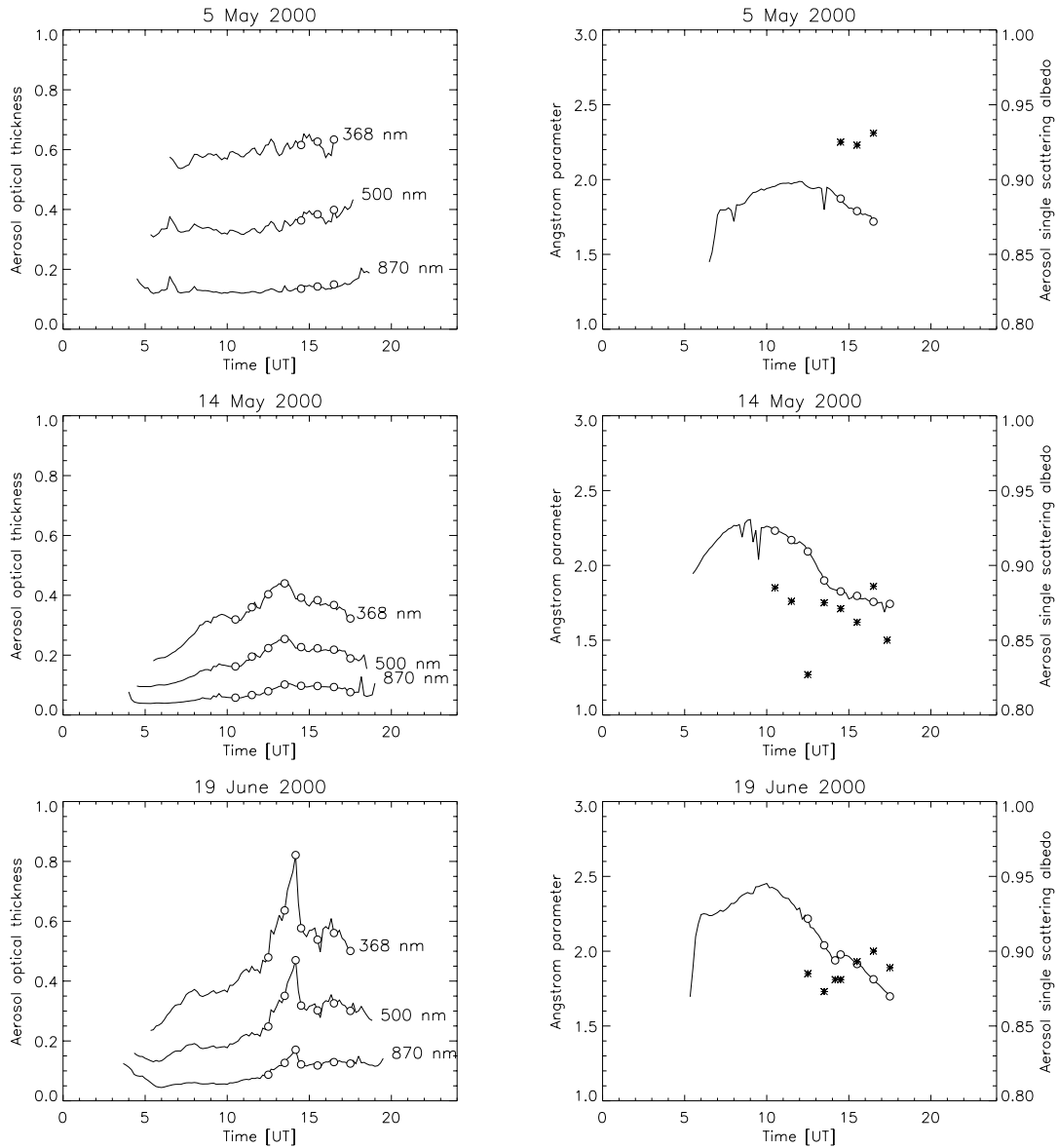


**Figure 3.3** (left panels) Daily variation of the aerosol optical thickness at three wavelengths (368, 500, and 870 nm) for the three selected days, values used in calculations are indicated by open circles. (right panels) Daily variation of aerosol single scattering albedo (asterisks) and Angström parameter (lines, open circles), for the three selected days.

### 3.4.3.5 Water vapor column

The effect of water vapor on the aerosol scattering properties is taken into account in the aerosol single scattering albedo (see section 3.4.2.4). Moreover, water vapor absorbs solar irradiance. The water vapor column is obtained from the vertically integrated radiosonde data, which are available every six hours. High temporal resolution integrated water vapor (IWV) measurements are available from a 50 km upwind station (Kootwijk, 5.81°E, 52.18°N) of a regional Global Positioning System (GPS) receiver network (Klein Baltink et al., 2002). Variations in IWV obtained using a linear interpolation between successive radiosondes agreed very well with the variation in IWV values retrieved from the GPS network. For collocation reasons the interpolated radiosonde IWV data was used in our calculations.

**Table 3.3** Results of Mie calculations of asymmetry parameter  $g$  for four size distributions (log-normal,  $\sigma=1.8$ )<sup>a</sup>

wavelength (nm)	Re( $m$ )	Im( $m$ )	Asymmetry parameter $g$			
			$r_g=0.037 \mu\text{m}$	$r_g=0.048 \mu\text{m}$	$r_g=0.055 \mu\text{m}$	$r_g=0.100 \mu\text{m}$
368	1.5	0.005	0.62	0.66	0.67	0.70
501	1.5	0.005	0.57	0.62	0.64	0.69
675	1.5	0.006	0.50	0.56	0.59	0.67
780	1.5	0.010	0.46	0.52	0.56	0.66
870	1.5	0.010	0.43	0.50	0.53	0.65
1000	1.5	0.010	0.39	0.46	0.50	0.63
1500	1.5	0.010	0.27	0.34	0.39	0.55
2000	1.5	0.010	0.19	0.26	0.30	0.47
3000	1.5	0.010	0.11	0.16	0.19	0.36
5000	1.5	0.010	0.05	0.07	0.09	0.22

<sup>a</sup>Median radii  $r_g=0.0368 \mu\text{m}$  and  $r_g=0.0475 \mu\text{m}$  correspond to distributions for which the wavelength dependence of the extinction agrees with the sun photometer data for 19 June 12:30 and 15:30 UT, respectively.  $r_g=0.055 \mu\text{m}$  is the median radius used in the reference calculations.  $r_g=0.1 \mu\text{m}$  corresponds to larger particles often observed (climatology in Petten).

### 3.4.3.6 Ozone column

The ozone column is measured with a Brewer spectrometer. Usually, the ozone column varies only slowly in the course of a day. The daily average value of the ozone column is therefore used in the calculations. For 5 May, 14 May, and 19 June 2000 we found, respectively, 360.4, 344.6, and 315.3 DU.

### 3.4.3.7 Surface albedo

Around the measuring site vegetation is dominant, but also motorways and built-up areas are found. To find a representative, but simple, spectral surface reflectance, we take a typical reflectance curve for photosynthetically active vegetation (Bowker et al., 1985, their Figure 2). This spectrum is split into two regions, VIS and NIR, according to the main processes responsible for the behavior of the curve. In the visible region (VIS) with wavelengths smaller than 700 nm, reflectance is normally low especially in the growing season due to photosynthesis. The transition to the near infrared region (NIR) is marked with a sharp rise in the reflectance at about 700 nm (the red edge). Reflectance in the NIR is dominated by reflection at the cell walls and absorption by the leaf water content (beyond 1300 nm).

In order to estimate the actual reflectances in the VIS/NIR, the NOAA/NASA Pathfinder AVHRR Land (PAL) data set was used (NASA, 2001). Of this data set, the so-called Daily Data Set was used, which contains global reflectances derived from AVHRR channels 1 and 2 mapped to an equal area projection ( $8 \times 8 \text{ km}^2$ ). These reflectances (Table 3.4) are corrected for Rayleigh scattering and ozone absorption (Agbu and

James, 1994). AVHRR channel 1 (580–680 nm) and channel 2 (730–1100 nm) thus yield the reflectance in VIS ( $R_{VIS} = 0.08$ ) and NIR ( $R_{NIR} = 0.22$ ), respectively. Assuming a Lambertian surface, these reflectances equal surface albedos ( $A_{s,VIS} = R_{VIS}$  and  $A_{s,NIR} = R_{NIR}$ ). The shortwave broadband albedo ( $A_s$ ) is obtained using a linear combination of the two reflectances:

$$A_s = c_{VIS} A_{s,VIS} + c_{NIR} A_{s,NIR} \quad , \quad (3.10)$$

where the coefficients  $c_{VIS}$  and  $c_{NIR}$  represent the ratio of global irradiance at the surface in the relevant wavelength region to the shortwave broadband global irradiance. Using the reference MODTRAN calculations (see Sect. 5) for the determination of the coefficients  $c_{VIS}$  and  $c_{NIR}$ , we find that  $A_s = 0.15$  both at 12:30UT and 15:30UT.

### 3.5 Sensitivity study of model calculations of shortwave irradiances on cloudless days

#### 3.5.1 MODTRAN4.1 calculations

Calculations of the downward shortwave irradiances at the surface are performed for the selected three cloudless days 5 May, 14 May, and 19 June 2000 and presented in Figure 3.4. The calculations are performed for every hour for the periods that the boundary layer was well mixed, as long as the direct irradiance exceeded  $150 \text{ Wm}^{-2}$ . This results in a total of 18 cases. Because the entire solar spectrum is included in the irradiance measurements, simulated irradiances are integrated from 250 to 5000 nm. The pyrheliometer window and pyranometer domes shield the detectors from thermal radiation. Therefore, thermal radiation is subtracted from the MODTRAN calculated irradiances. For the calculations, MODTRAN is fed with the measured input parameters as presented in section 3.4. A selection of input data is listed in Table 3.5. Although the measured input data are temporally averaged (e.g. sun photometer aerosol optical depth is averaged over 1 minute), the calculations are performed for an instantaneous moment (see the times in Table 3.5).

Before comparing the simulated surface shortwave irradiances to the measured irradiances, we will assess the uncertainties in the simulations. We assume that the model produces correct surface irradiances when fed with the correct solar insolation, surface reflectance, and atmospheric composition. Therefore, the only sources of error in the modeled irradiances are the errors in model input parameters for the chosen MODTRAN4.1 set-up. To estimate the magnitude of the errors in the calculated irradiances, we define two reference calculations on 19 June 2000: (1) at 12:30 UT (about 40 minutes after local solar noon) with  $\theta_0 = 33.7^\circ$ , (2) at 15:30 UT with  $\theta_0 = 53.5^\circ$ . In both reference calculations the input parameters are varied one-by-one with their measurement error or estimated error, while keeping the other parameters unchanged. The difference between the reference calculation and the perturbed reference calculation is a measure of the error in the calculated irradiance due to the error in the perturbed parameter.

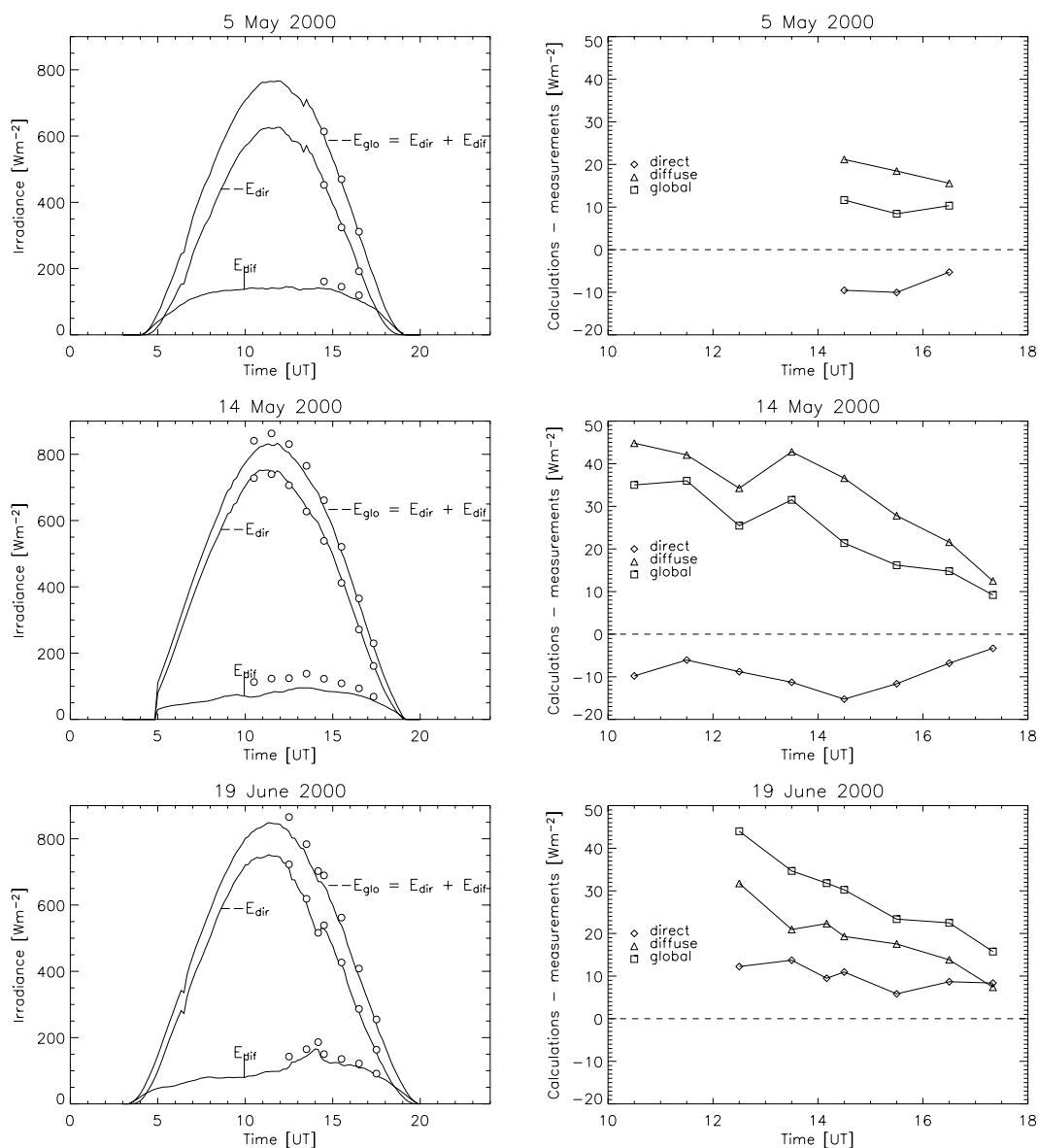


**Figure 3.4** (left panels) Measurements of direct irradiance ( $E_{dir}$ ), diffuse irradiance ( $E_{dif}$ ) and the sum of direct and diffuse irradiance ( $E_{dir} + E_{dif}$ ), for the three selected days, indicated by lines. Calculations of the same quantities are indicated by open circles. (right panels) The differences between measurements and calculations of direct, diffuse and global (direct + diffuse) irradiances for the three days.

### 3.5.2 Sensitivity study

In this section we will describe the error in each of the relevant input parameters of MODTRAN, and we will provide the resulting error in the calculated irradiances. In Tables 3.6 and 3.8 the MODTRAN reference and adjusted input parameter values are listed for the 12:30 UT and 15:30 UT runs for the case of 19 June 2000, respectively. The corresponding calculated irradiances are listed in Tables 3.7 and 3.9, respectively. For completeness, also the reflected irradiance at top of atmosphere (TOA),  $E_{\uparrow,TOA}$ , and the absorbed irradiance in the atmosphere,  $E_{abs} = (\mu_0 E_0 - E_{\uparrow,TOA}) - E_{glo}(1 - A_s)$ , are calculated for the selected days.

**Table 3.4** AVHRR-derived 8×8 km<sup>2</sup> surface reflectances for an area centered around De Bilt on 19 June 2000<sup>a</sup>.

	$R_1$			$R_2$			$A_s$		
↑	0.12	0.11	0.11	0.29	0.26	0.22	0.20	0.19	0.17
24 km	0.12	0.08	0.09	0.30	0.22	0.17	0.21	0.15	0.13
↓	0.10	0.09	0.08	0.20	0.19	0.19	0.16	0.14	0.14
	$\overline{R_1} = 0.10 \pm 0.02$			$\overline{R_2} = 0.23 \pm 0.05$			$\overline{A_s} = 0.16 \pm 0.03$		
	←— 24 km —→								

<sup>a</sup>The first two matrices contain channel 1 and channel 2 reflectances ( $R_1$  and  $R_2$ ), respectively. The third matrix contains the estimated shortwave broadband surface albedo ( $A_s$ ) assuming Lambertian surface reflectance. The centre value of each matrix corresponds to the pixel coordinates (52.110° N, 5.130° E) closest to the coordinates of De Bilt (52.100° N, 5.183° E). Area-averaged values and standard deviations are given below the matrices.

### 3.5.2.1 Sensitivity to aerosol optical thickness errors

The calibrated sun photometer provides the total optical thickness ( $\tau = \tau_{Ray} + \tau_{gas} + \tau_{aer}$ ). Because the errors in the Rayleigh scattering optical thickness ( $\tau_{Ray}$ ) and the gaseous absorption optical thickness ( $\tau_{gas}$ ) are small compared to the errors in the aerosol optical thickness, the latter can be obtained from the Lambert-Beer law:

$$E(\lambda) = E_0(\lambda) \exp[-\tau M], \quad (3.11)$$

where  $M$  is the relative airmass. Using straightforward error calculus:

$$\Delta_{abs} \tau_{aer} = \left[ \frac{(\Delta_{abs} \ln E_0)^2 + \left( \Delta_{abs} \ln \left( \frac{E_{dir}}{\mu_0} \right) \right)^2}{\left( \ln E_0 - \ln \left( \frac{E_{dir}}{\mu_0} \right) \right)^2} \right]^{\frac{1}{2}} \cdot \left\{ 1 + \frac{\tau_{Ray} + \tau_{gas}}{\tau_{aer}} \right\} \cdot \tau_{aer}, \quad (3.12)$$

where  $\Delta_{rel} M$  is the relative error in the relative airmass,  $\Delta_{abs} \ln E_0$  is the absolute error in the extraterrestrial irradiance as found from the SPUV calibration, and  $\Delta_{abs} \ln (E_{dir}/\mu_0)$  is the absolute error in the measured DNSI. According to equation (3.12), the error in a single aerosol optical thickness value is the result of the combined error in relative airmass, the SPUV calibration, and the direct normal solar irradiance (DNSI) measurement. We estimate the relative error in the relative airmass to be 1% due to meteorological variations in temperature, pressure or humidity relative to the well-mixed molecular standard atmosphere used to determine the relative airmass (Young, 1994). We take a relative error of 2% in DNSI. The absolute error in the calibration factor,  $\Delta_{abs} \ln E_0$ , is the standard deviation of the mean calibration factor (Henzing et al., 2001). We thus find the aerosol optical thicknesses at 550 nm for the reference times:  $\tau_{aer}(12:30 \text{ UT}) = 0.20 \pm 0.02$  and  $\tau_{aer}(15:30 \text{ UT}) = 0.25 \pm 0.02$ .

**Table 3.5** Selected model input data. The data is obtained as described in section 3.4.3.

Day, Time (UT)	$\tau_{aer}$					$\alpha$	$a_{aer}$	$H_2O$ ( $kg\ m^{-2}$ )	$H_{bl}$ (km)
	368 Nm	500 nm	670 nm	780 nm	870 nm				
May 5, 14:30	0.62	0.36	0.18	0.13	0.14	1.87	0.93	17	1.85
May 5, 15:30	0.63	0.38	0.21	0.15	0.14	1.79	0.92	17	1.88
May 5, 16:30	0.63	0.40	0.23	0.16	0.15	1.72	0.93	17	1.88
May 14, 10:30	0.32	0.16	0.05	0.03	0.06	2.23	0.89	11	1.10
May 14, 11:30	0.36	0.20	0.06	0.05	0.07	2.17	0.88	12	1.20
May 14, 12:30	0.40	0.22	0.08	0.06	0.08	2.09	0.83	12	1.42
May 14, 13:30	0.44	0.25	0.10	0.08	0.10	1.90	0.88	12	1.68
May 14, 14:30	0.39	0.23	0.10	0.07	0.10	1.83	0.87	12	1.70
May 14, 15:30	0.38	0.22	0.10	0.07	0.10	1.80	0.86	13	1.69
May 14, 16:30	0.37	0.22	0.11	0.08	0.09	1.76	0.89	13	1.67
May 14, 17:30	0.32	0.19	0.11	0.08	0.08	1.74	0.85	13	1.64
June 19, 12:30	0.48	0.25	0.09	0.07	0.09	2.22	0.89	19	1.50
June 19, 13:30	0.64	0.35	0.16	0.12	0.13	2.04	0.87	20	1.80
June 19, 14:10	0.82	0.47	0.24	0.17	0.17	1.94	0.88	21	2.00
June 19, 14:30	0.58	0.32	0.15	0.11	0.12	1.98	0.88	22	2.00
June 19, 15:30	0.54	0.30	0.15	0.11	0.12	1.91	0.89	23	2.00
June 19, 16:30	0.56	0.33	0.18	0.13	0.13	1.81	0.90	25	2.00
June 19, 17:30	0.50	0.30	0.17	0.13	0.12	1.70	0.89	26	2.00

In order to establish the sensitivity of the calculations to the error in  $\tau_{aer}$ , the aerosol optical thickness is changed according to the above uncertainties. The fractional change at 550 nm is then applied to all other wavelengths. At 12:30 UT the error in aerosol optical thickness leads to an error in  $E_{dir}$ ,  $E_{dif}$ , and  $E_{glo}$  of 11, 7, and 4  $Wm^{-2}$ , respectively. At 15:30 UT the uncertainties in  $E_{dir}$ ,  $E_{dif}$ , and  $E_{glo}$  are 9, 5, and 4  $Wm^{-2}$ , respectively.

### 3.5.2.2 Sensitivity to absorption coefficient errors

The accuracy of  $k_{abs}$  is limited due to three major problems. One problem is the use of white light in the aethalometer to measure the absorption coefficient, which is essentially wavelength-dependent. Another problem is the loss of light, due to scattering particles on the filter, which is erroneously attributed to absorption. A third potential problem was discovered during our study, when we observed a decrease of aethalometer sensitivity when the total load on the filter increased, resulting in a non-linear response.

As a conservative estimate, we assume that  $k_{abs}$  is not better measured than within a factor of 2. As will be shown later, this limited accuracy does not preclude meaningful use of the aethalometer data in the model calculations. At 12:30 UT the best estimate of the aerosol absorption coefficient is  $\overline{k_{abs}} = 6.9 \times 10^{-6} m^{-1}$ , corresponding to  $a_{aer} = 0.89$ . Due to the factor 2 the possible range of error for  $\overline{k_{abs}}$  is  $[1.4 \times 10^{-5} m^{-1}, 3.5 \times 10^{-6} m^{-1}]$  and for  $a_{aer}$   $[0.79, 0.94]$ . At 15:30 UT the best estimate is  $\overline{k_{abs}} = 7.2 \times 10^{-6} m^{-1}$  ( $a_{aer} = 0.89$ ) with the range for  $\overline{k_{abs}}$   $[1.4 \times 10^{-5} m^{-1}, 3.6 \times 10^{-6} m^{-1}]$  and for  $a_{aer}$   $[0.81, 0.94]$ .

**Table 3.6** The MODTRAN input values used in the 19 June 2000, 12:30 UT, reference run are given in column 3 (“reference value”). Values used in the sensitivity study are given in column 6 (“adjusted value”). Reference values and applied changes of the input parameters are described in the corresponding subsections of section 3.5.

Input parameter	Symbol	Reference value	Applied change	Explanation	Adjusted value	Consequence
Aerosol optical thickness (550 nm)	$\tau_{aer}$	0.20	+0.02 -0.02	measurement error	0.22 0.18	
Asymmetry parameter (501 nm)	$G$	0.638	see text	larger particles smaller particles	0.694 0.567	
Aerosol absorption coefficient	$k_{abs}$	$6.9 \times 10^{-6} \text{ m}^{-1}$	$\times 2$ $\times \frac{1}{2}$	measurement error	$13.9 \times 10^{-6} \text{ m}^{-1}$ $3.5 \times 10^{-6} \text{ m}^{-1}$	$a_{aer} = 0.79$ $a_{aer} = 0.94$
Aerosol scattering coefficient	$k_{sca}$	$5.4 \times 10^{-5} \text{ m}^{-1}$	-0.3	assumed dry air (aerosol scattering insensitive to $RH$ )	$5.1 \times 10^{-5} \text{ m}^{-1}$	$a_{aer} = 0.88$
Surface albedo	$A_s$	0.15	+0.03 -0.03	standard deviation	0.18 0.12	
Boundary layer height	$H_{bl}$	1.5 km	$\times 2$	experiment	3000 m	
Water vapor column	$\text{H}_2\text{O}$ (g)	$19.0 \text{ kg m}^{-2}$	+10% -10%	interpolation error	$20.85 \text{ kg m}^{-2}$ $17.05 \text{ kg m}^{-2}$	

**Table 3.7** MODTRAN results for 19 June 2000, 12:30 UT. Incident irradiance at TOA is  $\mu_0 E_0 = 1138 \text{ W m}^{-2}$ ,  $\theta_0 = 33.7^\circ$ . Differences (adjusted calculation minus reference calculation) in  $\text{W m}^{-2}$ . The input (reference and adjusted) parameters are given in Table 3.6.

MODTRAN run	$E_{dir}$ , $\text{W m}^{-2}$	$E_{diff}$ , $\text{W m}^{-2}$	$E_{dir} + E_{diff}$ , $\text{W m}^{-2}$	$E_{\uparrow, \text{TOA}}$ , $\text{W m}^{-2}$	$E_{abs}$ , $\text{W m}^{-2}$
Irradiance of reference run	723	142	865	170	232
No aerosol	+122	-84	+38	-4	-28
Aerosol optical thickness	-11 +11	+7 -7	-4 +4	+0 -0	+2 -3
Asymmetry parameter	larger particles smaller particles	+3 -4	+3 -4	-2 +3	-1 +1
Aerosol absorption coefficient	increased decreased	0 -15 +9	-15 +9	-6 +4	+19 -13
Aerosol scattering coefficient	dry air	0 -1	-1	-0	+0
Surface albedo	increased decreased	0 -2	+2 -2	+21 -21	-23 +22
Boundary layer height	increased	0	+0	-1	-0
Water vapor column	increased decreased	-4 +4	-4 +4	-1 +1	+4 -5

**Table 3.8** The MODTRAN input values used in the 19 June 2000, 15:30 UT, reference run are given in column 3 (“reference value”). Values used in the sensitivity study are given in column 6 (“adjusted value”). Reference values and applied changes of the input parameters are described in the corresponding subsections of section 3.5.

Input parameter	Symbol	Reference value	Applied change	Explanation	Adjusted value	Consequence
Aerosol optical thickness (550 nm)	$\tau_{aer}$	0.25	+0.02 -0.02	measurement error	0.27 0.23	
Asymmetry parameter (501 nm)	$G$	0.638	see text	larger particles smaller particles	0.694 0.567	
Aerosol absorption coefficient	$k_{abs}$	$7.2 \times 10^{-6} \text{ m}^{-1}$	$\times 2$ $\times \frac{1}{2}$	measurement error	$14.3 \times 10^{-6} \text{ m}^{-1}$ $3.6 \times 10^{-6} \text{ m}^{-1}$	$a_{aer} = 0.81$ $a_{aer} = 0.94$
Aerosol scattering coefficient	$k_{sca}$	$6.0 \times 10^{-5} \text{ m}^{-1}$	-0.4	assumed dry air (aerosol scattering insensitive to $RH$ )	$5.6 \times 10^{-5} \text{ m}^{-1}$	$a_{aer} = 0.88$
Surface albedo	$A_s$	0.15	+0.03 -0.03	standard deviation	0.18 0.12	
Boundary layer height	$H_{bl}$	2.0 km	$\times 2$	experiment	3.0 km	
Water vapor column	$\text{H}_2\text{O (g)}$	23.3 kg m <sup>-2</sup>	+10% -10%	interpolation error	25.6 kg m <sup>-2</sup> 21.0 kg m <sup>-2</sup>	

**Table 3.9** MODTRAN results for 19 June 2000, 15:30 UT. Incident irradiance at TOA is  $\mu_0 E_0 = 813 \text{ W m}^{-2}$ ,  $\theta_0 = 53.5^\circ$ . Differences (adjusted calculation minus reference calculation) in  $\text{W m}^{-2}$ . The input (reference and adjusted) parameters are given in Table 3.8.

MODTRAN run	$E_{dir}$ , $\text{W m}^{-2}$	$E_{diff}$ , $\text{W m}^{-2}$	$E_{dir} + E_{diff}$ , $\text{W m}^{-2}$	$E_{\uparrow, TOA}$ , $\text{W m}^{-2}$	$E_{abs}$ , $\text{W m}^{-2}$
Irradiance of reference run	427	136	562	139	196
No aerosol	+134	-84	+49	-13	-29
Aerosol optical thickness	-8 +9	+4 -5	-4 +4	+1 -1	+2 -3
Asymmetry parameter	0 0	+5 -5	+5 -5	-3 +3	-0 +0
Aerosol absorption coefficient	0 0	-15 +9	-15 +9	-7 +5	+20 -12
Aerosol scattering coefficient	0 0	-1 +2	-1 +2	-0 +13	+1 -15
Surface albedo	0 0	-2 -2	-2 -2	-13 -13	+15 +15
Boundary layer height	0 0	+0 -0	+0 -0	+0 -1	+0 +3
Water vapor column	-3 +3	+0 +0	-3 +3	-1 +1	+3 -4



In order to establish the sensitivity of the calculations to the error in the aethalometer measurements, the single scattering albedos at both ends of the ranges of error are used as model input. The total aerosol optical thickness is kept unchanged, so there are no consequences for  $E_{dir}$ . For both reference times the absolute effects on  $E_{dif}$ , and thus  $E_{glo}$ , are equal as can be seen from Tables 3.7 and 3.9. Increasing the aerosol absorption coefficient,  $E_{dif}$  and  $E_{glo}$  decrease by as much as  $15 \text{ Wm}^{-2}$ . With decreasing aerosol absorption the increase in  $E_{dif}$  and  $E_{glo}$  is  $9 \text{ Wm}^{-2}$ .

### 3.5.2.3 Sensitivity to scattering coefficient errors

The aerosol scattering coefficient is determined by the combined use of radiosonde, humidograph, and nephelometer measurements. As far as the radiosonde watervapor profile is concerned, it probably does not play a significant role in the overall error of the scattering coefficient. The determination of the dry scattering coefficient normally contributes most to the overall error. The drying in the nephelometer is accomplished by heating. Ammonium nitrate, which is the dominant aerosol for the Netherlands (Ten Brink et al., 1996), is semi-volatile and may (partly) evaporate upon heating. Such evaporation is indeed observed: on days with high RH decreases in signal of as high as 50% have been registered. On the days used in this study, surface RH is so low that drying is minimal and evaporative losses should be negligible. Probably the most important source of error for the scattering coefficient during our study is the translation of the groundbased measurement of the RH-dependence of the scattering coefficient to the boundary layer average scattering coefficient. Neglecting the RH dependence in the boundary layer, we find that  $\overline{k_{sca}}$  (12:30UT) is decreased from  $5.4 \times 10^{-5} \text{ m}^{-1}$  to  $5.1 \times 10^{-5} \text{ m}^{-1}$ , so  $a_{aer}$  decreases from 0.89 to 0.88. A similar decrease in  $a_{aer}$  occurs for the 15:30 UT case.

In order to establish the sensitivity of the irradiance calculations to the error in the boundary layer average aerosol scattering coefficients, the single scattering albedos corresponding to completely dry atmospheres ( $a_{aer} = 0.88$ ) at the reference times are used as model input. The results are in Tables 3.7 and 3.9. Again  $E_{dir}$  is not affected. For both reference times the absolute effects on  $E_{dif}$  ( $E_{glo}$ ) are equal. For the dry atmosphere  $E_{dif}$  and  $E_{glo}$  decrease by a modest  $1 \text{ Wm}^{-2}$ .

### 3.5.2.4 Sensitivity to asymmetry parameter errors

Aerosol size distribution measurements are used to obtain the asymmetry parameter using Mie theory. Unfortunately, the size distribution was not measured 5 and 14 May 2000. Based on a great many size distribution measurements at Petten in the past, it can be concluded that a size of  $r_g=0.055 \text{ }\mu\text{m}$ , as measured on 19 June 2000, is quite small. Therefore, we calculate the asymmetry parameter also for a size distribution with larger particles, namely with  $r_g=0.1 \text{ }\mu\text{m}$ . However, the Angström parameter that follows from the sun photometer measurements (Figure 3.3 right panels), suggests that the aerosol size distribution consists of smaller particles. For 19 June 2000, 12:30 UT (15:30 UT), we need to lower the median radius to  $r_g=0.037 \text{ }\mu\text{m}$  ( $r_g=0.048 \text{ }\mu\text{m}$ ) in order to meet the sun photometer spectral dependence, which has an Angström parameter of 2.2 (1.9). In Table 3.3 the asymmetry parameters corresponding to the measured size distribution and for the small and large particles are given for the selected wavelengths. It can be seen that  $g$  is larger for larger particles as expected.

The asymmetry parameters of the smaller and larger particles are used to establish the sensitivity of the irradiance calculations for the error in the asymmetry parameter. As is shown in Tables 3.7 and 3.9,  $E_{dir}$  is unaffected.  $E_{dif}$  and  $E_{glo}$  are increased in the perturbed calculation, because the larger particles scatter more in the forward direction. At 12:30 UT (15:30 UT)  $E_{dif}$  and  $E_{glo}$  are increased with 3 (5)  $\text{Wm}^{-2}$ . The smaller particles scatter more uniformly in all directions, so that  $E_{dif}$  and  $E_{glo}$  are decreased in the perturbed calculation. At 12:30 UT (15:30 UT)  $E_{dif}$  and  $E_{glo}$  are decreased with 4 (2)  $\text{Wm}^{-2}$ .

### 3.5.2.5 Sensitivity to water vapor column errors

A reasonable estimate of the error in the atmospheric water vapor column is 10%. At 12:30 UT we find  $\text{H}_2\text{O} = 19.0 \pm 1.9 \text{ kg m}^{-2}$ . At 15:30 UT,  $\text{H}_2\text{O} = 23.3 \pm 2.3 \text{ kg m}^{-2}$ . This error in absorption by water vapor leads to an error in both  $E_{dir}$  and  $E_{glo}$  of 4 and 3  $\text{Wm}^{-2}$  at 12:30 UT and 15:30 UT, respectively (see Tables 3.7 and 3.9). The effect on  $E_{dif}$  is less than 1  $\text{Wm}^{-2}$  at both reference times.

### 3.5.2.6 Sensitivity to surface albedo errors

The shortwave broadband surface albedo used in the simulations is obtained using AVHRR channel 1 and 2 reflectances for the single  $8 \times 8 \text{ km}^2$  pixel containing the measuring site, as described in section 3.4.2.7. A second estimate of the albedo is obtained by averaging the broadband reflectances of the nine AVHRR  $8 \times 8 \text{ km}^2$  pixels surrounding the measuring site. Doing so, we find  $A_s = 0.16 \pm 0.03$ .

The standard deviation 0.03 is used to investigate the sensitivity of the calculated irradiances to the assumed broadband surface albedo. As can be seen from Tables 3.7 and 3.9, the effect of the exercise  $A_s \pm 0.03$  is strongest for the reflected irradiance at the top of the atmosphere: at 12:30 UT  $E_{\uparrow, \text{TOA}}$  increases by 21  $\text{Wm}^{-2}$  for the 0.03 increase of  $A_s$ , whereas at 15:30 UT  $E_{\uparrow, \text{TOA}}$  increases by 13  $\text{Wm}^{-2}$  for the 0.03 increase of  $A_s$ . The effect on the surface irradiances is less pronounced: the increase of  $A_s$ , which increases multiple reflections between the surface and the atmosphere, increases  $E_{\downarrow}$  by 2  $\text{W m}^{-2}$  for both reference times.

## 3.5.3 Total error in the calculated irradiances

We express the error in the calculated irradiances due to the error in model input parameter  $x_i$  as:

$$\Delta E_{rad,i} = \left( \frac{\partial E_{rad}}{\partial x_i} \right) \Delta x_i . \quad (3.13)$$

Here *rad* stands for *dir*, *dif* or *glo* and  $(\partial E_{rad} / \partial x_i)$  represents the sensitivity, defined as the change in the computed  $E_{rad}$  for a unit change in input parameter  $x_i$ , keeping all other parameters constant. Assuming that all input parameters are independent, we estimate the overall error in the calculated irradiances due to uncertainties in the input parameters as:

$$\Delta_{calc} E_{rad} = \sqrt{\sum_i (\Delta E_{rad,i})^2} \quad (3.14)$$

( $\text{Wm}^{-2}$ ). The errors in the calculated irradiances are listed together with the irradiance measurement errors in Table 3.2.

### 3.6 Comparison between Modeled and Measured Downward Shortwave irradiances on cloudless days

#### 3.6.1 Comparison strategy

We define the difference between modeled and measured irradiances as:

$$DE_{rad} = E_{rad,calc} - E_{rad,meas}. \quad (3.15)$$

The error in  $DE_{rad}$  is then given by

$$\Delta DE_{rad} = \left[ (\Delta_{calc} E_{rad})^2 + (\Delta_{meas} E_{rad})^2 \right]^{1/2}, \quad (3.16)$$

since the errors in measured and calculated irradiances are uncorrelated. Using equation (3.16) and the values of  $\Delta_{calc} E_{rad}$ , given in section 3.5.3, and the values of  $\Delta_{meas} E_{rad}$  given in Table 3.2, we find the estimated errors  $\Delta DE_{rad}$  for the reference calculated irradiances listed in Table 3.2.

#### 3.6.2 Direct irradiances

For 5 May and 14 May 2000, the calculated direct irradiances are always smaller than the measured irradiances with a typical difference of 5 – 15  $\text{Wm}^{-2}$  (see Figure. 3.4 right panels). On 19 June 2000, however, the situation is reversed but the differences are of the same order of magnitude. Even when we assume that the smallest error estimate of  $\Delta DE_{dir}$ , is applicable, namely 14  $\text{Wm}^{-2}$ , we find all individual differences,  $DE_{dir}$ , to be smaller than, or very close to  $\Delta DE_{dir}$ . Therefore, we conclude that modeled and measured surface downward direct irradiances agree within the estimated uncertainty.

#### 3.6.3 Diffuse irradiances

For the diffuse irradiance there is less good agreement between the modeled and measured irradiances. For all cases the calculated diffuse irradiances are higher than the measured irradiances,  $DE_{dif}$  being between 7 and 44  $\text{Wm}^{-2}$ . The calculations and measurements tend to converge towards the end of the day, particularly on 14 May and 19 June. Despite the large error in the difference, the maximum  $\Delta DE_{dif}$  being 18  $\text{Wm}^{-2}$ , only 5 out of the 18 comparisons agree within the estimated uncertainty.

#### 3.6.4 Global irradiances

As was the case for the diffuse irradiance, all calculated values of the global irradiance are higher than the measured values,  $DE_{glo}$  being between 8 and 44  $\text{Wm}^{-2}$ . The trends that are seen in  $DE_{dif}$  are also present in  $DE_{glo}$ . The calculated values of  $E_{glo}$  generally agree best with the measurements for low sun elevation. Despite the large error in the difference, the maximum being 21  $\text{Wm}^{-2}$ , only 8 out of the 18 comparisons agree within the estimate uncertainty.

In conclusion, we find that calculated and measured direct irradiances at the ground agree within the combined error estimate. However, for the diffuse and global irradiances, we find that the calculated irradiances overestimate the measured irradiances. For a big majority of cases, the magnitude of the overestimation cannot be explained by pyranometer measurement errors, or by the error in the used model input parameters, or by a combination of both. Moreover, the overestimation seems to be dependent on the time on the day; the magnitude of  $DE_{dif}$  increases with increasing  $\mu_0$  for all three cases (Figure 3.5 top). In Figure 3.5 (bottom) the magnitude of  $DE_{dif}$  relative to the incoming irradiance at TOA ( $\mu_0 E_0$ ) is shown. The relative model-measurement difference shows not significant correlation with  $\mu_0$ , differences roughly amount 1–4% of TOA irradiance. This is in agreement with the results that we derive from Halthore and Schwartz (2000, their Table 1, 43 cases), who also find values of 1–4%.

In the next section we will discuss sources of errors that may lead to the systematic deviations from zero in  $DE_{dif}$ .

### 3.6.5 Discussion of possible sources of the disagreement between calculated and measured irradiances

Above we estimated the error in the difference between modeled and measured irradiances by including the uncertainties of the measurements that served as input for the model calculations. We saw that calculated and measured diffuse and global irradiances did not agree within the error estimate. In this section we will discuss some other uncertainties that can lead to a disagreement between calculated and measured irradiances.

#### 3.6.5.1 Spectral aerosol optical thickness

In the model calculations, the aerosol optical thicknesses at wavelengths longer than 870 nm are obtained by extrapolation using the Angström relation. However, from measurements in Petten we know that on 19 June 2000 (but also on other days with synoptic conditions similar to those in our study) the size distribution is bi-modal. The fact that  $\tau_{aer}(870 \text{ nm})$  is equal to or larger than  $\tau_{aer}(780 \text{ nm})$  for the three selected days confirms this. To study the effect of higher optical thickness of the aerosols at longer wavelengths, we recalculate the irradiances at the two reference times increasing the aerosol optical thickness to  $\tau_{aer}(870)$  at 1000 nm (case I) and 1500 nm (case II), keeping the aerosol optical thickness constant in-between and using the Angström relation for longer wavelengths. Increasing the aerosol optical thickness reduces the direct irradiance by 4 (10)  $\text{Wm}^{-2}$  for case I (case II) at both reference times. The corresponding increase in diffuse irradiances is 3 (6)  $\text{Wm}^{-2}$  at both reference times.

Using these irradiance values for case I (case II), 3 (10) out of 18 (18) comparisons of the direct irradiance do not agree within the error estimate (originally model and measurements agreed). For diffuse irradiance the situation also gets worse, only 4 (2) out of 18 (18) comparisons agree within the error estimate (originally we found agreement for 5 out of 18 comparisons). In view of this large effect, measurements of  $\tau_{aer}$  at longer wavelengths (e.g. at 1000, 1600, and 2200 nm) are desirable in later studies.

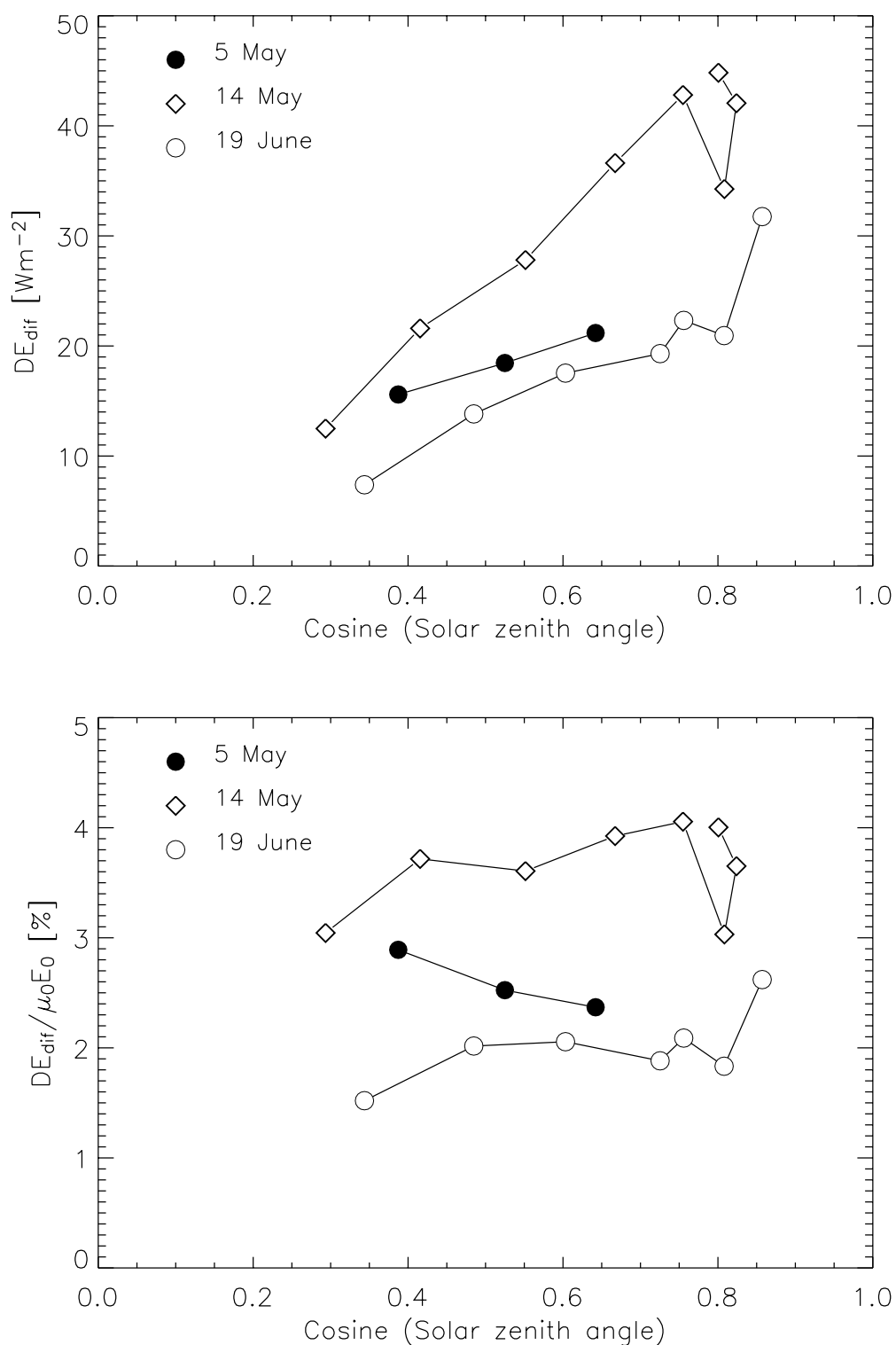


**Figure 3.5** (top) The difference between calculated and measured diffuse irradiances plotted as a function of the cosine of the solar zenith angle ( $\mu_0$ ). Individual comparisons on a single day (diamonds and circles) are connected by a thin black line. (bottom) Same but relative to the top-of-atmosphere incoming irradiance,  $\mu_0 E_0$ .

### 3.6.5.2 Surface albedo

In our model we use a spectrally flat albedo. However, for vegetation the surface albedo in the visible spectral region is generally smaller than at longer wavelengths (Bowker et al., 1985). The spectrally independent surface albedo is thus too reflective in the visible and too little reflective in the near infrared. Since scattering by the atmosphere is stronger in the visible spectral region than in the near infrared, the use of the broadband albedo will consequently lead to a modeled  $E_{dif}$  that is too high. Indeed, using the reflectances derived from AVHRR channels 1 (8%) and 2 (22%) for the visible region (VIS,  $\lambda < 700\text{nm}$ ) and the near infrared region (NIR,  $\lambda > 700$ ) as was done in section 3.4.3.7, we find that due to the assumption of a spectrally flat albedo of 0.15,  $E_{dif}$  is overestimated by 4 and 2  $\text{Wm}^{-2}$  for 19 June 12:30 UT and 15:30 UT, respectively.

Furthermore, in our model we use a constant albedo over the day. In reality, however, the surface albedo depends on the solar zenith angle. To obtain a representative solar zenith angle dependence of the surface albedo of our site, we use data from upward and downward looking pyranometers over pasture in Cabauw (less than 20 kilometers SW of the measuring site) at 19 June 2000. Although this surface albedo increases with increasing solar zenith angle by almost 50% over the range of zenith angles in this study, its effect on the downward diffuse irradiance and on  $DE_{dif}$  is only 1-2  $\text{Wm}^{-2}$ , due to the partly canceling effect of increasing surface albedo and decreasing incoming irradiance with increasing solar zenith angle. We therefore conclude that the large differences between modeled and measured surface downward irradiances and, more specific, the trend in the differences cannot be explained by uncertainties in the surface albedo.

### 3.6.5.3 Zero offset of pyranometer measurements

As explained in section 3.3.2 we chose not to correct the pyranometer measurements for thermal offset errors. In view of the differences between measured and modelled irradiances it is nevertheless useful to give a rough estimate of the error involved. Nighttime offsets in Cabauw typically vary between +1 and -6  $\text{Wm}^{-2}$ , where the latter value occurs during cloudless nights such as the ones prior to and after the measurement days used in this study. However, it is well-known that during cloudless conditions daytime values of the thermal offset are larger than nighttime values (Cess et al., 2000; Dutton et al., 2001). However, these works suggest that the daytime offset does not exceed the nighttime offset by a factor of two. This implies that a liberal estimate of the daytime offset for the cases described here is 12  $\text{Wm}^{-2}$  and probably smaller. In view of the values of  $DE_{dif}$  and  $DE_{glo}$ , the conclusion is justified that the pyranometer zero-offset alone cannot explain the differences between modeled and measured irradiances. It should, however, be mentioned that this offset does reduce the discrepancy, but the precise reduction is unknown. Since model-measurement differences seem to be a fixed fraction of the incoming irradiance at TOA (Figure 3.5, bottom), it is not very likely that the pyranometer zero offset is causing an important fraction of the discrepancy, as it would have led to a systematic model-measurement difference independent of solar insolation.

### 3.6.5.4 Vertical aerosol distribution

In our study, we assume that all aerosols are confined to a well-mixed boundary layer, which is an idealized representation of the reality. This assumption is almost harmless

with respect to surface downward irradiances, if optical properties of aerosols above the boundary layer do not deviate from boundary layer aerosol, see the double boundary layer height experiments in Tables 3.6–3.9. However, if free-tropospheric and stratospheric aerosols, with different asymmetry parameters and/or single scattering albedos, are responsible for a significant fraction of the aerosol optical thickness, then the calculated diffuse irradiances are erroneous. To estimate this effect, we use the MODTRAN built-in aerosol climatology (Shettle and Fenn, 1979) with free tropospheric aerosol and stratospheric aerosol. The aerosol optical thickness as obtained from the sun photometer is distributed over the boundary layer ( $\tau_{aer}(12:30)=0.12$  and  $\tau_{aer}(15:30)=0.15$  at 500 nm), free troposphere ( $\tau_{aer}=0.11$  and  $\tau_{aer}=0.14$ ), and stratosphere ( $\tau_{aer}=0.01$ ). The result is that, compared to the standard runs for 19 June 12:30 and 15:30 UT,  $E_{dif}$  increases by 9 and 7  $\text{Wm}^{-2}$ , respectively. Thus, the difference with the measurements increases. Larger single scattering albedos and increased forward scattering by larger particles, included in the aerosol climatology, cause the increase. To obtain agreement between calculated and measured  $E_{dif}$ , the single scattering albedo and asymmetry parameter of the aerosol above the boundary layer should be decreased to values far beyond the smallest values accepted in the sensitivity calculations. We believe that free tropospheric aerosol (aerosol optical thickness of stratospheric aerosol is too small to be of any importance) with those characteristics is unrealistic.

### 3.7 Discussion of a possible agreement between modeled and measured diffuse irradiances

In an attempt to determine when we *do* find agreement between modeled and measured diffuse irradiances, we varied the single scattering albedo and the median radius of the log-normal distribution beyond uncertainty estimates. The results of these model calculations are shown in Figure 3.6.

In Figure 3.6 (top), the largest single scattering albedos cause the largest modeled-measured diffuse irradiance differences,  $DE_{dif}$ . Decreasing the single scattering albedo to 0.70 and 0.79, we find closure for 19 June 12:30 and 15:30 UT, respectively. Although both single scattering albedos are outside the measurement uncertainty limits, they are not completely improbable. However, for 14 May 2000, the model-measurement differences are much larger, whereas  $\tau_{aer}$  is much lower (Figure 3.3 left panels). Consequently the single scattering albedo has to be lowered more rigorously to 0.56 and 0.61 for 14 May 12:30 and 15:30, respectively. Such low single scattering albedos do not only fall outside the measurement uncertainty limits, they are very low even for heavy industrialised areas or metropolitan city centres.

In Figure 3.6 (bottom) the largest median radii, corresponding to common size distributions in the Netherlands, cause the largest model-measurement differences. The smaller the particle median radius is chosen, the smaller  $DE_{dif}$  becomes. For 19 June 2000, agreement is obtained for particles as small as 0.003 and 0.015  $\mu\text{m}$  for 12:30 and 15:30 UT, respectively. For 14 May 2000, it is not possible to find agreement by reducing the aerosol particle sizes.

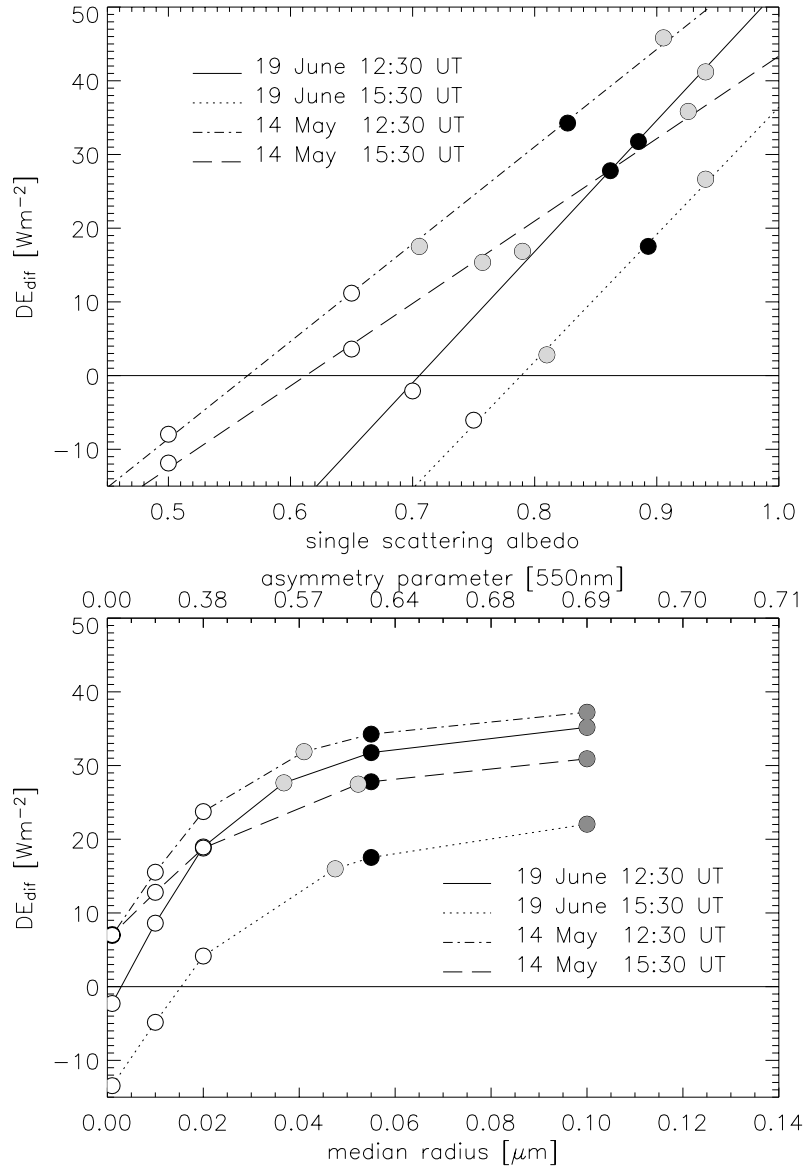


**Figure 3.6** Differences between modeled and measured diffuse irradiance,  $DE_{dif}$ , as a function of single scattering albedo,  $a_{aer}$  (top) and median radius or asymmetry parameter (bottom). In each plot  $DE_{dif}$  is given for two low aerosol optical thickness cases (14 May, 2000, 12:30UT,  $\theta_0 = 36^\circ$  and 15:30UT,  $\theta_0 = 57^\circ$ ) and two high aerosol optical thickness cases (19 June, 2000, 12:30UT,  $\theta_0 = 34^\circ$  and 15:30UT,  $\theta_0 = 54^\circ$ ). (top) Black filled circles indicate the values used in the standard calculations of Figure 3.4. Grey filled circles correspond to calculations with the decreased aerosol absorption (high  $a_{aer}$ ) and the increased aerosol absorption (low  $a_{aer}$ ) of Tables 3.6–3.9. Agreement, i.e.  $DE_{dif}=0$ , is obtained when  $a_{aer}=0.70$  and  $a_{aer}=0.79$  for 19 June 12:30 and 15:30 UT, respectively; for 14 May 12:30 and 15:30 UT agreement is obtained when  $a_{aer}=0.56$  and  $a_{aer}=0.61$ , respectively. (bottom) Filled circles indicate the values used in the standard calculations of Figure 3.4; light grey circles indicate the median radius for which the Mie calculated Angström parameter equals the sun photometer Angström parameter; dark grey circles correspond to climatological large particles. Agreement is obtained for  $r_g=0.003 \mu m$  and  $r_g=0.015 \mu m$  for 19 June 12:30 and 15:30 UT, respectively. For the case of 14 May (low aerosol optical thickness) no agreement can be obtained by reducing the aerosol particle size.



In the following we will make first order estimates of three corrections that reduce  $DE_{dif}$ . We discussed in section 3.3.1 that the pyrheliometer is measuring forward scattered light as diffuse irradiance. The shaded pyranometer is missing exactly this diffuse irradiance. We estimated the missing diffuse irradiance being 1.4 and 1.6  $\text{Wm}^{-2}$  for 19 June 12:30 and 15:30, respectively. Furthermore, we applied a spectrally flat albedo in our calculations. In section 3.6.5.2 we showed that this leads to an overestimate of the modeled diffuse irradiance. We estimated the amount to be 4 and 2  $\text{Wm}^{-2}$  for 19 June 12:30 and 15:30, respectively. To obtain the asymmetry parameter, we applied Mie calculations for a log-normal distribution with the median radius and standard deviation as obtained from microphysical measurements in Petten. As an alternative we can use the Angström parameter as measured with the sun photometer to obtain the median radius of the log-normal size distribution. This results in a smaller asymmetry parameter and thus less forward scattering. For 19 June 12:30 and 15:30, we find a reduction of the modeled diffuse irradiance of 4 and 2  $\text{Wm}^{-2}$ , respectively. Summing the above values, that all work in the same direction, we find that the differences between modeled and measured diffuse irradiances are reduced by 9.4 and 5.6  $\text{Wm}^{-2}$  for 19 June 12:30 and 15:30 UT, respectively. We find  $DE_{dif} = 22 \pm 18 \text{ Wm}^{-2}$  and  $DE_{dif} = 12 \pm 18 \text{ Wm}^{-2}$  for 19 June 12:30 and 15:30 UT, respectively. For 15:30 UT we now find agreement. For 12:30 UT we need a realistic pyranometer zero offset of 4  $\text{Wm}^{-2}$  to bring calculations and measurements into agreement. It is thus possible to find agreement between calculated and measured surface diffuse irradiances for the two reference calculations. Applying the largest correction (9.4  $\text{Wm}^{-2}$ ) 11 out of 18 comparisons agree without having to apply a correction for pyranometer zero offset. If, moreover, the maximum zero offset estimate of 12  $\text{Wm}^{-2}$ , given in section 3.6.5.3, is used for correction, we find that 17 out of 18 comparisons agree within the uncertainty estimates. For 14 May 10:30 UT the needed zero offset is 13.4  $\text{Wm}^{-2}$  and thus exceeds the maximal zero offset. Moreover, it should be mentioned that, after applying the largest correction to all calculations, calculated values remain always larger than measured irradiances, except for 19 June 17:30 UT.

Despite the partly obtained closure, there is still the fact that modeled diffuse irradiances exceed measured diffuse irradiances while direct irradiances are predicted correctly. This may indicate an erroneous aerosol scattering phase function or missing atmospheric absorption. A readily identifiable gas responsible for anomalous continuum absorption, as suggested by e.g. Kato et al. (1997) and Halthore and Schwartz (2000), is absent. It is unlikely that missing absorption is the result of a gaseous line absorber, because it is very unlikely that such a line absorber would not have been recognised until now (Solomon et al. 1998, Mlawer et al, 2000). We believe that the residual optical thickness that is obtained after subtracting molecular scattering and absorption from total extinction as measured with the sun photometer is caused by particles. We know that a smaller single scattering albedo and asymmetry parameter, associated with smaller particles, will reduce the calculated downward diffuse solar irradiance for a given aerosol optical thickness. To explain the model-measurement discrepancy,  $a_{aer}$  and  $g$  have to be changed beyond estimated uncertainty limits. However, for small particles ( $r_g < 0.1 \mu\text{m}$ ), the single scattering albedo and asymmetry parameter are very sensitive to both the median size  $r_g$  and the standard deviation  $\sigma$ . Both  $a_{aer}$  and  $g$  decrease drastically as  $r_g$  and  $\sigma$  decrease (e.g. Wendish et al., 2002; Fu et al., 1998). Therefore, it is possible that our uncertainty limits have been set too rigorous and that a narrower size distribution shifted towards

smaller particles, exists. The median radius of the log-normal distribution used in our calculations is possibly too large (cf. the sun photometer Angström parameter). According to Twomey (1977), we can expect aerosols to be smaller than  $0.1 \mu\text{m}$  for the low relative humidities that were present throughout the whole atmosphere at our comparison days ( $\text{RH} < 70\%$ ). The width of the log-normal distribution is therefore possibly taken too large. So, if these small particles do exist and are responsible for part of the extinction measured with the sun photometer, why do we not observe the correspondingly high absorption coefficient? We suggest two possibilities why these small particles are neglected in the aethalometer measurement. Firstly, ultrafine particles with radii smaller than  $0.025 \mu\text{m}$  are transported primarily by Brownian diffusion. They are therefore efficiently transported towards the surface where they are absorbed (Wesely, 1989; Seinfeld and Pandis, 1998). Thus, ultrafine particles present everywhere in the boundary layer (and above) may contribute to the aerosol extinction as observed with sun photometry, but they may not be as numerous near the surface and may not contribute to the measured aerosol absorption coefficient. Secondly, the aethalometer is designed to obtain absorbing carbonaceous aerosol concentrations. Therefore, the used aethalometer filter (Tissuquartz, Pallflex company), with aerosol retention close to 100% for particles larger than  $0.3 \mu\text{m}$ , should be suitable for this purpose. However, the retention for smaller aerosol particles, that hypothetically absorb light, is not very well known and certainly less than 100%. So, if these small particles are indeed undetected by the aethalometer, then the relevant question is whether they are numerous enough to be of any importance in terms of aerosol optical thickness. This remains to be investigated as future work.

### 3.8 Conclusions

The analysis for 18 cases of model calculations and measurements of cloudless surface irradiances revealed no discernable difference between model and measurement for the direct irradiance, but several significant differences for the diffuse (and, consequently, global) irradiance. The differences between modeled and measured direct irradiance vary between  $-15 \text{ Wm}^{-2}$  and  $+14 \text{ Wm}^{-2}$ , with an average of  $-2 \text{ Wm}^{-2}$ . Since the uncertainty in the difference varies between 14 and  $16 \text{ Wm}^{-2}$ , there is no evidence for a disagreement between model and measurement. For the diffuse irradiance, however, the measurement is always overestimated by the model. The overestimation varies from 7 to  $44 \text{ Wm}^{-2}$ , with an average of  $25 \text{ Wm}^{-2}$ . Since the uncertainty in the difference is estimated to be  $18 \text{ Wm}^{-2}$ , a majority of the cases (to be precise: 13 out of 18) reveals a significant overestimation of the measurements by the model.

Several instrument imperfections and model assumptions are likely to have caused biases that, in particular in combination, contribute to the discrepancy mentioned. Examples are: the pyranometer zero-offset, the portion of diffuse radiation that is not measured by the shaded pyranometer, the use of a wavelength-independent surface albedo, and the use of Mie calculations instead of sunphotometer measurements for the calculation of the aerosol asymmetry parameter. Although it is difficult to assess the precise magnitude of these biases, we estimate the cumulative effect between 5 and  $21 \text{ Wm}^{-2}$ , where the largest variation comes from the uncertainty in the zero-offset. In the worst case ( $21 \text{ Wm}^{-2}$ ), only one of the 18 cases reveals a significant

overestimation of the measurement by the model. It should be noted, however, that this situation is based on the crude assumption that the daytime pyranometer zero-offset amounts to twice the typical night-time value. If we relax this assumption, to values that are probably more realistic, then several cases point to a persistent and significant positive model-measurement difference for the diffuse irradiance. This difference amounts to typically 1–4% of the top-of-atmosphere irradiance, and does not depend on the solar zenith angle.

In order to shed light on the reason for the discrepancy for diffuse irradiance, we performed a model sensitivity analysis for the aerosol single scattering albedo and the mean radius, which is related to the asymmetry parameter (Figure 3.6). The analysis learned that closure can be obtained for smaller single scattering albedo or mean radius. Although the values have to be adjusted beyond the measurement uncertainty, the analysis seems to point to an explanation in terms of small aerosol particles. In particular, a size distribution that includes a branch of very small particles may very well remove the discrepancy for the diffuse irradiance. It is conceivable that these particles have not been detected by the instrument for measuring aerosol absorption, because they are simply too small, but also because they may not be so dominantly present near the surface, where dry deposition leads to removal of these particles. In both cases, too little aerosol absorption may have been measured, and too much forward scattering may have been assumed, leading to an overestimation of modeled diffuse irradiance.

A future experiment may focus on the suggested presence of ultrafine absorbing aerosols, and on the question if these particles exist in a sufficient concentration to significantly reduce model calculations of the surface diffuse irradiance. Needless to say, such efforts are not very useful if other measurement uncertainties are not reduced. Two aspects that need special attention are the pyranometer zero-offset and the sunphotometer calibration. Meanwhile, KNMI is in the process of updating its radiation measurements to the standards of the Baseline Surface Radiation Network (BSRN; Ohmura et al., 1998) and the operational sunphotometer has been calibrated at the High Altitude Research Station Jungfraujoch (Knap and Los, 2004).

# A parameterization of size resolved below cloud scavenging of aerosols by rain

## 4.1 Introduction

Aerosol removal processes remain an important source of uncertainty in global aerosol transport models (Rasch et al., 2000). Recent aerosol model intercomparisons such as AeroCom (AeroCom, 2005; Textor et al., 2005) show significant differences in modeled atmospheric aerosol concentrations that might be due to differences in the model representations of wet removal of aerosols. Aerosol particles are very efficiently removed from the atmosphere by in-cloud and below-cloud scavenging processes. For accumulation mode aerosols the in-cloud removal, governed by aerosols acting as cloud condensation nuclei or ice nuclei that are subsequently removed from the cloud when they grow large enough to form precipitation, is by far the most efficient atmospheric sink. However, very small particles are more easily scavenged by rain droplets because they are rapidly transferred into falling droplets as their Brownian motion exceeds the rain droplet fall velocity. Coarse particles are also more easily scavenged by rain droplets than accumulation mode aerosols because of their size and inertness (Slinn, 1984; Pruppacher and Klett, 1997).

On-line calculation of below-cloud scavenging parameters in large-scale aerosol models is (yet) unrealistic due to the large computational time involved. Therefore, studies often describe the size-resolved aerosol load as a diagnostic variable (Collins et al., 2001) or they confine themselves to precipitation free episodes so that wet removal can be neglected (Schulz et al., 1998; Vignati et al., 2001). Studies that do include size resolved below-cloud scavenging generally use approximate expressions for the scavenging rate based on mean rain droplet size (Gong et al., 2003).

The purpose of this study is to parameterize below-cloud scavenging for aerosols of various sizes taking into account the rain droplet spectrum. The parameterization will be applied to size resolved sea salt aerosol in the global chemistry transport model TM4. The importance of below-cloud scavenging relative to other removal mechanisms will be discussed and the impact on the overall sea salt aerosol lifetime will be investigated.

## 4.2 Below cloud scavenging coefficient

### 4.2.1 Explicit calculation

A rain droplet with radius  $R$ , sweeps per unit of time approximately the volume of a cylinder equal to  $\pi(R+r)^2(U_t - u_t)$ , where  $U_t$  is the droplet speed of fall,  $u_t$  the aerosol particle speed of fall, and  $r$  the aerosol particle radius. However, a falling droplet also perturbs the neighboring air and creates a flow-field around the droplet. Therefore, the actual volume swept by the falling droplet depends on the ability of the aerosol particle to adjust to the flow streamlines. The solution of this fluid mechanics problem is often expressed in terms of the collision efficiency  $E(R, r)$ , which is defined as the fraction of aerosol particles contained within the sweep-cylinder-volume that actually collides with the falling droplets. We can assume that the aerosol particle speed of fall is small compared to the rain droplet speed of fall and that the aerosol particle radius is small compared to the rain droplet radius. The differential scavenging coefficient  $\beta$ , which is the fractional amount (number, mass etc.) of aerosol removed by precipitation per unit time for a fixed aerosol particle radius, is then given by (Engelmann, 1968):

$$\beta(r) = \int_0^{\infty} \pi R^2 U_t(R) \varepsilon E(R, r) N(R) dR \quad , \quad (4.1)$$

where  $N(R)dR$  is the number of rain droplets with radii between  $R$  and  $R+dR$  per unit volume and  $\varepsilon$  is the retention efficiency that determines whether the collision between droplet and particle is effective. Below it is explained how the various terms that are necessary to perform the integration of equation (4.1) can be calculated.

#### 4.2.1.1 Rain droplet velocity

In our calculations we will assume that rain droplets always fall at their terminal velocities. We base our rain droplet terminal velocity on an empirical representation given by Atlas et al. (1973) but for  $R < 0.3$  mm we force the droplet velocity smoothly to zero using a linear fit to measurements of Gunn and Kinzer (1949) as proposed by Mätzler (2002). The pressure-independent droplet terminal velocity [ $\text{m s}^{-1}$ ] over the whole range is then given by:

$$U_t(R) = \begin{cases} 0; & R \leq 0.015 \text{ mm} \\ 4.323(R - 0.015); & 0.015 \leq R \leq 0.3 \text{ mm} \\ 9.65 - 10.3 \exp(-0.3R); & R > 0.3 \text{ mm} \end{cases} \quad (4.2)$$

#### 4.2.1.2 Rain droplet size distribution

We base our rain droplet size distribution on a gamma function fit of De Wolf (2001) to the pioneering size distribution measurements of Laws and Parsons (1943). We choose the gamma fit instead of the more traditional exponential function fit (Marshall and Palmer, 1948), because it represents the size distribution over the whole particle size spectrum whereas the exponential fits overestimate the number of droplets at the small end of the particle size spectrum. Making use of the droplet terminal velocity (equation 4.2), Mätzler (2002) properly normalized the De Wolf size

distribution. Normalization assures that the precipitation intensity computed from the droplet size distribution (equations 4.3) and their accessory speed of fall (equation 4.2) is consistent with the rain rate input variable,  $P$  (equations 4.3). The empirical expression for the number of drops with drop radii between  $R$  and  $R+dR$ , per unit volume of air, as a function of rain rate  $P$  is given:

$$N(R, P) = \text{norm} \cdot 1.98 \cdot 10^{-5} P^{-0.384} R^{2.93} \exp[-(5.38 \cdot P^{0.186} \cdot R)] \quad , \quad (4.3a)$$

where

$$\text{norm} = 1.047 - 0.0436 \cdot \ln P + 0.00734 \cdot (\ln P)^2 \quad . \quad (4.3b)$$

The adopted rain droplet size distribution ('De Wolf') is shown in Figure 4.1 for a precipitation intensity of  $5 \text{ mm hr}^{-1}$ .

#### 4.2.1.3 Raindrop-aerosol collection efficiency

The collision efficiency,  $E(R, r)$  expresses the probability that an aerosol particle that resides in the geometrical cylinder swept in a certain time interval by the cross-section of a falling rain droplet, actually collides with the droplet. We assume that every collision is efficient: the sticking efficiency or retention,  $\varepsilon$ , is unity (Pruppacher and Klett, 1997), in contrast to particle-particle collisions. The collection efficiency,  $\varepsilon E$ , is therefore equal to the collision efficiency. A value of  $\varepsilon E = 1$  implies that all particles in the geometric sweep-cylinder will be collected. In general  $\varepsilon E \ll 1$ , except for charged particles and very small Brownian particles (e.g. nanometer-sized particles formed by homogeneous nucleation) that are both not considered in our study. Theoretical solution of the Navier-Stokes equation for prediction of the collision efficiency for the general rain droplet-aerosol interaction case is a difficult undertaking due to the complicated induced flow patterns around the falling drop. Instead of exactly solving the Navier-Stokes equations we use an alternative expression for  $E$  that is based on dimensional analysis and experimental data (Slinn, 1984). The reader is referred to Seinfeld and Pandis (1998, their section 20.3.1) for a full description of the applied  $E$ .

The scavenging coefficient  $\beta$  as a function of aerosol particle radius and precipitation intensity is explicitly calculated using equation (4.1) and is shown in Figure 4.2. The dark blue/black area in the figure clearly identifies the well-known Greenfield gap, where aerosols are not effectively removed by falling rain droplets. The strong increase in the scavenging coefficient at particle sizes of about  $2 \mu\text{m}$  marks the transition to the size region where inertial impaction becomes the dominant contributor to the collection efficiency.

#### 4.2.2 Parameterization

To avoid the computationally expensive integration of equation (4.1) in our chemistry transport model, we fit an analytical function through the pre-calculated values of the scavenging coefficient for every aerosol particle radius; 1000 log-equidistant

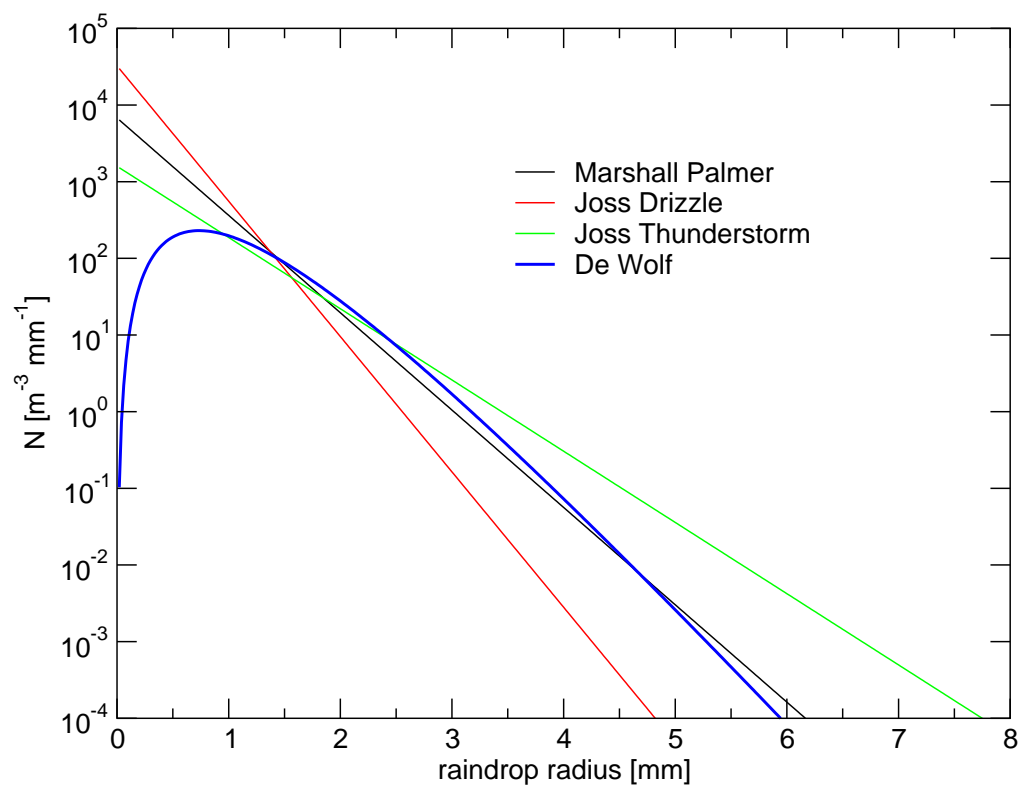


**Figure 4.1** The normalized rain droplet size distribution (precipitation intensity  $5 \text{ mm hr}^{-1}$ ), as used in our study (De Wolf) together with three other widely used size distributions (for a discussion see section 4.5.1).

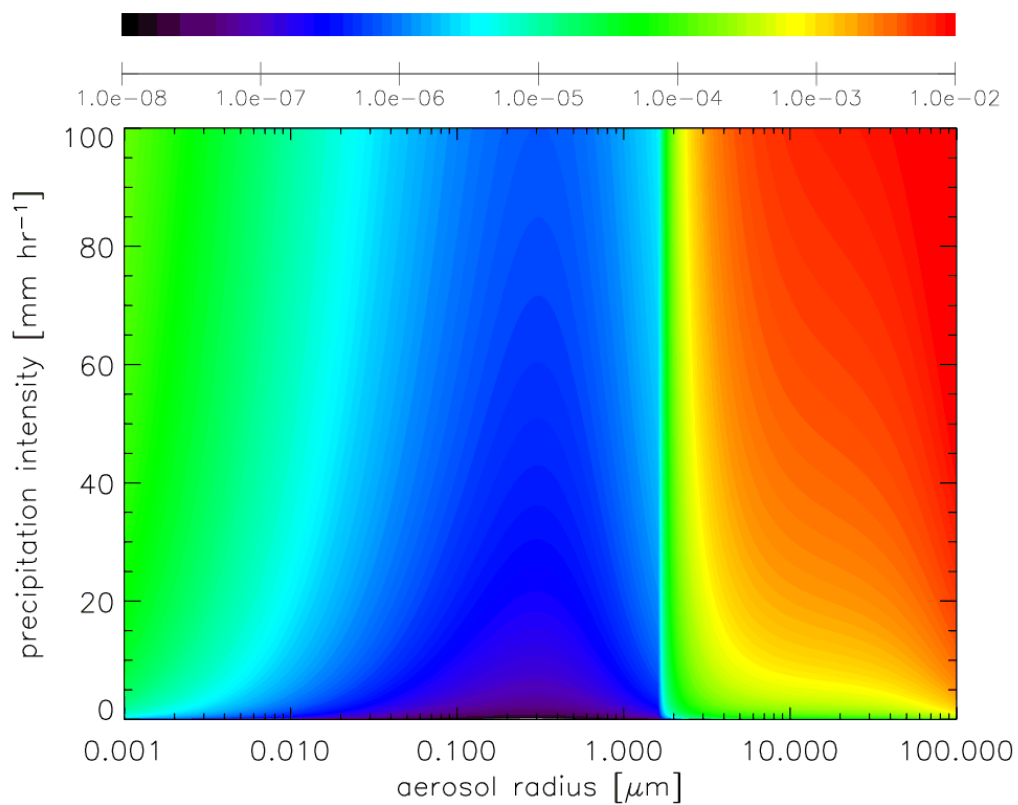


**Figure 4.2** Differential scavenging coefficient [ $\text{s}^{-1}$ ], scale is given in the color bar over the figure.

increments per order of magnitude increase in particle radius (Figure 4.2). A function of the form

$$\beta(P) = A_0 \left( e^{A_1 P^{A_2}} - 1 \right), \quad (4.4)$$

fits the data quite well and yields a scavenging coefficient for every aerosol particle radius that is only a function of the precipitation intensity. Using the fit function instead of an explicit integration over the rain droplet spectrum introduces errors such smaller than 1% except in a very small size region around 1  $\mu\text{m}$  (Figure 4.3).

### 4.3 Global chemistry transport model TM4

The global chemistry transport model TM (Heimann, 1995; Dentener et al., 1999) contains an aerosol module (Jeuken, 2000; IPCC, 2001) that will be used to investigate the impact of the developed below cloud scavenging parameterization. TM is a three-dimensional transport model coupled off-line to ECMWF meteorological fields. Here, we use version 4 of TM that mainly differs from older versions by improved meteorological parameters. This version contains parameterizations of convective (Tiedtke, 1989) and turbulent tracer transport (Holtslag and Boville, 1993; Vogelesang and Holtslag, 1996; Beljaars and Viterbo, 1999). Large scale advection of aerosol tracers is performed using the slopes scheme of Russell and Lerner (1981). We use a horizontal resolution of 6° in longitude and 4° in latitude. In the vertical the total number of hybrid  $\sigma$ -pressure levels (Simmons and Burridge, 1981) has been reduced from 60 (ECMWF) to 25 (TM4) by merging selected layers, mostly in the stratosphere. The scavenging parameterization will be evaluated for sea salt whose parameterization in the model was recently updated, as described below.

#### 4.3.1 Sea salt source function

A source for sea salt aerosol particles (Gong, 2003) that is based on the source function given by Monahan et al. (1986) has been included in the model. This source function, which is a function of the wind speed at 10-meter height ( $U_{10}$ ), provides the number of particles emitted in a certain size range per unit time and per unit sea surface. In our model the series of physical transport processes on sea salt aerosol are most conveniently formulated in terms of the dry part of the aerosol particles. Therefore, we have translated the source function, which is valid at 80% relative humidity (Monahan et al., 1983), in a dry particle source function using the size dependence of sea salt aerosol as a function of relative humidity given by Gerber (1985). To solve the size distribution both in number and mass it is sufficient to use 12 log-equidistant sectional bins (Gong et al., 2003). Our 12 bins cover the dry radius spectrum from 0.03  $\mu\text{m}$  to 10.0  $\mu\text{m}$ . Offline, we have calculated the sea salt mass emission [ $\text{kg s}^{-1}$  per unit sea surface] at 1  $\text{m s}^{-1}$  wind speed for every bin. The actual emissions are obtained by multiplication with  $U_{10}^{3.41}$  (Monahan et al., 1986). In the model, aerosol particles are assumed to be in a stable equilibrium size with respect to ambient relative humidity. The actual size of sea salt aerosol, which is used to calculate the below-cloud scavenging, is related to their dry size by the relationship of Gerber (1985).



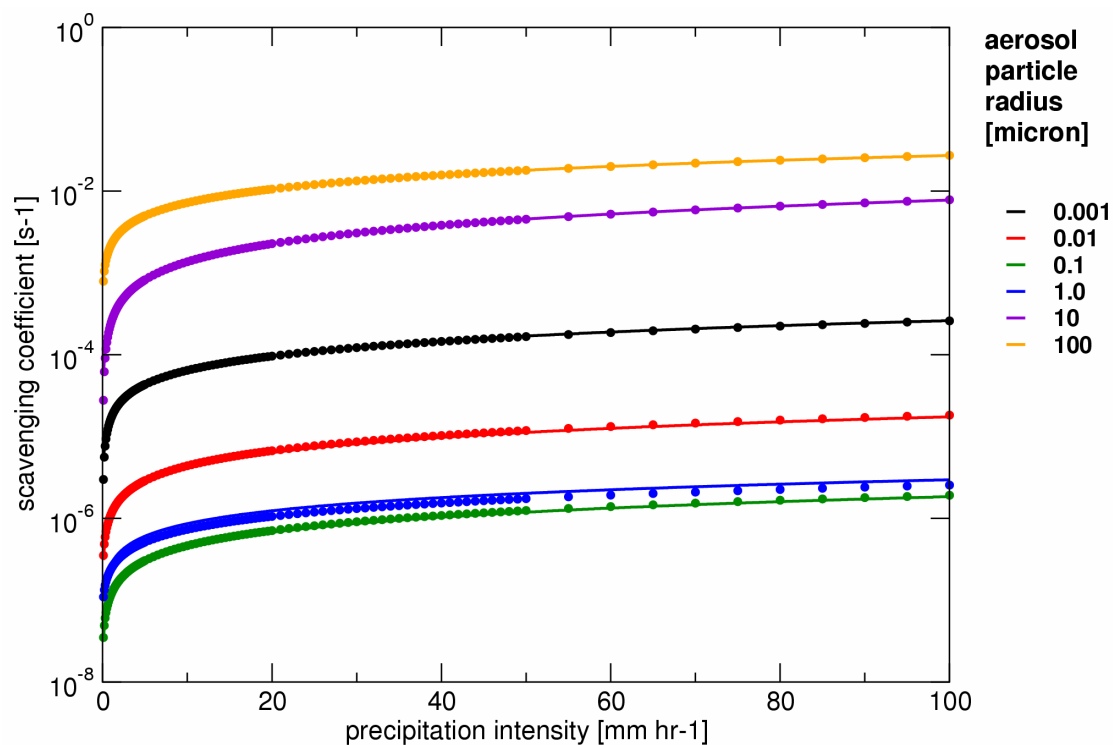


**Figure 4.3** Differential scavenging coefficients for a selection of aerosol radii (different colors). Full integrations of equation (4.1) are indicated by filled circles, results of the applied fit of equation (4.4) are indicated by full lines.

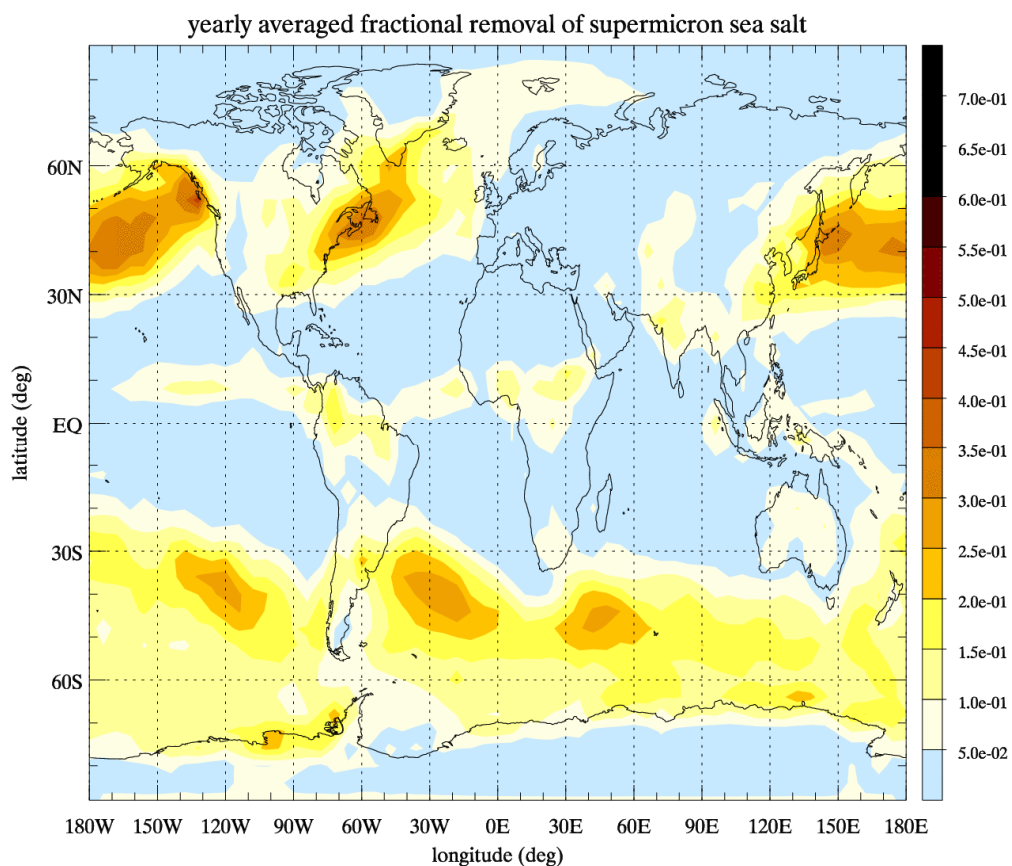


**Figure 4.6** Average fractional contribution of below-cloud scavenging to the total removal of super-micron sea salt aerosol for the year 2000.

### 4.3.2 Aerosol sinks

#### 4.3.2.1 Large scale cloud systems

The change in aerosol mass mixing ratio  $\mu$  due to the scavenging by precipitation can be obtained by applying an equivalent fractional loss term  $f$  that accounts for the subgrid-scale patchiness of precipitation (Walton et al., 1988):

$$\mu(t + \Delta t) = \mu(t) \cdot f \equiv \mu(t) \cdot (V_1 f_1 + V_2 f_2 + V_3) \quad , \quad (4.5)$$

where indices 1-3 represent respectively the region inside precipitating clouds, the region below precipitating clouds, and cloud free regions,  $V_i$  is the fraction of the grid cell occupied by region of type  $i$ , and  $f_i = \exp[-\beta_i \Delta t]$  where  $\Delta t$  is the time between two calls of the removal scheme. The assumption of an equivalent fractional loss term implicitly assumes that aerosols are uniformly distributed within each grid cell. We observed that when this scheme is applied at high temporal resolution, aerosol is removed too efficiently. The explanation is that it is implicitly assumed that aerosol is mixed from aerosol rich (cloud free) regions into aerosol poor (precipitating) regions after every removal step whereas in reality the precipitating systems still affect, for a large part, the same aerosol containing air mass. To overcome this problem, we effectively postpone the mixing. To do so we defined a no-mixing-timescale,  $\Delta t_{\text{no-mix}} = N \cdot \Delta t$ , and we reformulated the equivalent fractional loss term that then becomes a function of the number of calls,  $n$ , of the removal scheme since the last mixing instant:

$$f^*(n) = \frac{V_1 f_1^n + V_2 f_2^n + V_3}{V_1 f_1^{n-1} + V_2 f_2^{n-1} + V_3} \quad . \quad (4.6)$$

If we neglect all other processes but the removal scheme we find for  $n = N$ :

$$\mu(t + N\Delta t) = f^*(N) \cdot \mu(t + (N-1)\Delta t) \quad , \quad (4.7)$$

$$\mu(t + N\Delta t) = f^*(N) \cdot f^*(N-1) \cdot \dots \cdot f^*(1) \cdot \mu(t) \quad , \quad (4.8)$$

$$\mu(t + N\Delta t) = (V_1 f_1^N + V_2 f_2^N + V_3) \cdot \mu(t) \quad , \quad (4.9)$$

which equals the mixing ratio that would be obtained if air masses and precipitating clouds would be kept fixed at their relative positions for a time period  $\Delta t_{\text{no-mix}}$ . A convenient assumption for the no-mixing-timescale is the time between successive updates of the meteorological input, which is six hours in our model.

#### **Below cloud scavenging**

The *differential* scavenging coefficient,  $\beta(r)$ , obtained up to now, corresponds to a given, fixed aerosol particle radius. To derive an *integral* scavenging coefficient that is valid for the total aerosol mass contained within a certain size bin, equation (4.1)

has to be integrated over the aerosol particle mass distribution (Dana and Hales, 1976):

$$\beta(r_s) = \int_{r_l}^{r_r} \beta(r) f_{\text{mass}}(r) dr \quad , \quad (4.10)$$

where  $r_l$  and  $r_r$  are the left and right borders of the size bin,  $f_{\text{mass}}(r)dr$  is the mass probability distribution function (pdf), and subscript 's' indicates that the scavenging coefficient is obtained by integration over the aerosol mass *spectrum* that is contained in the size bin. Within a size bin the mass-pdf is unknown. As a first approximation we simply assume that the mass is equally distributed within a bin. The resolution with respect to aerosol radius of the parameterized differential scavenging coefficients is chosen such that the scavenging coefficient at the exact radius of the (wet) size bin borders can be obtained by linear interpolation of adjacent scavenging coefficients without introducing additional errors ( $\ll 1\%$ ).

### ***In-cloud scavenging***

The in-cloud scavenging coefficient is determined by two sequential steps: first the formation of cloud droplets from water vapor and second the conversion from cloud droplet to rain droplet. We neglect the existence of interstitial aerosol and thus assume that all aerosol particles act as condensation nuclei. The second step, that thus fully determines the removal process, is captured by calculation of the precipitation formation rate (Roelofs and Lelieveld, 1995). The actual scavenging coefficient is the fraction of cloud water that is converted into rain water per unit of time.

#### **4.3.2.2 Dry deposition**

Dry deposition, the amount of material deposited to a unit surface area per unit time,  $F$ , is calculated as:

$$F = -v_d C \quad , \quad (4.11)$$

where  $C$  is the concentration [ $\text{kg m}^{-3}$ ] and the constant of proportionality,  $v_d$ , with units of length per unit time is the deposition velocity. The dry deposition velocity of aerosol particles is a function of turbulent state of the atmosphere and of particle aerodynamic size. Based on theoretical considerations Slinn and Slinn (1980) derived an expression for the deposition velocity,

$$v_d = \frac{(v_a + v_g)(v_b + v_g)}{(v_a + v_b + v_g)} \quad , \quad (4.12)$$

where  $v_a$ ,  $v_b$ , and  $v_g$  are velocities. Velocity  $v_a$ , represents the rate of material transport by turbulence from a reference height in the free troposphere to a layer of stagnant air just above and adjacent to the surface (quasi-laminar sublayer). In our model  $v_a = 1/r_a$ , where  $r_a$  is the aerodynamic resistance that is calculated and stored at ECMWF. Analogously, the transfer velocity in the quasi-laminar sublayer is written  $v_b = 1/r_b$ , where  $r_b$  is the resistance to transfer which depends upon Brownian diffusion accounted for by the Schmidt number ( $Sc$ ), and upon inertial impaction, accounted for by the Stokes number ( $St$ ) (Slinn, 1982):

$$r_b = \frac{1}{u_* \left( Sc^{-2/3} + 10^{-3}/St \right)} \quad , \quad (4.13)$$

where  $u_*$  is the friction velocity,  $Sc = \nu/D$ , where  $\nu$  is the kinematic viscosity and  $D$  the Brownian diffusion and  $St = \nu_g u_*^2 / g \nu$ , where  $g$  is the gravitational acceleration. The gravitational settling velocity is given by Stokes Law,

$$\nu_g = \frac{4\rho_p r_p^2 g}{18\mu}, \quad (4.14)$$

where  $\rho_p$  is the density of the particle,  $r_p$  is the particle radius,  $\mu$  is the viscosity of air.

#### 4.3.2.3 Convective cloud systems

The scavenging by convective precipitation is proportional to the mass flux entrained in convective clouds, as in Balkanski et al. (1993) and Guelle et al. (1998). We apply rather arbitrary scavenging efficiencies of 50% for shallow convection up to 700 hPa and of 80% for deep convection. Furthermore, we include an exponential scaling factor to avoid removal in the case of relatively dry updrafts. In the absence of precipitation there is no removal, for a precipitation intensity of 1 mm/hr the scaling is 0.85, and for higher intensities the scaling rapidly goes to 1 (no scaling).

## 4.4 Results

### 4.4.1 Emission, load, and lifetime

Applying our model with the newly implemented sea salt source function (Gong 2003), we find for the year 2000 a total sea salt mass emission of 2,440 Tg for particles with dry radii between 0.03 and 10  $\mu\text{m}$ . This value falls well within the range of estimates reported in the literature (1,000 to 3,000 Tg/yr, Erickson and Duce, 1988; 5,900 Tg/yr, Tegen et al., 1997) and can be compared to the current best estimate of 3,300 Tg/yr for sea salt particles with dry radii between 0.03 and 8  $\mu\text{m}$  that is given in IPCC (2001). Super-micron (sub-micron) aerosol particles by definition have diameters larger (smaller) than 1 $\mu\text{m}$ . Super-micron (sub-micron) mass emissions add to 2.390 (48) Tg/yr, which agrees with the ranges of 1,000 to 6,000 (18 to 100) Tg/yr provided by IPCC (2001). In Figure 4.4 we show the seasonal variations of global and hemispheric monthly emissions in our model. The strong seasonal variations in both the northern and southern hemisphere agree with the findings of Gong et al. (2002).

Guelle et al. (2001) used the Monahan et al. (1986) source function for sea salt to estimate a mean annual global mass-load of 0.5 and 10.6 Tg for sub- and supermicron (cut off at 4 $\mu\text{m}$  radius) sea salt, respectively. Using the Gong-Monahan source, that mainly differs from the original Monahan source function at small particle sizes, which make up only a small fraction of the total mass, we find for size ranges corresponding to Guelle et al. global mean loads of 0.5 and 6.1 Tg for submicron and supermicron aerosol, respectively. For the whole size range we find 9.8 Tg which can be compared to Guelle et al. (2001) who have 12.7 Tg.

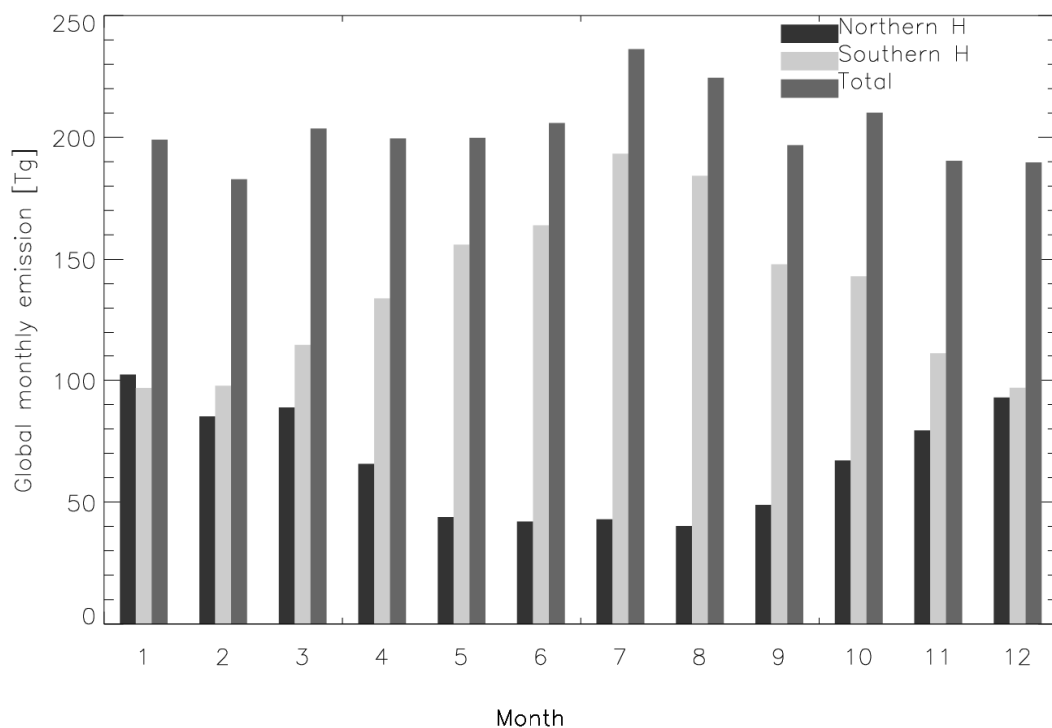


**Figure 4.4** Simulated monthly variations of global and hemispheric emissions for the year 2000.

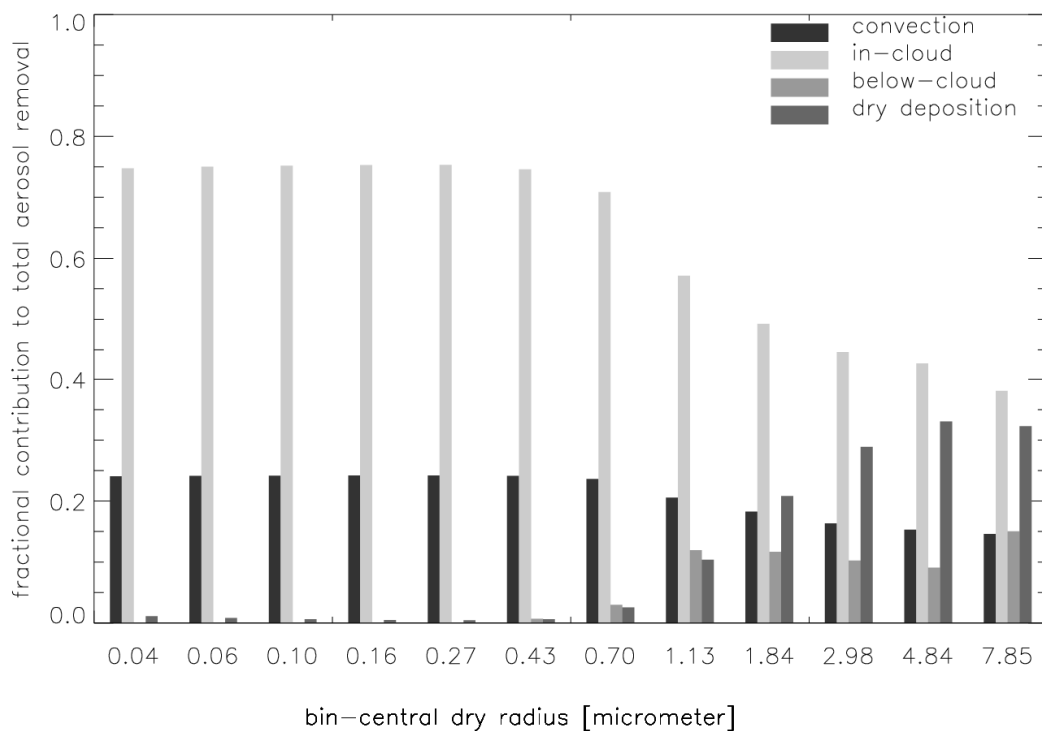


**Figure 4.5** Relative importance of different removal mechanisms for sea salt aerosols presented as a global-average for the year 2000. The log-central radii of the 12 (dry) sea salt bins are given in micrometer. ‘in-cloud’ here refers to large scale systems without convection.

For IPCC (2001) six models with prescribed sea salt sources were run to estimate global burdens. Using these estimates the average sea salt lifetime for the whole size range is 2.1 days (varying between 0.8 and 4.55 days). Our estimate of 2.16 days is in close agreement with these values.

#### 4.4.2 Partitioning between below-cloud scavenging and other sinks

For the 12 dry sea salt tracers global-average fractional contributions of dry deposition (dry), removal in convective cloud systems (convective), removal by large-scale clouds (in-cloud), and below-cloud scavenging by falling raindrops (below-cloud) to the total aerosol removal are shown in Figure 4.5. For sub-micron particles removal is governed by cloud processes with in-cloud dominating over convective; below-cloud scavenging thus being unimportant. For super-micron sea salt the individual fractional contributions to the total removal are 0.29, 0.16, 0.43, and 0.12 for dry, convective, in-cloud, and below-cloud removal, respectively. All considered removal processes thus contribute significantly to the total removal of super-micron aerosol.

In Figure 4.6 (p. 64) the global distribution of the relative contribution of below-cloud scavenging to the total sea salt removal is shown. At mid-latitudes in both hemispheres below-cloud scavenging is regionally the dominant sink for super-micron sea salt. The maximum below-cloud scavenging contributions coincide with yearly averaged maxima in sea salt emissions. A removal process that acts so efficiently in the vicinity of source regions may very efficiently prevent the tracer from being transported to other regions. It is therefore tempting to hypothesize that ignoring the below-cloud scavenging process would have an even stronger effect on the global average aerosol lifetime than can be expected from the global fractional contribution of the below-cloud scavenging to the total removal. However, below we will show that this is not the case. Aerosol lifetime  $\tau$ , can be defined as the ratio of the atmospheric burden of aerosol to its emission. For sufficiently long run time periods, a few months or longer, emission is balanced by removal. Total removal is the sum of all individual removal processes so that the inverse of the overall lifetime can be written as the sum of the inverse lifetimes of each of the individual removal processes:

$$\frac{1}{\tau_{\text{tot}}} = \frac{1}{\tau_{\text{dry}}} + \frac{1}{\tau_{\text{convective}}} + \frac{1}{\tau_{\text{in-cloud}}} + \frac{1}{\tau_{\text{below-cloud}}} \quad , \quad (4.15)$$

where individual lifetimes are defined as the ratio of the atmospheric burden to the removal caused by the individual process. The total lifetime and the contributions to it by the individual processes are shown in Table 4.1. When all processes are considered, the total atmospheric lifetime  $\tau_{\text{tot}}=2.16$  days. If one of the processes would not occur the total atmospheric lifetime would increase. The increase in total atmospheric lifetime can thus also be inferred from model simulations with individual removal processes switched off. Running TM4 without below-cloud scavenging, we find  $\tau_{\text{tot}}=2.47$ . If we use, equation (4.15) to predict the total atmospheric lifetime in the absence of below-cloud scavenging from the model simulation that includes all removal processes and the simulations with the individual other removal processes switched off., we also find  $\tau_{\text{tot}}=2.47$  days. This confirms the validity of equation (4.15) and implies that the individual lifetimes or individual fractional contributions to total removal can directly be compared to assess their relative importance.

**Table 4.1** Aerosol lifetimes,  $\tau$ , for super-micron sea salt particles for model simulations with and without the below-cloud scavenging parameterization. Subscripts ‘dry’, ‘below-cloud’, ‘in-cloud’, and ‘convective’ refer to dry deposition, below cloud scavenging, scavenging in large scale clouds, and scavenging by convective clouds, respectively.

Process	All Removal Processes		No Below-cloud scavenging	
	Lifetime	Fractional contribution total removal	Lifetime	Fractional contribution total removal
Dry	7.43	0.29	7.77	0.32
Below-cloud	17.43	0.12	—	—
In-cloud	5.07	0.43	4.85	0.51
Convective	13.64	0.16	14.38	0.17
Total	2.16	1.00	2.47	1.00

## 4.5. Remaining uncertainties

We have parameterized the scavenging of aerosol particles by falling rain droplets and have shown that for particles with diameters larger than one micrometer below cloud scavenging is an important process to be included in models, especially when the modeling objective is to simulate aerosol mass (rather than number). We also made it plausible that the new parameterization itself (i.e. the fit through pre-calculated scavenging coefficients and conversion from differential scavenging coefficients to integral scavenging coefficients that are valid for an aerosol size bin) is quite accurate numerically. So far, however, we have not yet discussed physical uncertainties e.g. related to the choice of the rain droplet spectrum or particle humidity growth. Below we give an overview of the most relevant issues.

### 4.5.1 Rain droplet spectrum

Differential scavenging coefficients depend strongly on the choice of the rain droplet size distribution. The gamma distribution we have chosen may be representative for global average continuous rainfall. However, it is unlikely that the rain droplet distributions of individual precipitating systems are properly described with this distribution. Therefore, we also determined the differential scavenging coefficients using equation (4.1) with the three other rain droplet size distributions that are shown in Figure 4.1. The ‘Marshall Palmer’ distribution is the widely used exponential fit of Marshall and Palmer (1948) to the Laws and Parsons (1943) data that is also used by De Wolf (2001). Droplet distributions associated with drizzle and precipitation from thunderstorms are dominated by small and large droplets, respectively. The Joss (Joss et al., 1968) ‘drizzle’ and ‘thunderstorm’ exponential distributions (Figure 4.1) can be expected to indicate extremes in this case. However, De Wolf (2001) found that a gamma function fit to the data (Laws and Parsons, 1943) represents the measurements at the small end of the droplet range ( $R < 0.5$ -1mm) better than exponential functions that predict maximum droplet number concentration for droplets with sizes approaching zero diameter. Therefore, the distribution used in this study has fewer small rain droplets, which are very effective aerosol collectors, than the other distributions shown in Figure 4.1. Results from the ‘drizzle’ distribution pretty much resembled our results, but the ‘Marshall Palmer’ and ‘Thunderstorm’ distributions yielded scavenging coefficients that were a factor of 3 and 5, respectively, higher over

the whole range of precipitation intensities and for all aerosol particles sizes. The central plus the additionally investigated distributions do not encompass the whole range of possible rain droplet size distributions (for an overview see Pruppacher and Klett, 1997) so that deviations could potentially be even larger. Moreover, the distributions are the same everywhere below precipitating clouds, whereas it is known that large differences in rain droplet spectra may occur between cloud base and surface due to e.g. breakup and evaporation of large droplets and coagulation of droplets. It is not possible to produce reliable rain droplet size distributions with our model, nor can we integrate the aerosol and rain droplet size distributions to obtain the scavenging coefficients online. As yet it is thus not possible to get around the droplet size distribution problem. This would require an explicit microphysical package to be included which for the moment is numerically too expensive for our model.

### 4.5.2 Particle humidity growth

Another possible source of uncertainty is the growth of particles with increasing humidity. For the water uptake of sea salt particles we applied a relation provided by Gerber (1985). In our model sea salt is externally mixed with other aerosol particles. Applying the Gerber relation implicitly assumes that the composition of our sea salt resembles that of the Navy Aerosol Model (NAM). In reality, sea salt particles may act as a substrate for heterogeneous chemistry and will therefore be internally mixed to some extent (Dentener and Crutzen, 1993). Internal mixing of sea salt particles with continental pollution and organic compounds reduces their hygroscopic growth rate (Swietlicki et., 2000; Randles et al., 2004). For below-cloud scavenging this may become important for aerosol particles with radii around 1 or 2  $\mu\text{m}$  where the differential scavenging coefficient grows very rapidly with increasing aerosol particle size. Keeping track of internal mixtures combined with online particle humidity growth calculations is not foreseen in our model in the near future, but it is in principle possible. A related issue is the accuracy of the relative humidity itself, especially at high relative humidity. At the coarse resolution used here ( $6^\circ \times 4^\circ$ ) a single, using only an average, value of the relative humidity in each cell is a poor representation of the spatial variability of relative humidity. The large changes in relative humidity fields that are experienced between successive meteo updates, especially in situations with precipitation, indicates that the model neither represents temporal variability well. Moreover relative humidity may not be accurately predicted below precipitating clouds. The importance of uncertainties related to relative humidity may be best demonstrated with an example: The aerosol mass of a sea salt particle with dry radius 1  $\mu\text{m}$  will be underestimated by a factor 2 if the ambient relative humidity of 90% is underestimated at 80%, the corresponding underestimate in the differential scavenging coefficient is more than a factor of 20.

### 4.5.3 Precipitation and evaporation

Below-cloud scavenging is directly proportional to the precipitation intensity. Uncertainties in precipitation intensity stem from uncertainties in the distribution of precipitation in time and space and in the calculated precipitation formation rates. Firstly, precipitation is assumed to be distributed uniformly over the cloud covered fraction within the grid cell and over the period between two meteo updates. In reality



it may not rain continuously; some of the clouds in the domain may not precipitate at all and thus leave the aerosol unaffected. Our precipitation intensities will thus likely be biased towards lower values. For lower intensities, the rain drop size distribution will consist of more and smaller-sized droplets that scavenge aerosols more easily. Together this will overestimate removal of aerosol particles by below-cloud scavenging. Secondly, the precipitation formed in a grid cell is (almost) always larger than the precipitation intensities at the surface given by the ECMWF data. Part of this difference may be explained by evaporation. Therefore, we scale our precipitation formation rates with ECMWF surface precipitation implicitly handling the evaporation of rain droplets. Uncertainties in ECMWF precipitation will thus directly translate to uncertainties in below-cloud scavenging. Moreover, when falling rain droplets evaporate the aerosol particles that resided in the droplet are released. In our approach the aerosol is released within the cloud and aerosols remain prone to in-cloud scavenging. However, in reality most of the evaporation will take place below cloud base and aerosols are only scavenged by falling rain droplets. Evaporation of falling rain droplets may be an effective downward transport mechanism for aerosol and once properly accounted for may increase the relative contribution of below-cloud scavenging compared to that of in-cloud scavenging. In a (near) future version of the model evaporation fields stored experimentally by ECMWF will be used to investigate this issue further.

## 4.6 Conclusions

A size dependent parameterization for the removal of aerosol particles by falling rain droplets has been developed. The parameterization has been applied in the global chemistry transport model TM4 and the relative importance of below-cloud scavenging relative to other removal mechanisms has been investigated. To investigate the impact of below-cloud scavenging we have adopted a source for sea salt aerosol (Gong, 2003). A scheme with 12 log-equidistant bins covering the dry aerosol spectrum from 0.03 to 10.0  $\mu\text{m}$  keeps track of the aerosol size distribution. We have shown that our modeled results fall well within the range of current models, but we have not explicitly evaluated the removal parameterization. The reason is that such an evaluation is complicated by the fact that the emission source function has not been validated either. In fact, currently feasible comparisons against observed atmospheric concentrations rather validate the whole chain of emissions, transport, and removal mechanisms in a specific model (Gong, 2003). The same would apply here; a comparison of model atmospheric fields obtained with the new parameterization against measurements may yield good agreement by canceling errors. We therefore like to stress the urgency of performing dedicated field experiments addressing sources and sinks of sea salt aerosols jointly.

For a full year run (year 2000), we find that for particles with diameter larger than 1  $\mu\text{m}$ , below-cloud scavenging is as important as the removal in convective updrafts and that below-cloud scavenging accounts for 12% of the total yearly average removal. At mid-latitudes of both hemispheres the fractional contribution of below-cloud scavenging to the total removal is about 30% with regional maxima exceeding 50%. The maxima in relative importance of below-cloud scavenging coincide with maxima in emissions. Excluding the below-cloud scavenging process would result in an increase of global average aerosol lifetime from 2.16 days to 2.47 days

Despite uncertainties in the obtained deposition by below-cloud scavenging by uncertainties in precipitation, relative humidity, and particle humidity growth, we conclude that below cloud scavenging is likely an important sink for super-micron sized sea salt aerosol particles. The same conclusion would not necessarily hold for other super-micron sized particles such as e.g. desert dust. Desert dust is produced in arid areas under dry conditions. Therefore, dust is lifted and transported from its source regions and resides generally in the lower free troposphere, whereas coarse mode sea salt remains in the boundary layer.



# 5

## Global aerosol modeling with TM4 – application to the aerosol optical depth over Europe

### 5.1 Introduction

In chapter 2 the importance of aerosols for our climate system has been discussed. Whatever aerosol-climate interaction is to be investigated, the (global) three dimensional distribution of aerosols is needed. Here, we describe a model that is capable to give this distribution. Furthermore, the model contains a module that converts aerosol mass into aerosol optical depth. Both aerosol mass and aerosol optical depth are compared to ground based observations to test the skill of the model.

### 5.2 Transport Model TM4

For the aerosol modeling we use version 4 of three-dimensional global chemical transport model TM (Heimann, 1995; Dentener et al., 1999). The model version used in this study contains sulfate, nitrate, ammonium, 4 different carbonaceous, and 12 sea salt aerosol tracers (Henzing et al., 2005). Parameterizations are used to calculate convective mass fluxes (Tiedtke, 1989) and vertical turbulent diffusion (Holtslag and Boville, 1993; Vogelesang and Holtslag, 1996; Beljaars and Viterbo, 1999). Large scale advection of aerosol tracers is performed using the slopes scheme of Russell and Lerner (1981). We use a horizontal resolution of  $6^\circ$  in longitude and  $4^\circ$  in latitude. In the vertical the total number of hybrid  $\sigma$ -pressure levels (Simmons and Burridge, 1981) has been reduced from 60 (ECMWF) to 25 (TM), mainly by merging levels in the upper atmosphere.

#### 5.2.1 Emissions

Annual totals and spatial distributions of anthropogenic  $\text{NO}_x$ ,  $\text{NH}_3$ ,  $\text{SO}_2$ , and CO emissions have been taken from the  $1^\circ \times 1^\circ$  EDGAR-V2.0 emission inventory (Olivier, 1996; Van Aardenne et al., 2001). Monthly mean seasonal cycles of biomass burning emissions are taken into account (Hao and Liu, 1994; Hao et al., 1991) and the seasonal variations in industrial and fossil fuel related  $\text{NO}_x$  and  $\text{SO}_2$  emissions are based on the GEIA data base (Benkovitz et al., 1996). Hydrocarbon emissions from EDGAR-V2.0 and GEIA databases are lumped into the corresponding CBM-4

compound representation (Gery et al., 1989; Houweling et al., 1998). NO<sub>x</sub> aircraft emissions are taken from the ANCAT/EC2 data base (Gardner, 1998). Soil NO<sub>x</sub> emissions, that are also included in the EDGAR-V2.0 data base, are taken from the inventory of Yienger and Levy (1995). NH<sub>3</sub> emissions from soil under natural vegetation and from oceans are taken from EDGAR-GEIA (Bouwman et al., 1997). Annual total and spatial distribution of natural oceanic CO emissions are based on the work of Bates et al. (1995) and Erickson (1989) as described by Houweling et al. (1998). Total CO emissions from vegetation, based on the work of Bauer et al. (1979), have been scaled to the global distribution of net primary production as derived from the climate assessment model IMAGE (Minnen et al., 1996; Kreileman, 1996). SO<sub>2</sub> emissions from continuously degassing volcanoes are taken from Andres and Kasgnoc (1998). Natural SO<sub>2</sub> and DMS land-emissions are taken from Spiro et al. (1992). Using the parameterization for ocean-air exchange of Liss and Merlivat (1986), the measurement-based compilation of DMS concentrations in surface water on a 1°×1° grid of Kettle and co-workers (Kettle et al., 1999; Kettle and Andreae, 2000) is translated into fluxes. Natural VOC emissions (including isoprene) are taken from the GEIA data base (Guenther et al., 1995).

## 5.2.2 Chemistry

TM4 describes full tropospheric chemistry of HO<sub>x</sub>-NO<sub>x</sub>-SO<sub>x</sub>-CO-CH<sub>4</sub> and Non Methane Hydro Carbons (NMHC's) using a modified version of the CBM-4 scheme (Houweling et al., 1998). To calculate photolysis rates we use the scheme of Krol and Van Weele (1997). The sulfur cycle (Jeuken, 2000; Metzger et al., 2002b) is fully coupled to the photochemistry code. In our model version all oxidants as well as heterogeneous reaction rates of N<sub>2</sub>O<sub>5</sub> on preexisting aerosol surface resulting in the formation of HNO<sub>3</sub> (Dentener and Crutzen, 1993) are explicitly calculated. Gas and cloud phase reactions of SO<sub>2</sub>, DMS, NH<sub>3</sub>, SO<sub>4</sub><sup>2-</sup> and NH<sub>4</sub><sup>+</sup> are incorporated (Dentener and Crutzen, 1994). For a complete list of all other gas phase reactions the reader is referred to Houweling et al. (1998). In total 55 atmospheric constituents are considered, of which 21 gaseous and 19 aerosol tracers are transported. 110 gas phase reactions and 24 photolysis reactions are taken in account.

## 5.3 Aerosol module

### 5.3.1 Aerosol sources

Sulfate aerosol is mainly produced from gas-phase and aqueous-phase oxidation of SO<sub>2</sub> and DMS. Only a very small fraction of the sulfur emissions is directly emitted as sulfate (2% in our model). Ammonium and nitrate aerosol is formed when low volatile precursor gases condensate. The gas-particle partitioning of the sulfate-ammonium-nitrate system, which depends on the amount of precursor gases but also strongly on the ambient relative humidity and temperature, is accounted for by a simplified thermodynamic equilibrium model (EQSAM, Metzger et al., 2002a). The main assumption of this model is that aerosols are internally mixed and obey thermodynamic gas-aerosol equilibrium. For global modeling this assumption is adequate as the time required for gas-aerosol equilibration is much shorter than the model timestep (Metzger et al., 2002a). To increase the computational efficiency of

EQSAM the total number of equilibrium reactions is minimized by making use of concentration domains that contain fewer species than the entire set of possible aerosol compositions (Nenes et al., 1998, Metzger et al., 2002a). Critical for the aerosol composition is the amount of  $\text{NH}_3$  plus  $\text{NH}_4^+$  (total ammonia). The mole ratio of total ammonia to total sulfate, which defines the domains, determines the sulfate state, i.e. non-neutralized  $\text{H}_2\text{SO}_4$  or neutralized  $\text{HSO}_4^-$  or  $\text{SO}_4^{2-}$ . Only for a surplus of total ammonia, ammonium nitrate salts will be formed. The actual gas-aerosol partitioning only occurs for the ammonium nitrate salts; the other ammonium salts and sulfuric acid are treated as nonvolatile and they remain in the aerosol phase.

Four types of carbonaceous aerosol are considered. We differentiate between organic carbon (OC) and black carbon (BC). Both OC and BC can be hydrophobic or hydrophilic. Hydrophobic aerosol will neither be activated as cloud condensation nuclei, nor will it be scavenged by precipitation. BC is predominantly emitted as hydrophobic aerosol, but a small fraction of the emissions may be hydrophilic (Cachier, 1998). We assume that 80% of the BC emissions are hydrophobic and 20% is hydrophilic as is common in other models. OC is emitted in equal proportions of hydrophobic and hydrophilic aerosol in accordance with Cooke et al. (1999). The sources of BC and OC sub-micron aerosol particles were taken from the work of Cooke et al. (1999). They provide global-scale emissions of carbonaceous aerosol from fossil fuel usage with a horizontal resolution of  $1^\circ \times 1^\circ$ . The quantity of carbonaceous aerosol emitted by fossil fuel combustion is proportional to the quantity of fuel consumed and the emission factor for the combustion process. The quantity of fuel consumed is reasonably well known (e.g. United Nations, 1993). The distinction between BC and OC emission factors for the Cooke et al. (1999) emission data, is based on fuel type (e.g. diesel, kerosene, coal, gas), consuming sector (domestic, transport, and industry), and level of development of the country. The emissions are equally spread over the year.

A source for sea salt aerosol particles (Gong, 2003) that is based on the source function given by Monahan et al. (1986) is included in the model (Henzing et al., 2005). We translate the source function, which is valid at 80% relative humidity (Monahan et al., 1983), in a dry particle source function using the size dependence of sea salt aerosol as a function of relative humidity given by Gerber (1985). We solve the size distribution by using 12 log-equidistant sectional bins that cover the dry radius spectrum from  $0.03 \mu\text{m}$  to  $10.0 \mu\text{m}$ . We calculated the emission [ $\text{kg s}^{-1} \text{m}^{-2}$ ] in every bin for  $1 \text{ m s}^{-1}$  wind speed at 10 m height ( $U_{10}$ ). The actual emission is obtained by scaling with  $U_{10}^{3.41}$  (Monahan et al., 1986). In the model, aerosol particles always reach a stable equilibrium size with respect to ambient relative humidity. The actual size of sea salt aerosol, which is used to calculate the below-cloud scavenging, is obtained from their dry size by applying the relationship of Gerber (1985).

### 5.3.2 Aerosol sinks

Aerosols are removed from the (model) atmosphere by (1) collision with the surface (dry deposition), (2) by acting as cloud condensation nuclei or collision with cloud- and rain droplets inside clouds that are finally brought to the surface as precipitation (in-cloud scavenging and convective scavenging), and (3) by collision with and adherence to falling rain droplets that are subsequently deposited to the surface (below-cloud scavenging).

### 5.3.2.1 Dry deposition

In the widely used formulation for dry deposition that is also adopted in the TM4 model (Henzing et al., 2005, Chapter 4), the amount of material depositing to a unit surface area per unit time,  $F$ , is directly proportional to the local concentration,  $C$ , of the species,

$$F = -v_d C \quad , \quad (5.1)$$

where the constant of proportionality,  $v_d$ , with units of length per unit time is known as the deposition velocity. Based on theoretical considerations Slinn and Slinn (1980) derived an expression for the deposition velocity,

$$v_d = \frac{(v_a + v_g)(v_b + v_g)}{(v_a + v_b + v_g)} \quad , \quad (5.2)$$

where  $v_a$ ,  $v_b$ , and  $v_g$  are velocities. In our model  $v_a$  is inversely proportional to the aerodynamic resistance that is calculated and stored at ECMWF. Analogously, velocity,  $v_b$  is inversely proportional to the resistance to transfer which depends upon Brownian diffusion and inertial impaction (Slinn, 1982). The gravitational settling velocity,  $v_g$  is given by Stokes Law.

### 5.3.2.2 In-cloud scavenging and convective scavenging

For large scale precipitating systems, the change in aerosol mass mixing ratio  $\mu$  due to the scavenging by precipitation is obtained by applying an equivalent fractional loss term  $f$  that accounts for the subgrid-scale patchiness of precipitation (Walton et al., 1988):

$$\mu(t + \Delta t) = \mu(t) \cdot f \quad , \quad (5.3)$$

where  $\Delta t$  is the time between two calls of the removal scheme and  $f = \exp[-\beta \Delta t]$  where  $\beta$  is the scavenging coefficient. The assumption of an equivalent fractional loss term implicitly assumes that aerosols are uniformly distributed within each grid cell. We observed that when this scheme is applied with a high temporal resolution, aerosol is removed too efficiently. To overcome this problem, we effectively postpone the mixing (see Henzing et al., 2005, Chapter 4) for the period equal to the time between successive meteo updates, which is six hours in our model.

The in-cloud scavenging coefficient for large scale precipitating systems is determined by two sequential steps: first the formation of cloud droplets from water vapor and second the conversion from cloud droplet to rain droplet. In earlier versions of our model, we neglected the existence of interstitial aerosol. All aerosol particles, except for the hydrophobic carbonaceous particles, thus acted as condensation nuclei. The conversion from cloud droplet to rain droplet that is captured by calculation of the precipitation formation rate (Roelofs and Lelieveld, 1995) then fully determined the removal process. The actual scavenging coefficient is the fraction of cloud water that is converted into rain water per unit of time. In the new version of our model we take into account interstitial aerosols. At mid-latitudes, most tropospheric clouds are mixed-phase clouds in which supercooled liquid drops and ice crystals coexist (Pruppacher and Klett, 1997). These clouds precipitate solid particles. Except for the

hydrophobic carbonaceous aerosol, all aerosols act as CCN in our model. However, it is known that ice crystals form on a small subset of the aerosol population. These ice crystals grow by collision with supercooled droplets or by condensational growth at the expense of the supercooled droplets. The aerosols either remain prone to removal, but now via the ice-phase, or they are released as interstitial aerosol due to the evaporation of supercooled droplets. Henning et al. (2004) investigated aerosol partitioning between cloud and interstitial phases in natural, mid-latitude, mixed-phase clouds using in situ measurements. They concluded that the growth of ice crystals by transfer of water vapor from supercooled droplets, which occurs if the environment is super-saturated with respect to the ice phase but sub-saturated with respect to liquid water, becomes increasingly important with decreasing cloud temperatures. The fact that their observed fraction of interstitial aerosol is rather insensitive to particle sizes, allows us to use their numbers to estimate the amount of aerosol mass that remains interstitial, and that is therefore not removed from our model atmosphere. For warm clouds Henning et al. (2004) also provide an estimate of the fraction of aerosol that remains interstitial, we also use that value. For four temperature regimes the fractions of aerosol that remain interstitial are given in Table 5.1.

The scavenging by convective precipitation is proportional to the mass flux entrained in convective clouds (Balkanski et al., 1993; Guelle et al., 1998). We apply scavenging efficiencies of 50% for shallow convection up to 700 hPa and of 80% for deep convection. Furthermore, we include an exponential scaling factor to avoid removal in the case of relatively dry updrafts. In the absence of precipitation there is no removal, for a precipitation intensity of 1 mm/hr the scaling is 0.85, and for higher intensities the scaling rapidly goes to 1 (no scaling).

### 5.3.2.3 Below-cloud scavenging

The below-cloud scavenging coefficient for secondary inorganic salts and hydrophilic carbonaceous aerosols is deduced from the work of Dana and Hales (1976). They give theoretical mass rainout coefficients integrated over the rain droplet and aerosol size spectra. The scavenging coefficient is the product of the local rain flux and the mass rainout coefficient normalized to unit rainfall rate, which is  $0.05 \text{ mm}^{-1}$  for the chosen frontal rain spectrum and lognormal aerosol distribution (Jeuken, 2000, and references therein).

The below-cloud scavenging coefficient for sea salt aerosol is a function of aerosol particle size. For this purpose a size dependent parameterization for the removal of aerosol particles by falling rain droplets is developed. Scavenging coefficients are calculated explicitly as a function of aerosol particle size and precipitation intensity

**Table 5.1** Fraction of aerosol particle mass that is not incorporated in cloud droplets (interstitial aerosol) as a function of cloud temperature, based on Henning et al., 2004.

Cloud temperature [°C]	Interstitial aerosol fraction
-20 to -15	0.08
-15 to -10	0.14
-10 to -5	0.29
-5 and higher	0.54



including the full interaction of rain droplet size distribution and aerosol particles. The actual parameterization is an accurate three-parameter fit through these pre-calculated scavenging coefficients. The parameterization accounts for the water uptake of sea salt particles using a relationship provided by Gerber (1985). For a full description of the parameterization and the relative importance of below-cloud scavenging compared to other aerosol removal mechanisms as a function of particle size, the reader is referred to Henzing et al. (2005, Chapter 4). Hydrophobic carbonaceous aerosol particles are not removed by falling rain droplets.

### 5.3.3 Aerosol optical parameters

The optical depth  $\tau$  in layer  $k$  is given by:

$$\tau(k) = g^{-1} \int_{p_k}^{p_{k+1}} \sum_i \chi_i q_i dp \quad (5.4)$$

Here  $i$  is an index for aerosol species,  $\chi_i$  is the extinction cross section per unit mass for specie  $i$ , [ $\text{m}^2 \text{kg}^{-1}$ ],  $q_i$  is the aerosol mixing ratio [(kg aerosol)/(kg air)],  $p_k$  ( $p_{k+1}$ ) is the pressure at the bottom (top) of layer  $k$ , and  $g$  the acceleration due to gravity [ $\text{m s}^{-2}$ ]. Total aerosol optical depth is given by the summation over all vertical layers. For the conversion of aerosol mass to aerosol optical depth, the extinction cross sections per unit mass are thus required. For a known dry aerosol particle size distribution, water uptake as a function of relative humidity, and mixing state of the different aerosol species,  $\chi_i$  can be calculated. Here, we follow an approach similar to Kiehl et al. (2000) and we perform the calculation offline, in order to avoid numerically expensive online calculations. For all species, a dry log-normal size distribution is prescribed. For relative humidities varying between 0% and 100%, we calculate the ‘hydrated’ size distributions using appropriate prescribed water uptake functions. To each of the hydrated size distributions we closely fit a new log-normal distribution. For the composite particles that comprise the hydrated size distribution, we calculate the refractive index using an effective medium approximation. We finally obtain the extinction cross sections by using the hydrated size distribution and the accompanying refractive index as input for a Mie calculation.

#### 5.3.3.1 Hydrophobic carbonaceous aerosol

Hydrophobic organic carbon (OC) and black carbon (BC) aerosols are fresh combustion products. The size of these particles depends on the combustion process and the fuel used. Here we tentatively assume that all particles reside within a log-normal size distribution that is described by a median radius  $r_g = 0.02$  and geometric standard deviation  $\sigma = 2.0$ . For black carbon the real part of the refractive index  $m_r = 1.75$  and the imaginary part of the refractive index  $m_i = -4.4e^{-3}$  (Hess et al., 1998). For organic carbon  $m_r = 1.75$  and  $m_i = -4.4e^{-3}$  (Gelencsér, 2004; Lioussé et al., 1996). Using a Mie code (De Rooij and Van de Stap, 1984), we find for hydrophobic aerosols that do not accrete water,  $\chi_{BC} = 10.7 \text{ m}^2 \text{ g}^{-1}$  and  $\chi_{OC} = 2.3 \text{ m}^2 \text{ g}^{-1}$ . For the refractive index used for organic and black carbon,  $\chi_{OC}$  and  $\chi_{BC}$  decrease if the geometrical standard deviation of the log-normal size distribution is decreased. For example, for  $\sigma = 1.5$ , the cross sections are  $\chi_{OC} = 0.56 \text{ m}^2 \text{ g}^{-1}$  and  $\chi_{BC} = 9.00 \text{ m}^2 \text{ g}^{-1}$ , which equals the estimate for black carbon of Lioussé et al (1996). If the hydrophobic particle size distribution would have a smaller median radius, the extinction cross section would have been even smaller, e.g. for  $r_g = 0.01$  and  $\sigma = 1.5$ ,  $\chi_{OC} = 0.09 \text{ m}^2 \text{ g}^{-1}$

and  $\chi_{BC} = 6.40 \text{ m}^2 \text{ g}^{-1}$ . In the latter case, hydrophobic organic carbonaceous particles would not contribute to the aerosol optical thickness. Since the conversion from modeled aerosol mass to aerosol optical thickness is linear, the aerosol optical thickness of black carbon would have been about 40% lower in that case. If the hydrophobic particle size distribution would be better described by a larger median radius, the extinction cross section would be larger. In remote regions, Clarke et al. (1997) measured the particle number size distributions after heating the aerosol-containing air up to 300 °C. They interpreted the remaining, refractory, number distributions as the distribution of cores on which volatile fine particle mass had condensed. If these cores exist of either BC or OC then the refractory number distribution could provide another estimate of the hydrophobic particle size distribution. Converting their ‘refractory’ size distribution to a log-normal distribution we find,  $r_g = 0.03$ . Keeping  $\sigma$  at 2.0 we find  $\chi_{OC} = 3.6 \text{ m}^2 \text{ g}^{-1}$  and  $\chi_{BC} = 10.9 \text{ m}^2 \text{ g}^{-1}$ . In the latter case, the extinction due to hydrophobic black carbon would only change slightly as compared to our estimate. The aerosol optical thickness of organic carbon would then be about 55% higher. Evidently, the uncertainties in the extinction cross sections per unit mass are large.

### 5.3.3.2 Internal mixtures of carbonaceous and secondary inorganic aerosols

Hydrophilic OC and BC are ‘impure’ carbonaceous particles that contain species other than the fresh combustion products hydrophobic OC and BC. These impurities mainly consist of sulfates, ammonium and nitrates, also denoted by secondary inorganic aerosols (SIAs). The process that is responsible for the impurities in the first place controls the ratio of the amount of SIA to the amount of carbonaceous material, but it also controls the internal distribution within the composite particle. If the internal mixture is formed by coagulation of SIA aerosols and fresh hydrophobic carbonaceous particles, by condensation of sulfuric- and nitric acid on pre-existing carbonaceous particles, or by gas-to-particle heterogeneous nucleation onto a carbonaceous particle, the result would be a coated aerosol with the hydrophobic carbon particle at the core and the SIA species in a shell around it. On the other hand, if the internal mixture is formed from the evaporation of cloud droplets, then a more or less well-mixed matrix of substances would be the result. For simplicity, we assume here that the various carbonaceous and SIA species are homogeneously mixed within the composite particle. This assumption implies that cloud-cycling, i.e. aerosols are incorporated in cloud or rain droplets and released by evaporations several times, is important and that the refractory size distributions should be interpreted as the amount of carbonaceous material that is mixed into the composite particles. For the internal mixture of components a mixing rule is needed to compute the composite refractive index. Chylek et al. (1996, 2000) discussed the importance of using an appropriate effective medium approximation for the determination of the optical properties of heterogeneous particles. The best mixing rule will depend on the geometric arrangement of the components comprising the mixture. However, for typical atmospheric aerosol, composite refractive indices are rather insensitive to the choice of mixing rule and hence a simple volume-weighted average of the individual refractive indices can be used (Lesins et al., 2002).

In our calculations the distribution of the hydrophilic OC and BC composite particles is described by a log-normal size distribution with a geometric mean radius  $r_g = 0.05$  and a geometric standard deviation  $\sigma = 2.0$ . The volume fraction of OC and BC in all the individual particles of the distribution is given by the fractional contribution of the

OC and BC volume, occupied by a log-normal distribution with  $r_g = 0.02$  and  $\sigma = 2.0$ , to the total volume of the composite particle distribution. The remainder of the volume is occupied by SIAs. The fractional contributions of the various SIAs to the impure part of the composite hydrophilic carbonaceous particles are determined by the EQSAM model as described above. If insufficient SIA is available, which sometimes occurs for carbonaceous rich regions over warm land surfaces, the amount of OC and BC in the composite particles is increased (see Table 5.2). The water uptake of hydrophilic OC and BC is supposed to be similar to that of urban aerosol (Gerber, 1985). Using the method described in the first paragraph of this section, we calculate the mass extinction cross sections per unit dry mass for relative humidities varying between 0-100%. Through the calculations we closely fit a function of the form  $y = \exp[(A_0 + A_1 \cdot X)/(A_2 + A_3 \cdot X)]$  (Figure 5.1, top and middle). The fit parameters are given in Table 5.3 for the carbonaceous aerosol types defined in Table 5.2.

### 5.3.3.3 Pure secondary inorganic aerosol

For the sulfate-ammonium-nitrate system, the dry log-normal size distribution is expressed by a geometric mean radius  $r_g = 0.05$  and a geometric standard deviation  $\sigma = 2.0$  (Jeuken, 2000, Kiehl et al., 2000). The water uptake of these inorganic aerosols, expressed as a function of relative humidity and particle size, is similar to that of ammonium bi-sulfate (Gerber, 1985). The density of dry inorganic salts is  $1760.3 \text{ kg m}^{-3}$  and the  $m_r = 1.53$  and  $m_i = -6.0e^{-3}$  (Hess et al., 1998). For pure water,  $m_r = 1.333$  and  $m_i = -1.96e^{-9}$ . The water, sulfate, nitrate, and ammonium masses are equally distributed over all particles that comprise the hydrated size distribution and each particle consists of a homogeneous mixture of solutions. Therefore, a simple volume-weighted average of the individual refractive indices can be used to calculate the refractive index of the composite particles. The calculations and the fit of the form  $y = \exp[(A_0 + A_1 \cdot X)/(A_2 + A_3 \cdot X)]$  are shown in Figure 5.1 (bottom). The fit parameters are listed in Table 5.3.

### 5.3.3.4 Sea salt aerosol

For sea salt aerosol the mass extinction cross section  $\chi_{salt}$  is explicitly calculated as a function of relative humidity for each of the twelve size bins. For the Mie calculations

**Table 5.2** Applied internal mixtures of secondary inorganic salts (sulfate-ammonium-nitrate) and hydrophilic organic/black carbon. Size distribution parameters  $r_g$  (median radius) and  $\sigma_g$  (geometrical standard deviation) for the dry composite particle. The mass and volume fractions indicate the fractions of carbonaceous material within each of the individual particles of the size distribution. High, very high, and extremely high refer to carbonaceous aerosol mass concentrations that are relatively high, very high, and extremely high (respectively) as compared to secondary inorganic salts mass concentrations.

Type	$r_g$	$\sigma_g$	Mass fraction carbon	Volume fraction carbon
Standard	0.02	2	0.03	0.05
High	0.03	2	0.15	0.24
Very high	0.04	2	0.40	0.54
Extremely high	0.45	2	0.61	0.73
Pure carbonaceous	0.50	2	1.00	1.00

**Table 5.3** Fit parameters A0-A3 for sulfate-ammonium-nitrate system and for different internal mixtures of sulfate-ammonium-nitrate and black and organic carbon (see Table 5.2).

Aerosol Type	A0	A1	A2	A3
Sulfate-ammonium-nitrate	1.68769	-1.32746	1.17381	-1.10237
Standard BC	1.67128	-1.41704	1.16146	-1.11010
high BC	1.84137	-1.60648	1.13939	-1.09321
Very high BC	2.09148	-1.87676	1.10825	-1.06772
Extremely high BC	2.24292	-2.03647	1.09016	-1.05216
Pure BC	2.45818	-2.25941	1.06538	-1.03012
Standard OC	1.63821	-1.37635	1.16624	-1.11318
High OC	1.68978	-1.41765	1.16166	-1.10731
Very high OC	1.78476	-1.49344	1.15325	-1.09655
Extremely high OC	1.85540	-1.55060	1.14686	-1.08862
Pure OC	1.97447	-1.64887	1.13580	-1.07542

of the extinction efficiencies, the sea salt mass in each size bin is centered on the log-central radius of the bin. In order to find smooth relationships between aerosol mass and relative humidity, we adopted a narrow log-normal number distribution, so that major maxima and minima in the extinction efficiency (due to interference of light diffracted and transmitted by the sphere particles) are conserved but ripples (that arise from edge rays that are grazing and traveling the particles, spewing off energy in all directions) are avoided. The water uptake of sea salt is taken from Gerber (1985). The density of dry sea salt is  $2170 \text{ kg m}^{-3}$  and  $m_r = 1.50$  and  $m_i = -1.00 \text{ e}^{-8}$  (Shettle and Fenn, 1979). In Figure 5.2, the extinction cross section per unit wet sea salt mass is shown for the 12 bins. Through the calculated extinction cross sections we fitted polynomials. The fitted functions and their corresponding parameters are given in Table 5.4. Note that the decrease in  $\chi_{salt}$  for some of the bins does not mean that the extinction decreases with increasing relative humidity, since water uptake more than compensates for the decrease in  $\chi_{salt}$ .

**Table 5.4** Polynomials fitted through calculated extinction cross sections per unit wet sea salt mass together with their parameters.

Bin central- radius	Fitted formula $y(x) =$	A0	A1	A2	A3	A4	A5	A6	A7	A8	A9
0.0382	$(a_0x+a_1x+a_2x^2+a_3x^3)^{-1}$	3.5461	-3.7711	2.8909	-2.5807						
0.0620	$(a_0x+a_1x+a_2x^2+a_3x^3)^{-1}$	0.9185	-1.5576	2.1705	-1.4809						
0.1006	$(a_0x+a_1x+a_2x^2+a_3x^3)^{-1}$	0.2326	-0.1006	0.0376	-0.1219						
0.1633	9 <sup>th</sup> order polynomial	1.1506e <sup>+1</sup>	-6.7984e <sup>+1</sup>	1.7247e <sup>+3</sup>	-1.7551e <sup>+4</sup>	9.2733e <sup>+4</sup>	-2.8022e <sup>+5</sup>	5.0216e <sup>+5</sup>	-5.2713e <sup>+5</sup>	2.9922e <sup>+5</sup>	7.0873e <sup>+5</sup>
0.2650	7 <sup>th</sup> order polynomial	1.4562e <sup>+1</sup>	-4.7187	1.4353e <sup>+2</sup>	-9.8229e <sup>+2</sup>	3.3069e <sup>+3</sup>	-5.8258e <sup>+3</sup>	5.1356e <sup>+3</sup>	-1.7860e <sup>+3</sup>		
0.4300	3 <sup>rd</sup> order polynomial	1.0077e <sup>+1</sup>	-1.7063	9.0938	-1.4865e <sup>+1</sup>						
0.6977	3 <sup>rd</sup> order polynomial	3.4966	-6.5119	2.1926e <sup>+1</sup>	-1.6515e <sup>+1</sup>						
1.1322	3 <sup>rd</sup> order polynomial	2.3880	-3.0924	8.8326	-6.7139						
1.8372	3 <sup>rd</sup> order polynomial	1.3659	-0.6206	3.5481	-3.5525						
2.9813	3 <sup>rd</sup> order polynomial	0.8595	-0.3979	1.7906	-1.7828						
4.8377	3 <sup>rd</sup> order polynomial	0.5255	-0.3293	1.2711	-1.1867						
7.8502	3 <sup>rd</sup> order polynomial	0.3180	-0.1917	0.7547	-0.7116						

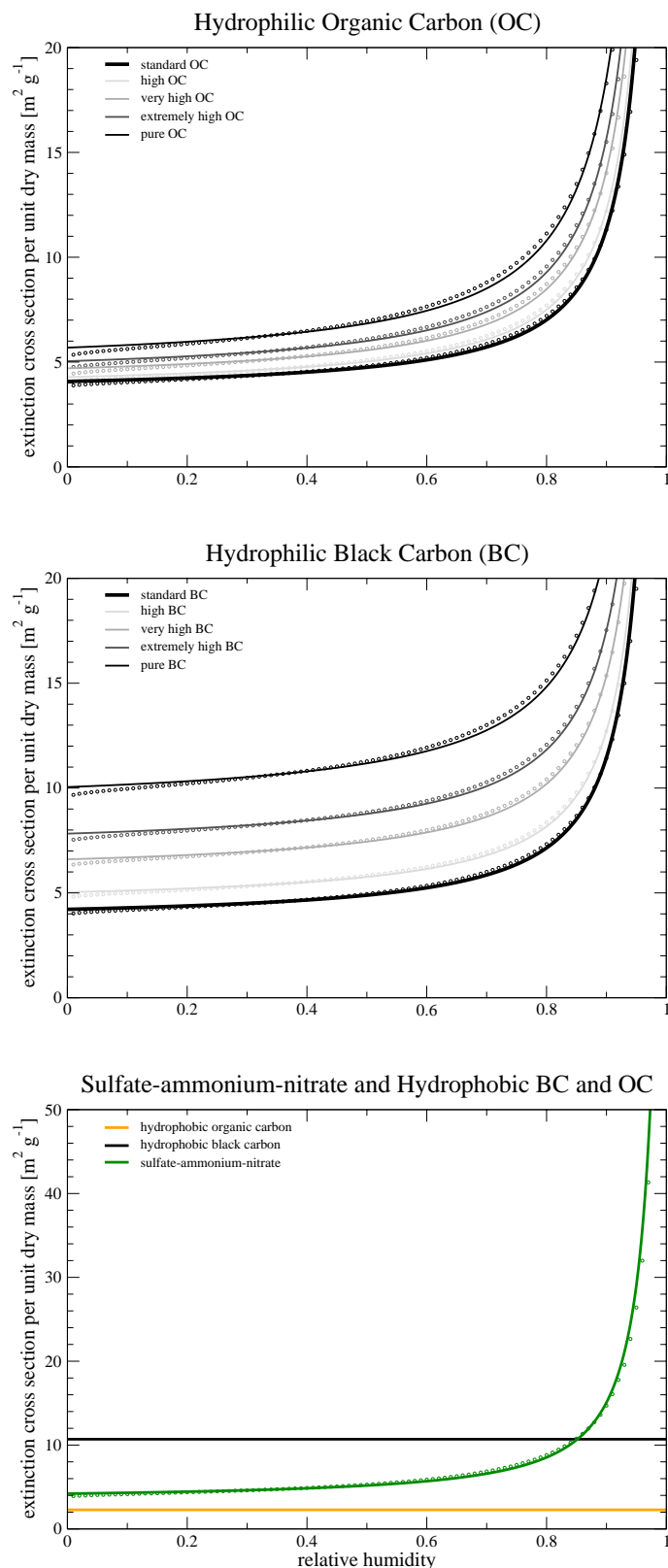


**Figure 5.1** Calculated (circles) and fitted values (straight lines) of the extinction cross section per unit dry mass  $[\text{m}^2 \text{g}^{-1}]$  as a function of ambient relative humidity. (top) Hydrophilic organic carbon for various internal mixtures. (middle) Hydrophilic black carbon for various internal mixtures. (bottom) Pure sulfate-ammonium-nitrate and hydrophobic black and organic carbon.

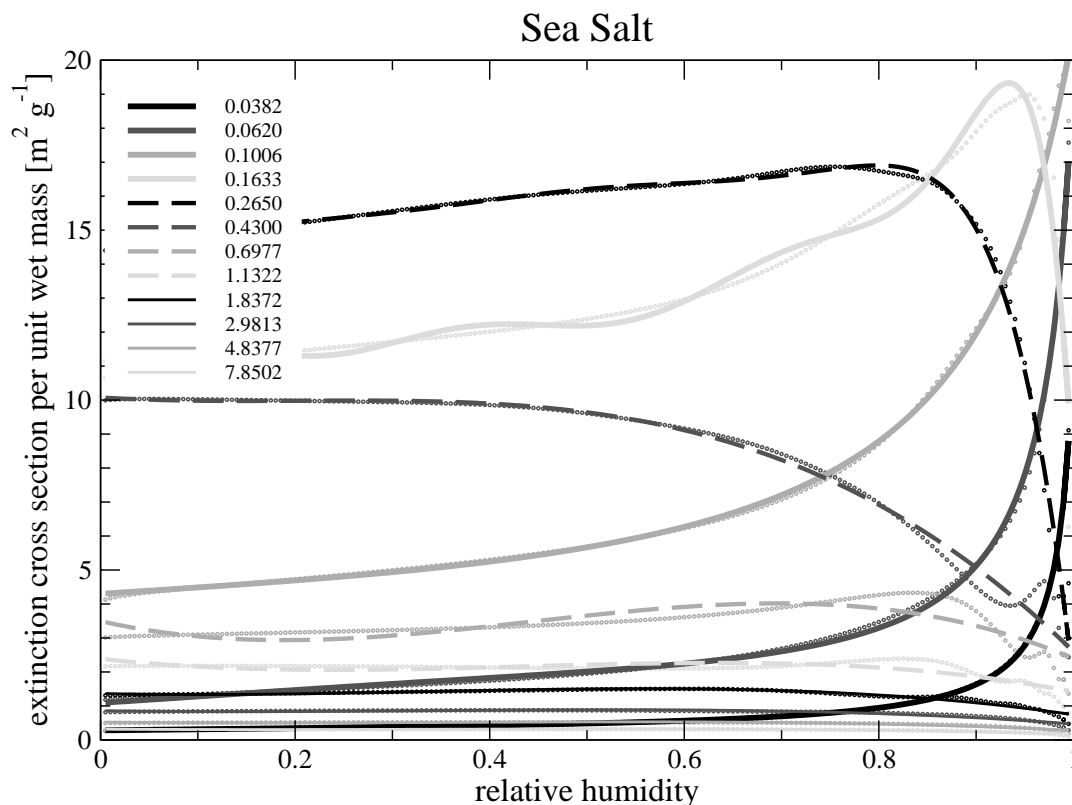


**Figure 5.2** Calculated (circles) and fitted values (straight lines) of the extinction cross section per unit humidified sea salt mass [ $\text{m}^2 \text{g}^{-1}$ ] as a function of ambient relative humidity for the 12 bin-central dry radii.

## 5.4 Application to Europe – comparison to observations

The TM4 model can provide an estimate of the aerosol optical depth on a global scale. Except for Saharan dust aerosols, which are episodically important over the Mediterranean, all relevant aerosol species that contribute to the aerosol optical depth over Europe are included. Here, we select a large area including Europe (30W-48E; 30N-78N) to evaluate the models' capability to predict the aerosol optical depth.

The spatial distribution of the yearly average AOD for the year 2000 is shown in Figure 5.3 (top left). What catches the eye is the area with high aerosol optical depths over the eastern part of the domain. These yearly average high values are predominantly caused by high values in the winter period that last until March (Figure 5.3, top right). A possible explanation may be that aerosols are built up in a stable winter boundary layer from which escape is hampered due to the blocking inversion. This also happens over other parts of Europe but there depression activity more often washes out the aerosol. In spring and summer the highest aerosol optical depths occur over central Europe (Figure 5.3, bottom panels), but these maxima are less pronounced.

The partitioning of the aerosol optical depth over the various species is shown in Figures 5.4. For the yearly average, we find that sea salt and secondary inorganic

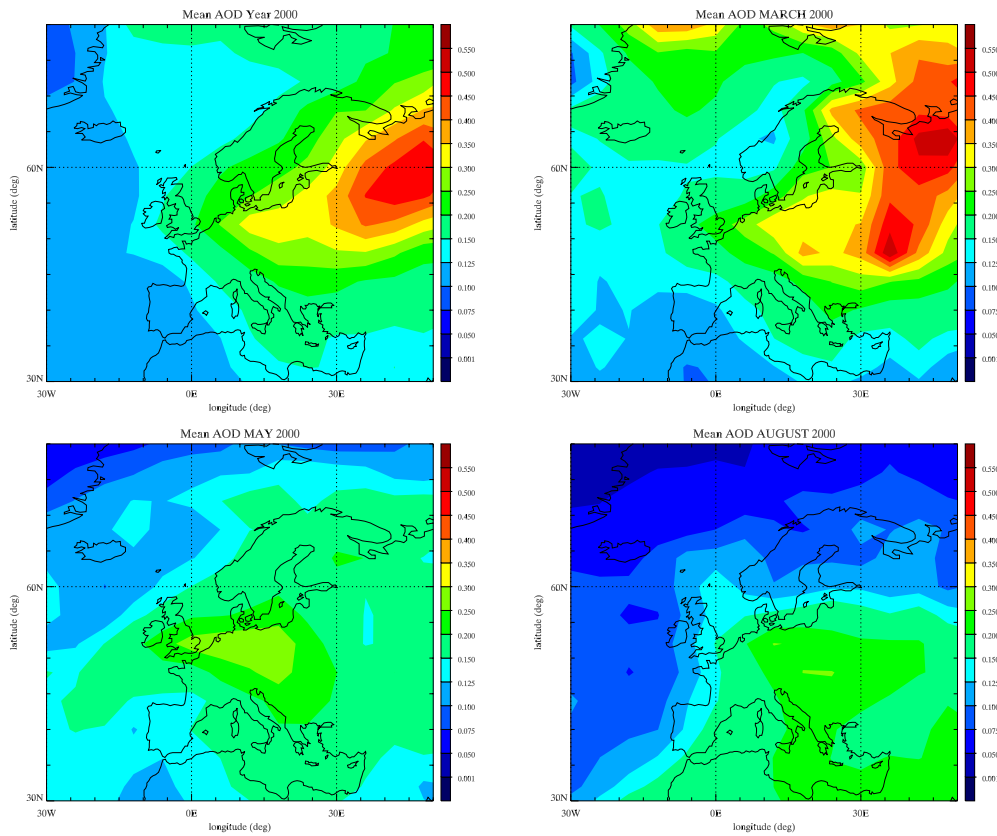


**Figure 5.3** Spatial distribution of the aerosol optical depth. (top left) Yearly mean. (top right) March. (bottom left) May. (bottom right) August.

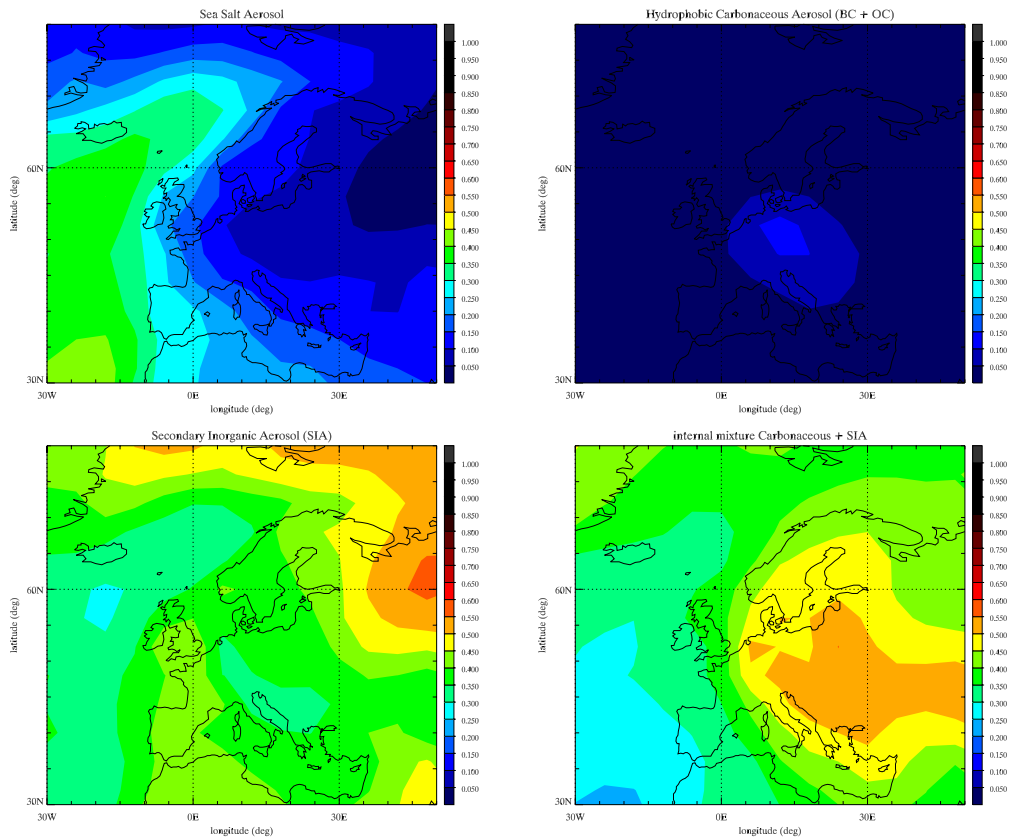


**Figure 5.4** Spatial distribution of the yearly-average fractional contribution of the various aerosol species to the total aerosol optical depth. (top left) Sea salt (top right) Hydrophobic black and organic carbon. (bottom left) Secondary Inorganic aerosol salts. (bottom right) Hydrophilic black and organic carbon.



aerosols are almost equally important over the Atlantic Ocean. The aerosol optical depth over the Norwegian Sea and the northern parts of Russia is dominated by secondary inorganic aerosols. The internal mixtures of carbonaceous and secondary inorganic aerosols are the main contributors to the aerosol optical depth over Central and Central-East Europe. The fractional contributions of the various species for individual months are not shown here but are briefly described below. For the month of March they do not substantially differ from the yearly average. In the month May, sea salt becomes less important even over the ocean, and the hydrophilic carbons become the dominant contributor to the aerosol optical depth except for the Iberian Peninsula and northern Africa where secondary inorganic aerosols contribute most to the AOD. The patterns for the month of August strongly resemble those of May. The maximum in the contribution of secondary inorganic aerosols to the aerosol optical depth forms a bridge between two regions, one dominated by sea salt over the ocean and the other dominated by hydrophilic carbonaceous aerosols over land. For all months the contribution to the AOD of hydrophobic BC and OC is small everywhere except for central Europe where the contribution more than 5% and locally close to 20%.

In Figure 5.5, the fractional contributions of the various species to the aerosol optical depth are given per month and spatially integrated over the selected domain. The contribution of hydrophobic BC and OC is smaller than 3% in all months, with the maximum contribution in (late) summer. The hydrophilic carbonaceous aerosols are the dominant contributors to the optical depth for a large part of the year. Only in winter the pure secondary inorganic aerosols dominate. The difference between the two contributors is largest in spring and summer. The occurrence of this yearly cycle cannot be explained by the emissions of aerosols and their precursor gases, but is most likely caused by the aerosol-gas partitioning of the secondary inorganic aerosols. In winter, lower temperatures prevail that cause a quicker condensation of the SIA precursor gases. This means that in winter compared to carbonaceous material relatively more SIA is available. In our model secondary inorganic aerosols are used to form the internal mixture, what is 'left over' is pure SIA. Note that only the contribution of this externally mixed SIA to the total optical depth is represented in Figure 5.5. This explains the occurrence of this yearly cycle in the fractional contributions of the SIA and hydrophilic carbonaceous species, and the cycle might be expected to be independent of the absolute value of the aerosol optical depth. The sea salt contribution varies between a minimum value of about 6% in August to a maximum of 18% in March. The temporal variability in sea salt load and thus sea salt aerosol optical depth is source driven, whereas for the other species the load is mainly determined by the sinks. The peak in sea salt aerosol optical depth that occurs in March in 2000, as well as its maximum fractional contribution, can therefore in other years occur in other winter months, as the occurrence of storms shows substantial interannual variability. The maximum aerosol optical depths of the other species are caused by long fair weather periods, which may occur in any season, although some high pressure systems have a preference, e.g. the Siberian winter High.

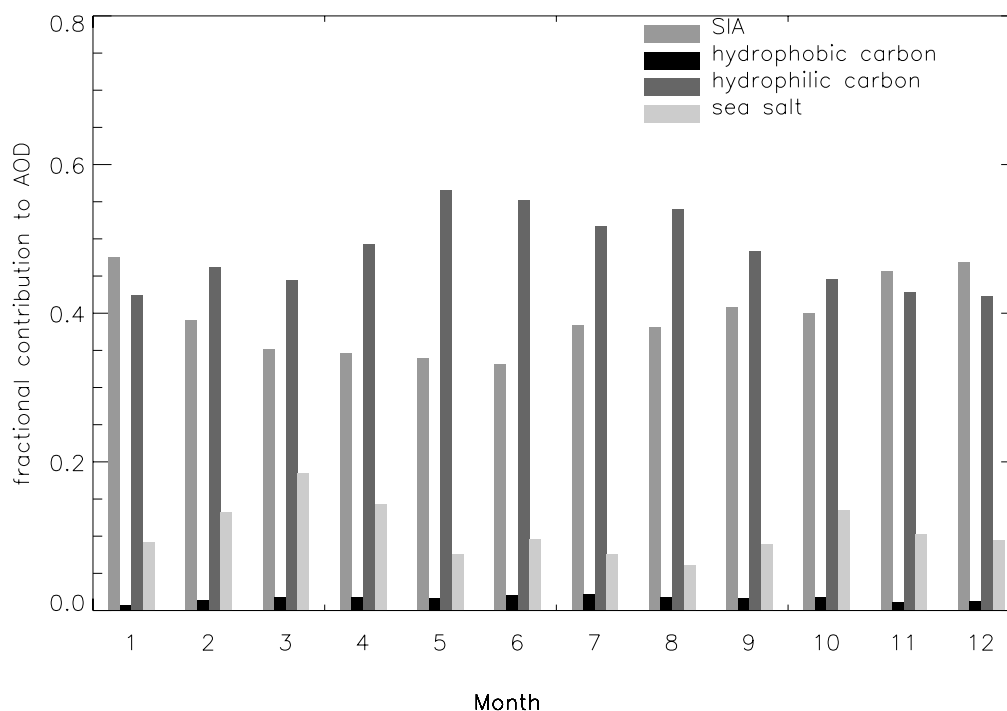


**Figure 5.5** Yearly variation of the fractional contribution of the various aerosol species to the total aerosol optical depth.

### 5.4.1 Comparison to AERONET observations

Here, we compare our modeled aerosol optical depths to ground based aerosol optical depth observations that are made available by AERONET (AERosol RObotic NETwork, Holben et al., 1998). For this purpose the AERONET aerosol optical depth at 550 nm is estimated from the AOD at measured wavelengths (440, 670, 870 and 1020 nm) using the provided Ångstrom exponent that is valid for the closest two enveloping wavelengths. For the year 2000, all simultaneous modeled aerosol optical depths and a selected set of AERONET observations of aerosol optical depth are compared. The selected stations are listed in Table 5.5.

For the year 2000, the average modeled aerosol optical depth at all stations is 0.19 and the standard deviation of the distribution,  $\sigma_{\text{dis.}}=0.13$ . If only the modeled values are used when AERONET observations are available, the average simulated aerosol optical depth reduces to 0.17 ( $\sigma_{\text{dis.}}=0.06$ ); to be compared to the AERONET average AOD of 0.20 ( $\sigma_{\text{dis.}}=0.15$ ). The model thus clearly underestimates the aerosol optical depth. When different periods are selected, this underestimation is found to be a persistent feature (Table 5.6). To explain it, we individually compare all simultaneous modeled and observed aerosol optical depths. In Figure 5.6 (left), the AERONET AOD values together with the simultaneous modeled AOD values are given as a function of the modeled values. From this figure we conclude that the persistent underestimation of the mean AOD is not caused by a systematic underestimation of all modeled values. Rather, high modeled AOD values are not supported by high observed AOD values and the other way around, and at the same time high observed AOD values are not accompanied by high modeled values. The same figure but with

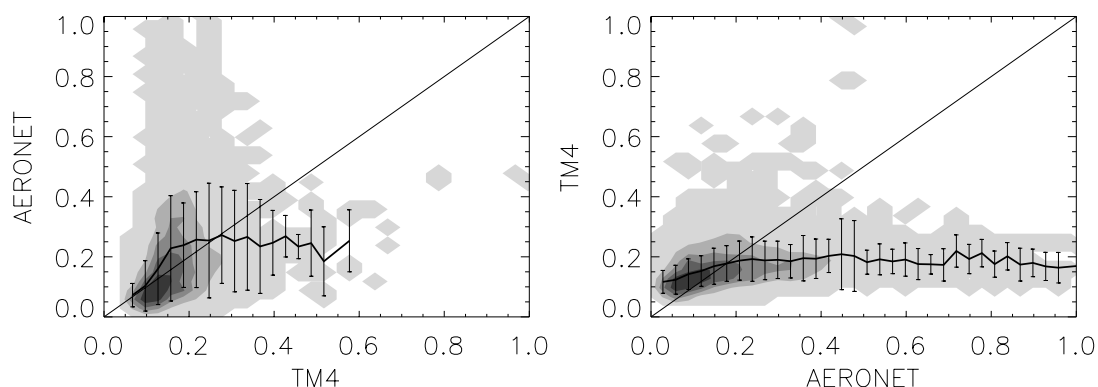


**Figure 5.6** Density plots of simultaneous modeled (TM4) and observed (AERONET) aerosol optical depth. The space is divided in pixels of 0.03 by 0.03 in AOD, the darkest smoothed area contains the pixels with the highest data density and contains 20% of all TM4-AERONET pairs. From dark to light, the other colored areas contain, 40, 60, 80, and 100 % of the data pairs, respectively. (left) The heavy black line indicates the average AERONET AOD for the TM4 AOD specified by the x-axis, the bars indicate the standard deviations of the distribution of AERONET observations around the mean. The thin straight black line indicates perfect agreement. (right) same, but the roles of observations and modeled values have been swapped.

the role of modeled and measured aerosol optical depths interchanged (Figure 5.6, right), more clearly characterizes the reason for the underestimation of the modeled aerosol optical depths. As the average modeled aerosol optical depth is lower than the observed AOD, high observed aerosol optical depths that are not accompanied by modeled high values is decisive for the lower modeled mean AOD.

From Figures 5.6, it might be anticipated that the correlation between observed and modeled aerosol optical depths is not very high. Indeed, the correlation for the individual stations is sometimes acceptable, but mostly weak and sometimes there seems to be no correlation at all (Table 5.7).

**Table 5.5** European AERONET stations selected for the comparison to TM4 model results.

Station	Latitude °N	Latitude °E
Avignon	43.9	4.9
Creteil	48.8	2.4
Gotland	57.9	19.0
Hamburg	53.6	10.0
Helgoland	54.2	7.9
Ispra	45.8	8.6
Lampedusa	35.5	12.6
Lille	50.6	3.1
Modena	44.6	10.9
Moldova	47.0	28.8
Palaiseau	48.7	2.2
Paris	48.9	2.3
Toulouse	43.6	1.4
Venise	45.3	12.5

**Table 5.6** Average modeled (TM4) and measured (AERONET) aerosol optical depth for various temporal selections of the data. The standard deviation of the distribution (square root of the variance),  $\sigma_{\text{dis}}$ , and the number of AOD values that contributed to the calculations  $N$  are also provided. The TM4 data shown only contains the modeled values when AERONET observations are available.

	Period	Mean AOD	$\sigma_{\text{dis}}$	$N$
TM4	2000	0.165	0.065	7505
	March-May-August	0.170	0.058	2726
	March	0.162	0.051	501
	May	0.182	0.070	912
	August	0.163	0.048	1313
AERONET	2000	0.199	0.154	7505
	March-May-August	0.216	0.141	2726
	March	0.211	0.160	501
	May	0.211	0.146	912
	August	0.223	0.128	1313

## 5.4.2 Sensitivity studies

In order to assess which model parameters affect the simulated results most a number of sensitivity studies have been performed.

### 5.4.2.1 Sources

The emission inventories used initially in this study are partly outdated. Effective clean air policies have led to significant reductions of some of the polluting species. For Europe TNO recently updated the most relevant sources of aerosols and their precursor gases. We will use these updated sources to study the effect of emission

**Table 5.7** Correlation between time series of modeled (TM4) and measured (AERONET) aerosol optical depth. MMA stands for March + May + August, Cor. stands for linear Pearson correlation, and  $N$  is the number of comparisons.

Station	YEAR 2000		MMA		March		May		August	
	Cor.	N	Cor.	N	Cor.	N	Cor.	N	Cor.	N
Avignon	0.47	1260	0.46	346	0.40	58	0.30	142	0.60	146
Creteil	0.40	349	0.68	136		0		0	0.68	136
Gotland	0.45	161	0.54	88	0.73	14	0.58	74		0
Hamburg	0.34	282	0.29	81		0		0	0.29	81
Helgoland	0.44	163	0.54	104		0		0	0.54	104
Ispra	0.47	1117	0.42	386	0.64	123	0.53	94	0.04	169
Lampedusa	0.38	546	0.16	205		0		0	0.16	205
Lille	0.31	418	0.24	124	0.65	6	-0.18	27	0.57	91
Modena	0.49	35	0.49	35		0	0.49	35		0
Moldova	0.40	696	0.58	304	0.76	33	0.53	271		0
Palaiseau	0.42	555	0.52	252	-0.07	51	0.58	69	0.63	132
Paris	0.45	23	-1.00	2		0		0	-1.00	2
Toulouse	0.31	253	0.44	93	0.44	93		0		0
Venise	0.20	1647	0.07	570	0.14	123	0.08	200	-0.17	247

source strengths on the aerosol optical depth. To do so, we replaced the old European emissions for the region 34N-66N and 6W-48E by the new TNO emissions. Total mass emissions of the gases SO<sub>2</sub>, NO<sub>2</sub>, NH<sub>3</sub> and the carbonaceous aerosol species BC and OC are 63, 36, 20, 59, and 28 % lower in the TNO inventory than in the previously used inventories. The reduction in emissions, reduce the monthly mean aerosol optical thickness for the whole European domain for March 2000 from 0.21 to 0.16. If TM4 aerosol optical thicknesses are selected with simultaneous AERONET observations the monthly mean aerosol optical thickness reduces from 0.16 to 0.13. This reduction is unwanted as it further increases the discrepancy between TM4 and AERONET aerosol optical depth. However, if we would accept that the updated sources are better, this would mean that the earlier estimates of the aerosol optical thickness is reasonably right for the wrong reason. It is furthermore disturbing that the correlation between the time series of AERONET observations and new modeled aerosol optical depths is worse than for the older emissions. Only for 2 (Venise and Moldova) of the 7 AERONET stations that provide data this month, the correlation is improved, for the others the correlation is deteriorated (Table 5.8).

#### 5.4.2.2 Water vapor redistribution

The relative humidity used in this study directly comes from the ECMWF meteorological fields. The relative humidity in every TM4 grid cell is therefore constant throughout the cell. This is not realistic. Most grid cells contain both cloudy and cloud free fractions. The cloudy part of the grid cell should be saturated. In a sensitivity run we have redistributed the water vapor in our model cells such that the cloudy fraction has a relative humidity of 100%. The remaining water vapor is uniformly distributed over the rest of the grid cell but we tentatively assume that the relative humidity can not drop below 30% by this redistribution. Effectively this water vapor redistribution or relative humidity scaling lowers the relative humidity of the cloud free fraction for which the aerosol optical depth is calculated. This reduction in relative humidity, reduces the monthly mean aerosol optical thickness for the whole European domain for March 2000 from 0.21 to 0.18. We find that the effect of the reduction of relative humidity is especially strong over the oceans. Maxima in aerosol optical depth dominated by sea salt,

**Table 5.8** Correlation between March time series of modeled (TM4) and measured (AERONET) aerosol optical depth for two sensitivity runs. TNO emis. stands for results from a run with updated emission inventory. RH-scaling: results from a run with water vapor redistribution such that cloudy parts have 100% relative humidity. Cor. Stands for linear Pearson correlation,  $N$  is the number of comparisons.

Station	Standard	TNO emis.	RH-scaling	RH-scaling TNO emis	$N$
Avignon	0.40	0.11	0.37	0.07	58
Gotland	0.73	0.57	0.69	0.56	14
Ispra	0.64	0.56	0.63	0.56	123
Lille	0.65	0.63	0.66	0.65	6
Moldova	0.76	0.79	0.82	0.83	33
Palaiseau	-0.07	-0.16	-0.08	-0.15	51
Toulouse	0.44	0.43	0.41	0.36	93
Venise	0.14	0.41	0.16	0.42	123

that are related to strong depression activity, are effectively lowered and are sometimes damped out completely. The largest aerosol optical depths, which are related to extreme water uptake and not necessarily to high aerosol mass loads, are also strongly affected. The reason for this is that the extinction cross section per unit mass increases rapidly with increasing relative humidity. The aerosol optical depth in large fair-weather regions associated with high pressure systems, is not affected much. If TM4 aerosol optical thicknesses are selected with simultaneous AERONET observations the monthly mean aerosol optical thickness is also reduced but the reduction is modest and does not show up in the rounded value that remains 0.16. The correlation between the time series of AERONET observations and modeled aerosol optical depth does not change significantly (Table 5.9).

#### 5.4.2.3 Sources and water vapor redistribution

The combination of water vapor redistribution and updated sources does neither improve the correlation between the AERONET and TM4 series and the underestimate of the average aerosol optical depth that was found for the individual sensitivity runs remains. The absolute differences between the standard run and the run with the TNO sources and redistributed water vapor, is shown in the left panels of Figure 5.7. The spatial distribution of the differences resembles that of the averaged aerosol optical depth for all four selected periods as shown in Figure 5.3. In the right panels of Figure 5.7 the ratio of the standard run to the run with the TNO sources and redistributed water vapor is shown. The highest values are more or less co-located with the maxima in aerosol optical depth for all periods. The maximum over Western Europe can best be explained by the large differences between the two emission inventories. For the Russian maximum in the winter period (including March) water vapor redistribution is very important. The shallow heavily aerosol loaded boundary layer becomes very humid by times, fog and low level clouds then easily form, so that the water vapor redistribution becomes very important. Overall, the ratio of the

**Table 5.9** Correlation between time series of modeled (TM4) and measured (AERONET) aerosol optical depth. “Stand” is the standard run, “Sens” is the sensitivity run with other sources and water vapor redistribution, “MMA” stands for March + May + August.

Station	YEAR 2000		MMA		March		May		August	
	Stand	Sens	Stand	Sens	Stand	Sens	Stand	Sens	Stand	Sens
Avignon	0.47	0.53	0.46	0.37	0.40	0.07	0.30	0.28	0.60	0.58
Creteil	0.40	0.35	0.68	0.64					0.68	0.64
Gotland	0.45	0.32	0.54	0.00	0.73	0.56	0.58	0.12		
Hamburg	0.34	0.35	0.29	0.34					0.29	0.34
Helgoland	0.44	0.50	0.54	0.50					0.54	0.50
Ispra	0.47	0.48	0.42	0.44	0.64	0.56	0.53	0.56	0.04	0.12
Lampedusa	0.38	0.49	0.16	0.54					0.16	0.54
Lille	0.31	0.27	0.24	0.23	0.65	0.65	-0.18	-0.18	0.57	0.47
Modena	0.49	0.47	0.49	0.47			0.49	0.47		
Moldova	0.40	0.53	0.58	0.63	0.76	0.84	0.53	0.56		
Palaiseau	0.42	0.39	0.52	0.45	-0.07	-0.15	0.58	0.47	0.63	0.62
Paris	0.45	0.43	-1.00	-1.00					-1.00	-1.0
Toulouse	0.31	0.21	0.44	0.36	0.44	0.36				
Venise	0.20	0.36	0.07	0.27	0.14	0.43	0.08	0.22	-0.17	0.05

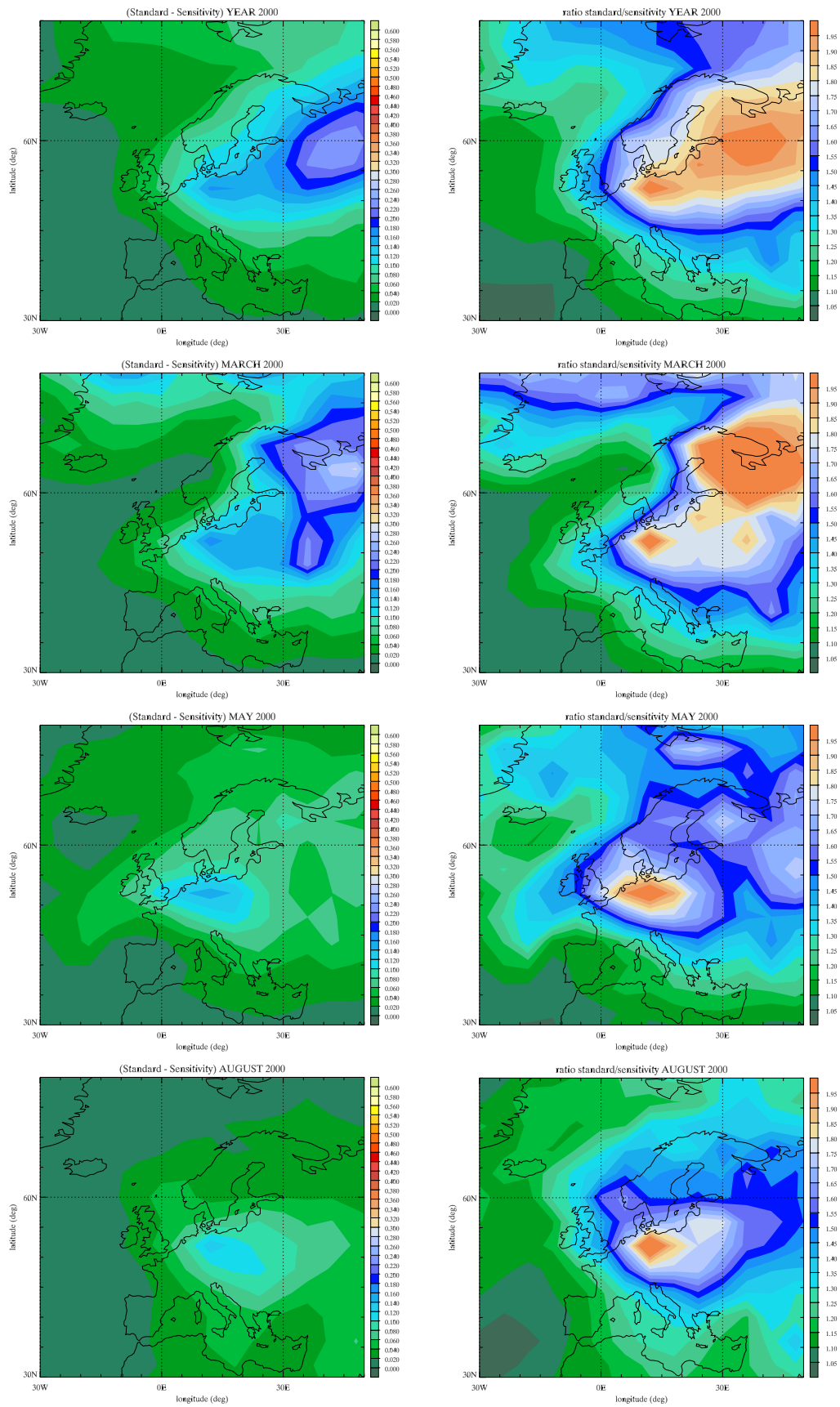


**Figure 5.7** Left panels: absolute differences between the AOD from the standard run and the run with TNO-sources and water vapor redistribution, for four different selected periods. Right panels: corresponding ratios of the AODs from the standard run to those from the run with TNO-sources and water vapor redistribution.

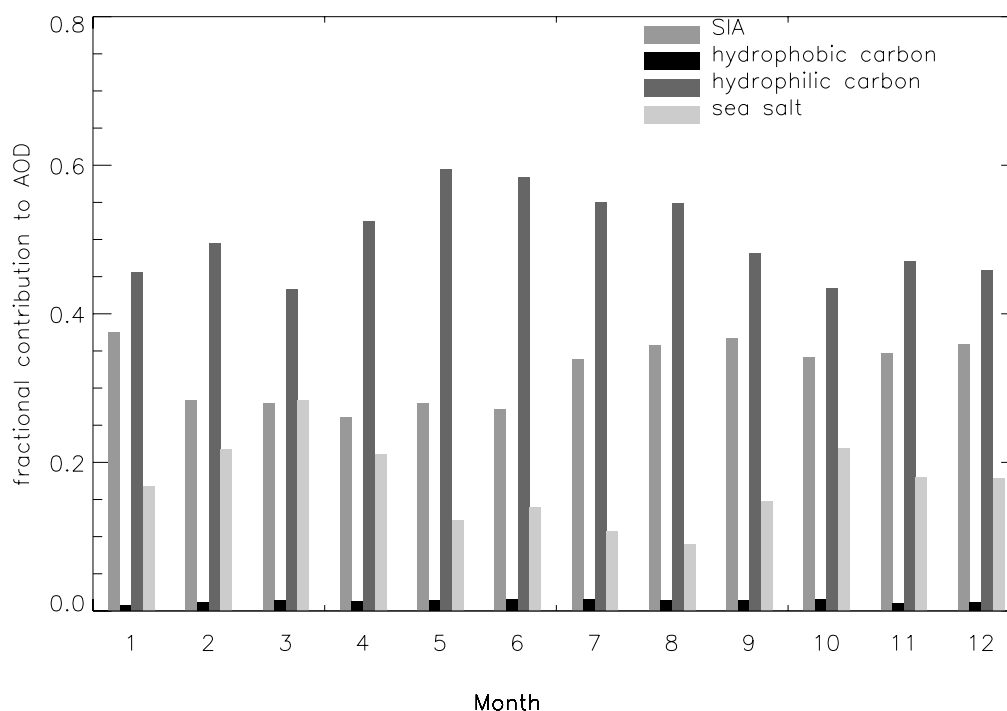


**Figure 5.8** Yearly variation of the fractional contribution of the various aerosol species to the total aerosol optical depth for the sensitivity run with the new TNO emission inventory and redistributed water vapor.

Standard run to the sensitivity run is somewhat larger over central Europe than expected from the water vapor rescaling and total reduction of aerosols and their precursors. A possible explanation for this may be that pure secondary inorganic aerosols contribute a lesser fraction of the total aerosol optical depth in the sensitivity run than in the standard run (Figures 5.8 and 5.9). Pure secondary inorganic aerosols take up water more easily than secondary inorganic aerosols that are internally mixed with carbonaceous aerosols. This means that even for fixed aerosol load, a reduction in the ratio secondary inorganic aerosol to hydrophilic carbons would lead to lower aerosol optical depths. Last remark, because of the reduced emissions, sea salt aerosol becomes a more important contributor to the total aerosol optical depth throughout the year.

## 5.5 Discussion and conclusions

The simulated mean aerosol optical thickness is lower than the observed mean aerosol optical depth. A possible reason for this is probably that the high spatial variability of water vapor is not resolved in our model. The relation between aerosol mass and aerosol optical depth is strongly non-linear with respect to water vapor. For perfectly simulated aerosol mass concentrations, the homogeneous distribution of water vapor throughout grid cells thus leads to systematic under prediction of aerosol optical depths. This effect becomes increasingly important for increasing relative humidity. Another possible reason for underestimating mean aerosol optical depth in the model, is the way evaporation is treated. Precipitation formed in the clouds is scaled down to the precipitation that eventually reaches the surface. Implicitly this means that



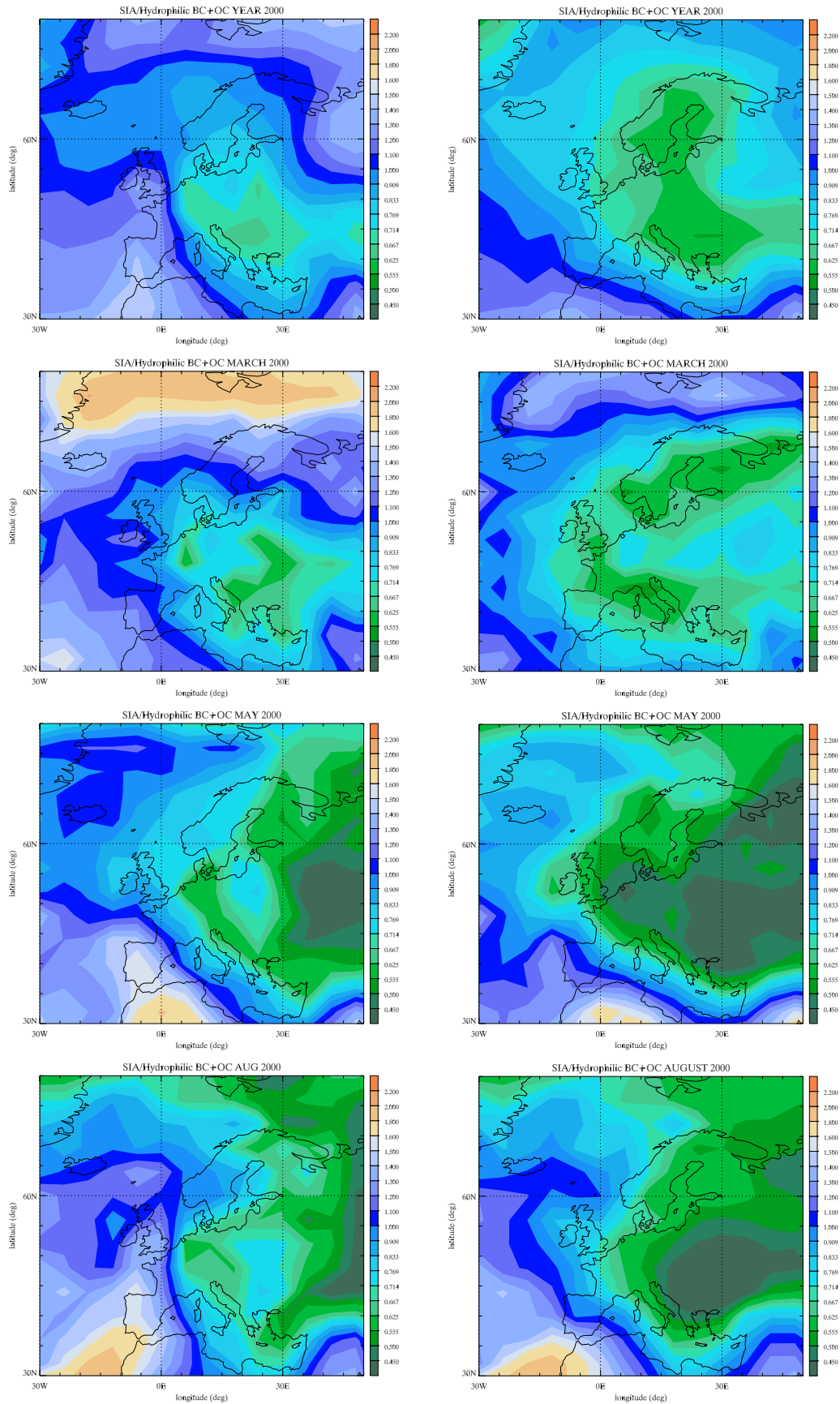


**Figure 5.9** Ratio of secondary inorganic aerosol (SIA) and internal mixture of carbonaceous aerosol and secondary inorganic aerosol (hydrophilic BC+OC) for four different selected periods. Left panels show the standard run, and right panels the run with new TNO-sources and water vapor redistribution.

aerosols are released by evaporation in the cloudy environment, where they remain prone to effective removal by in-cloud scavenging. In the real atmosphere much of the evaporation is below the clouds, where the much less effective below-cloud scavenging is responsible for the removal of aerosols. The variance of the simulated aerosol optical depths is smaller than the variance of the observed aerosol optical depths by AERONET. We suggest that also the coarseness of the model grid may contribute to the underestimation. Averaging of aerosol mass concentrations over large areas levels off the extreme values. Areas with fair weather, which are related to maxima in aerosol optical depth, very often do not cover an entire grid cell. At the boundaries of the grid cells wet deposition then reduces the aerosol mass of the entire grid cell due to mixing. The same holds for aerosol poor areas that always contain fair weather spells.



# 6

## **Perspectives on the assimilation of aerosol optical depth – development of an aerosol assimilation system for TM4 and application to Europe**

### **6.1 Introduction**

In Chapter 5 a module for the prediction of aerosol optical depth was developed. Application of the model over Europe revealed that the model does not always simulate the aerosol optical depth realistically compared to ground based observations. In this chapter, we describe the development of an assimilation system that adjusts simulated aerosol concentration fields aiming to improve the agreement between the simulated aerosol optical depths and other measures of aerosol optical depth. The assimilated quantities are aerosol optical depths retrieved from satellite observed radiances from ATSR-2. Particular attention has been given to the modeling of the observational and model errors. The system is applied over Europe and the results are compared to independent ground based observations.

### **6.2 Transport model TM4 aerosol module**

For the aerosol modeling we use version 4 of the three-dimensional global chemistry transport model TM (Heimann, 1995; Dentener et al., 1999). The aerosol module for simulating aerosols is described in detail in Chapter 5 of this thesis. Here, we use the model version that does not contain water vapor rescaling and we use the original emission inventory (standard run). This version gave results that are closest to AERONET observations.

### **6.3 Assimilation System**

The assimilation scheme that was implemented is based on the Kalman filter equations (Kalman and Bucy, 1961) and has previously been applied to ozone in TM3 (Jeuken et al., 1999; Eskes et al., 2003). The scheme adjusts modeled column aerosol fields to match observed quantities in a manner consistent with uncertainties in the model and retrieval. In our application the ‘observations’ are column-integrated aerosol optical depths retrieved from satellite-observed radiances denoted  $\tau^o$ . Running the model produces forecasts of the three dimensional aerosol optical depth fields

denoted by  $\tau^f$ . The core of the assimilation scheme is the analysis of the aerosol optical depth field given by:

$$\tau_k^a = \tau_k^f + \mathbf{P}\mathbf{H}^T(\mathbf{H}\mathbf{P}\mathbf{H}^T + \mathbf{R})^{-1}(\tau^o - \mathbf{H}\tau_k^f) \quad , \quad (6.1)$$

where  $k$  is an index for the vertical layer,  $\mathbf{H}$  is the observation operator;  $\mathbf{R}$  is the observation error covariance matrix,  $\mathbf{P}$  is the forecast error covariance matrix, and the superscript T denotes the transpose of the matrix. To reduce computation time, high-resolution optical depth retrievals are averaged to the TM grid. This avoids the spatial interpolation of model values to the location of the individual satellite pixels online, and the observation operator  $\mathbf{H}$ , that projects model space to observation space, simply represents the summation over the vertical layers. The error covariance matrices determine the relative weighting of the model forecast and the observations. A large forecast error ( $\mathbf{P}$ ) and relatively small error in the observation ( $\mathbf{R}$ ) will result in strong adjustment towards the observation. Vice versa, highly uncertain observational data, but trustworthy modeled fields, will result in a small impact of the observations on the analyses. For the observations we define a diagonal error covariance matrix  $\mathbf{R}$ , implying that the observational errors are uncorrelated between adjacent grid cells. This is reasonable in view of the short spatial scale at which AOD varies. The diagonal elements are the observation errors in the averaged observations (super-observations), which are estimated in section 6.3.1. The forecast error covariance matrix  $\mathbf{P}$ , which is kept constant in time, is prescribed as in Eskes et al. (2003):

$$P_{ij} = \sigma_i^\tau \sigma_j^\tau f_{\text{hor}} \quad , \quad (6.2)$$

where indices  $i$  and  $j$  represent two different model grid cells,  $\sigma_i^\tau$  is the forecast error variance in the total optical depth, which is estimated in section 6.3.2. The horizontal forecast error correlation is represented by the function  $f_{\text{hor}}$  derived by Thiebaut (1976) based on the assumption that the errors can be represented as a second-order regressive process:

$$f_{\text{hor}}(d_{ij}) = \left(1 + \frac{d_{ij}}{l_x}\right) \exp\left(-\frac{d_{ij}}{l_x}\right) \quad , \quad (6.3)$$

with  $d_{ij}$  the horizontal distance between two model grids, and  $l_x$  the horizontal correlation length-scale for errors in the model fields. In the current version of the assimilation module  $l_x$  is set to 200 km.

Finally, when equation (6.1) is solved and an optimal distribution of  $\tau_k^a$  is obtained, the mass of each aerosol tracer is adjusted accordingly. As we do not have additional information as to which aerosol species is responsible for the mismatch between observed and modeled aerosol optical depth, we choose to adjust each aerosol type  $s$  proportional to its mass  $M$  in grid cell  $k$ , as was also done by Collins et al. (2001):

$$M_{sk}^a = M_{sk}^f \frac{\tau_k^a}{\tau_k^f} \quad (6.4)$$

### 6.3.1 Satellite observation error

The field assimilated into the model is the aerosol optical depth at 550 nm, which was retrieved by TNO-D&V from radiances measured at top-of-atmosphere (TOA) by the Along Track Scanning Radiometer 2 (ATSR-2). For the retrieval the dual view algorithm of Veeffkind et al. (1998) was used over land and the single view algorithm of Veeffkind and De Leeuw (1998) over water. For the selection of cloud-free observations, the cloud screening scheme of Robles González (2003) based on the work of Koelemeijer et al. (2001) was applied. In both retrieval algorithms the contributions of Rayleigh scattering, gaseous absorption (ozone), and surface reflectance to the measured TOA reflectance were removed to isolate the aerosol signal. The relative contribution of different aerosol types that best reproduce the remaining spectral TOA reflectance was then determined. The aerosol types that were included for the retrieval over Europe were “marine aerosol” with an effective radius of  $1\ \mu\text{m}$  (Shettle and Fenn, 1979) and anthropogenic aerosol consisting mainly of sulfate and nitrate with an effective radius of  $0.05\ \mu\text{m}$  (Volz, 1972). Assuming that the TOA reflectance due to an external mixture of two different aerosol types can be approximated as the weighted average of the reflectance of the individual aerosol types and that the TOA reflectance is a linear function of the aerosol optical depth, the aerosol optical depth could then straightforwardly be computed.

The error in ATSR-2 retrievals made by TNO-D&V in the above described way is estimated by comparison to independent aerosol optical depth observations that are made available by AERONET (AERosol RObotic NETwork; Holben et al., 1998). For this purpose the AERONET aerosol optical depth at 550 nm is estimated from the aerosol optical depth at measured wavelengths (440, 670, 870 and 1020 nm) using the provided Ångström exponent that is valid for the closest two enveloping wavelengths. For the year 2000, all simultaneous ATSR-2 retrievals and AERONET observations of aerosol optical depth are mutually compared for the months March, May, and August. To increase the number of simultaneous observations, we include the mean aerosol optical depth of all individual ATSR-2 retrievals made within an area of  $0.1^\circ \times 0.1^\circ$  surrounding each AERONET site and we average the AERONET aerosol optical depth from half an hour before to half an hour after the satellite overpass. Doing so, we obtain (only) 46 simultaneous observations in the selected period. The average aerosol optical depth for this data set is 0.21 both for the AERONET and ATSR-2 retrieval. Comparing the simultaneous observations and retrievals one-by-one we find for the variance of the distribution of the differences 0.025 ( $\sigma = 0.16$ ). Since the accuracy of the AERONET measurements is estimated to lie between  $\sigma = 0.01$  and  $\sigma = 0.015$  (Eck et al., 1999), we conclude that the deduced variance is largely due to uncertainties in the retrieval.

The aerosol optical depth used in the assimilation scheme as (super-) observation is the average of all high-resolution aerosol optical depth retrievals that are within in a certain model cell of  $4^\circ \times 6^\circ$ . Considering the large number of high-resolution observations that contribute to each such super-observation, these super-observations are in general much more accurate than the individual retrievals, as the standard deviation of uncorrelated observations scales with the inverse of the square root of the number of observations. However, because the individual retrievals are not independent, we conservatively estimate that the accuracy equals the uncertainty in a

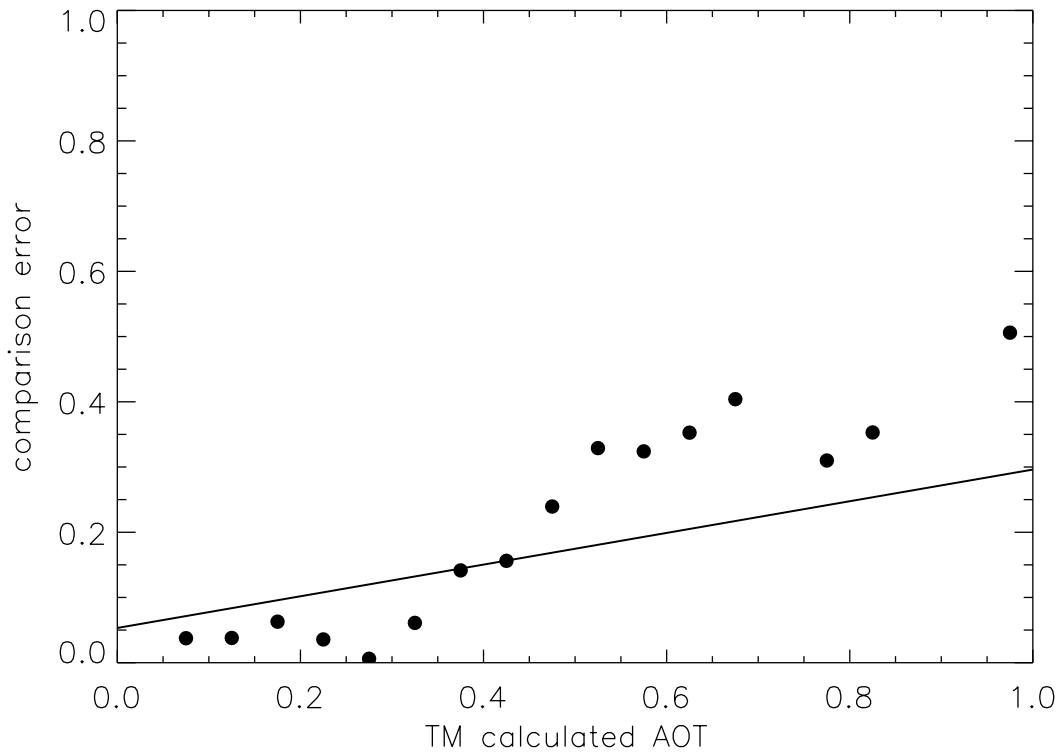


**Figure 6.1** Mean difference between observed (AERONET) and simulated (TM4) aerosol optical depth as a function of the magnitude of the aerosol optical depths (filled circles). The straight line is a weighted linear fit through the data (see text).

single high-resolution observation as obtained from comparison to AERONET optical depth observations,  $\sigma_{\text{super-observation}} = 0.16$ . This implies that we assume errors in the retrievals to be completely correlated within the area of a super-observation and that the error correlation reduces to zero when moving out of the area (remember,  $\mathbf{R}$  is diagonal).

### 6.3.2 Model error

We estimate the uncertainty in the modeled aerosol optical depth,  $\sigma_{\text{model}}$ , from comparison to AERONET aerosol optical depth observations. The differences between the modeled and measured aerosol optical depths are caused by model and measurement errors and the by fact that the AERONET point observations are not representative for the coarse model cells. This latter representation problem also occurs when ATSR-2 super-observations are compared to point observations. A convenient way to estimate the representation error is to consider the variance of the individual ATSR-2 pixels ( $1 \times 1 \text{ km}^2$ ) that contribute to each of the average AOD super-observations. Doing so for the 445 super-observations, which were on average compiled of about 2000 pixels, the variance is 0.016 ( $\sigma = 0.13$ ) independent of the aerosol optical depth. We use this value to estimate the representation error for the comparison of model data to AERONET,  $\sigma_{\text{repre}}$ . To compare modeled and AERONET aerosol optical depths, we calculate the difference of all simultaneous values. Grouping all differences in bins with sizes of 0.05 in simulated aerosol optical depth,

**Table 6.1** Mean aerosol optical depth, standard deviation of the distribution ( $\sigma_{\text{distr.}}$ ) and number of data points selected (N) for various selection criteria (ATSR means if only if ATSR observations are available) for the months March, May, and August.

	Assimilation	Selection criterion	Mean AOD	$\sigma_{\text{distr.}}$	N
AERONET		All data	0.22	0.14	2726
		ATSR-2	0.22	0.14	109
ATSR-2		All data	0.22	0.09	445
		AERONET	0.21	0.09	109
TM4	NO	All data	0.19	0.12	31206
	NO	AERONET	0.17	0.06	2726
	NO	ATSR-2	0.18	0.09	445
	NO	both	0.17	0.06	109
TM4	YES	All data	0.21	0.12	31206
	YES	AERONET	0.18	0.06	2726
	YES	ATSR-2	0.21	0.08	445
	YES	both	0.19	0.06	109

we calculate the distribution of the mean model-measurement differences as a function of aerosol optical depth. From a weighted linear fit through the distribution of mean differences, we then obtain an error estimate that we denote by  $\sigma_{\text{compare}}$  (Figure 6.1). If we further assume that the error in AERONET aerosol optical depths is negligibly small as compared to the model and representation errors, we can write:

$$\sigma_{\text{compare}}^2 = \sigma_{\text{model}}^2 + \sigma_{\text{repre}}^2 \quad (6.5)$$

Using equation (6.5), we find negative values of  $\sigma_{\text{model}}^2$  for aerosol optical depths up to about 0.35. This means that the model-measurement differences can be explained by representation failure for small optical depths. As it is quite unlikely that the model is perfect for low aerosol optical depths, we conservatively estimate the model error to be the maximum of  $\sigma_{\text{repre}}$  and  $\sigma_{\text{compare}}$ , so that:

$$\sigma_{\text{model}} = \max(0.13; 0.05 + 0.3 \times \text{AOD}) \quad (6.6)$$

## 6.4 Application of the system

The model is run for the whole year 2000, whereas application of the assimilation system is restricted to three months, i.e. March, May, and August. The selection of these periods is based on the relatively large amount of cloud free days in these months that resulted in less cloud-contamination of the satellite observations and thus to the availability of more observations for assimilation.



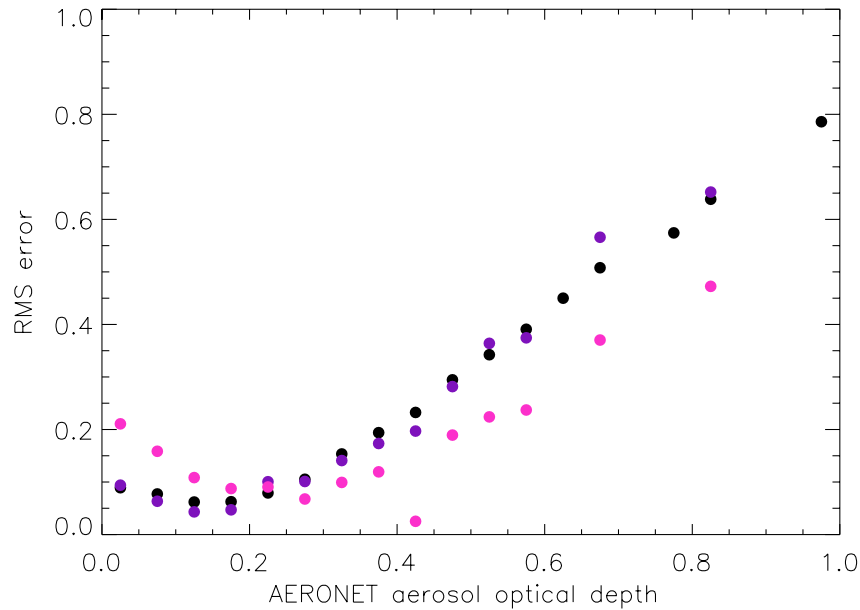


**Figure 6.2** RMS error of the aerosol optical depth for the ATSR-2 observations (light grey), for all simulated fields (black) and for simulated fields selected when ATSR-2 observations are available (dark grey)

### 6.4.1 Satellite observations

The mean aerosol optical depths of the ATSR-2 super-observations compare very well AERONET to independent ground based observations that are made available by (Aerosol RObotic NETwork, Holben et al., 1998). For a description of the AERONET data the reader is referred to Chapter 5. For the months March, May, and August the mean optical depth values are listed in Table 6.1. The mean ATSR-2 values compare in particular better to the AERONET observations than the model simulated mean aerosol optical depths. Due to the compilation of super-observations the extremes are leveled off so that the variance in the distribution of the super-observations is somewhat smaller than that of the AERONET data set, which is not the case for the original  $0.1^\circ \times 0.1^\circ$  ATSR-2 data set. For the direct comparison of ATSR-2 and AERONET observations, we calculate the root-mean-square of the residuals as a function of aerosol optical depth:

$$RMS = \sqrt{\left( \frac{\sum_i (ATSR(i) - AERONET(i))^2}{N} \right)}, \quad (6.7)$$

where  $i$  is an index for a simultaneous satellite and AERONET aerosol optical depth observation. This RMS error is larger than the RMS error of the simulated aerosol optical depths for low aerosol optical depths (Figure 6.2). For higher aerosol optical depths the ATSR-2 observations compare more favorably to the AERONET observation than the simulated results. This finding corresponds with the error estimates of observed and simulated aerosol optical depths given in sections 6.3.1 and 6.3.2, respectively. Based on these findings, we expect the simulated aerosol fields to benefit from assimilation of the ATSR-2 observations.

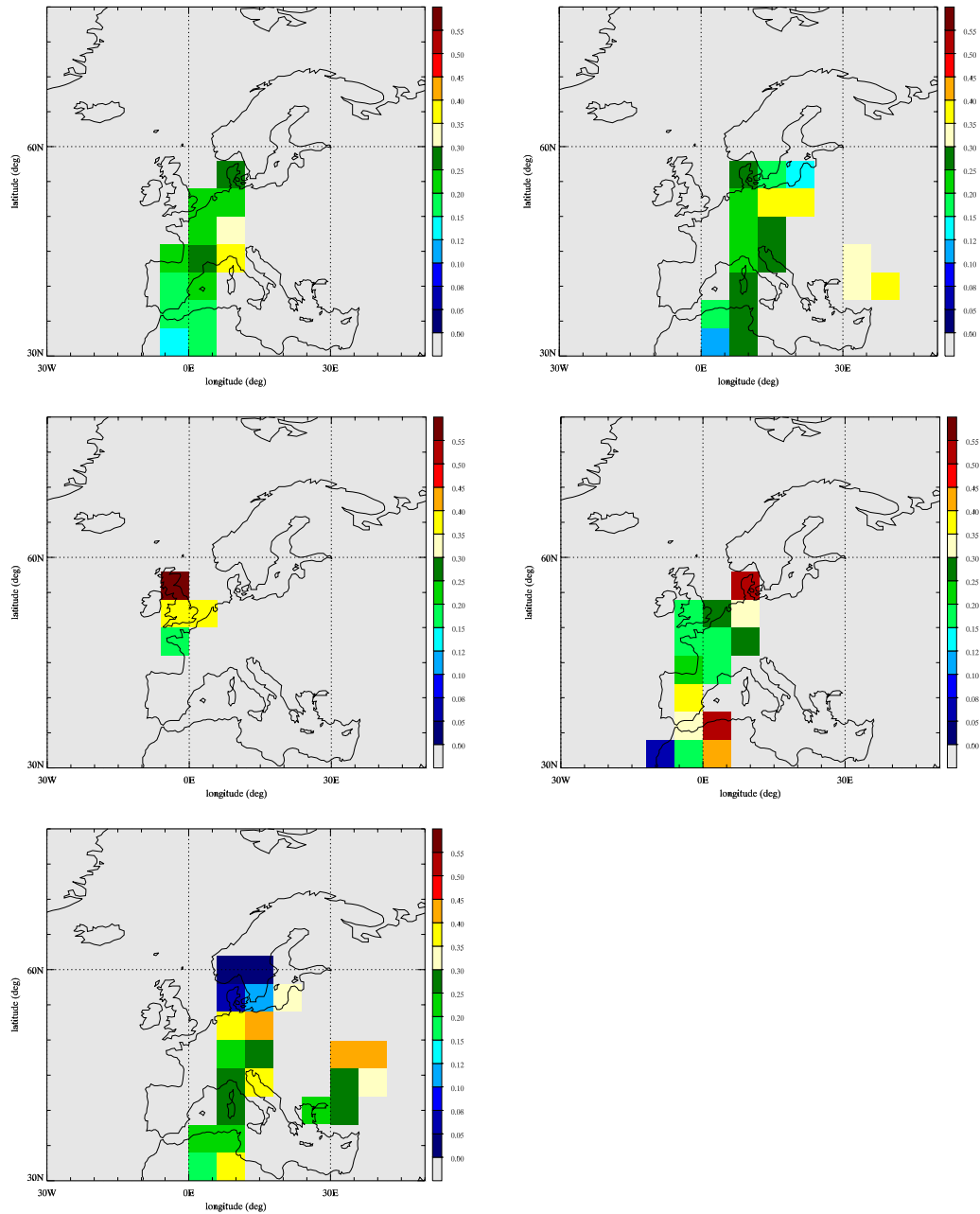


**Figure 6.3** ATSR super-observations for (top left) 20 March 2000 9 UT (top right) 20 March 2000 12 UT (middle left) 22 March 2000 9 UT (middle right) 23 March 2000 9 UT (bottom left) 23 March 2000 12 UT

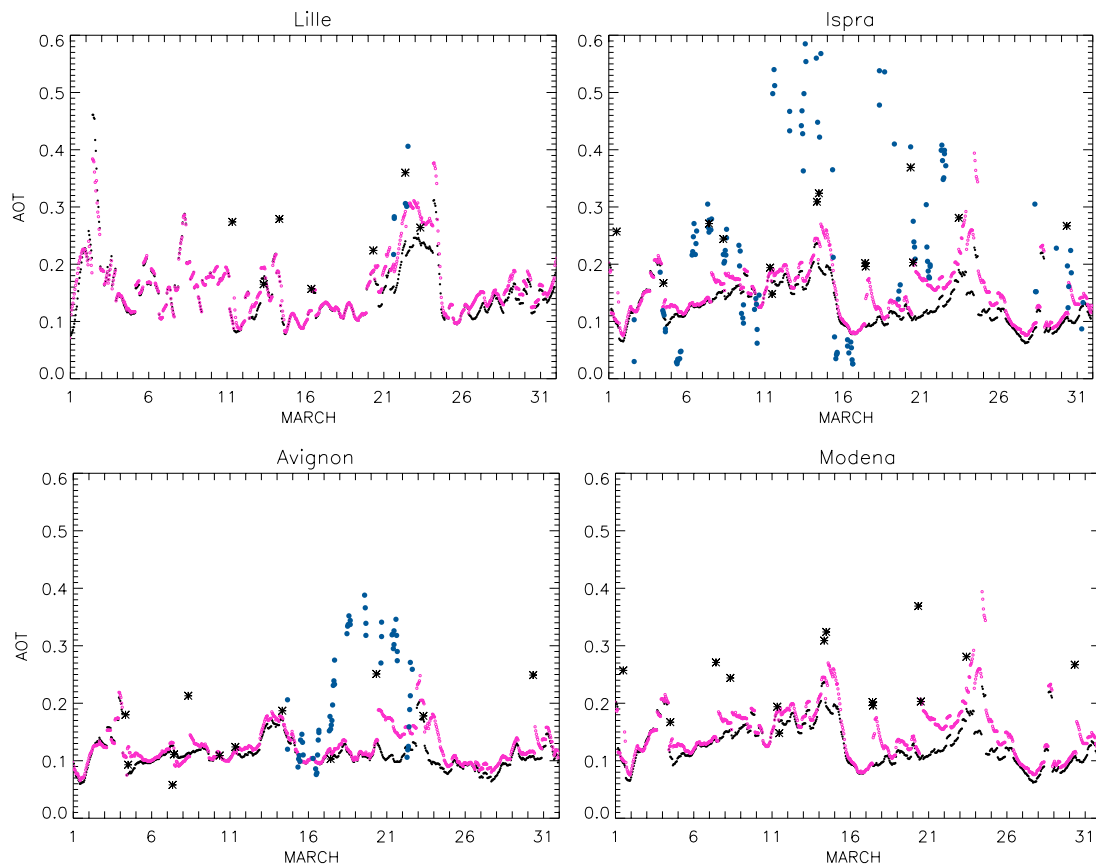


**Figure 6.4** Aerosol optical depth for March 2000 for Lille, Ispra, Avignon and Modena. Simulations without assimilation (black), simulations with assimilation (pink), coincident ATSR-2 observations (black asterisks), and AERONET observations (blue circles)

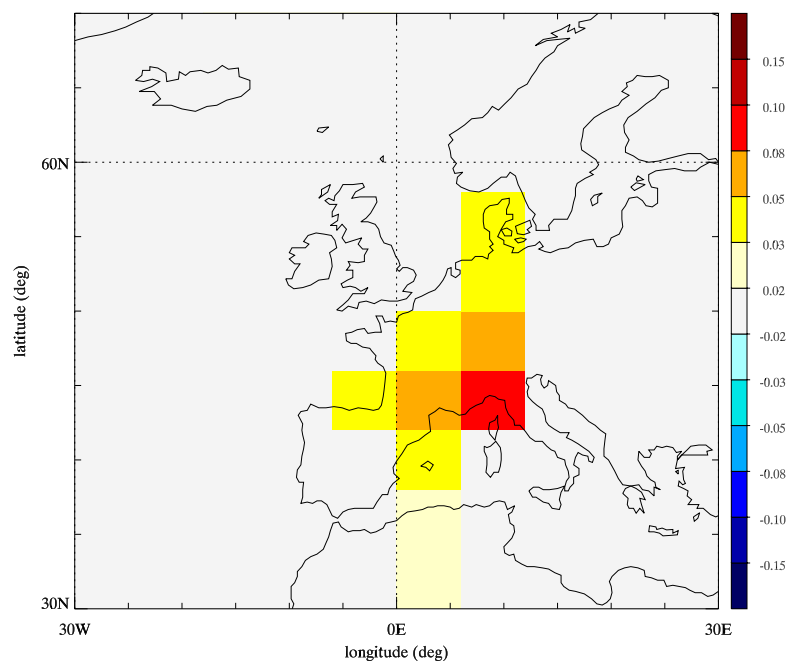


**Figure 6.5** Difference between the simulated aerosol optical depths just before and just after the assimilation of the ATSR-2 super-observations of 20 March 9UT.

## 6.4.2 Results and discussion

To assess the impact of the assimilation, we first consider two case studies.

### 6.4.2.1 Case 1: March 2000

During the second half of March 2000 a high pressure system dominated the weather in West-Central Europe. The lack of aerosol removal by wet deposition enabled the build-up of considerable atmospheric aerosol loading. The cloud free conditions also allowed relatively successful retrieval of aerosol optical depths from the ATSR-2 measurements. The compiled super-observations for the selected period are shown in Figures 6.3. The time series of the AERONET stations Lille and Avignon (Figure 6.4, left panels) clearly show that the simulated aerosol optical depths benefit from the assimilation. For Lille the AERONET observed aerosol optical depth increase is captured by the model and the assimilation increases the simulated aerosol optical depth towards the AERONET observations. For the station Avignon the build-up of aerosols is not simulated, due to sinks in the grid cell that effectively balance the emissions. The assimilation again pulls the simulated aerosol optical depths towards the AERONET observations. It is clearly seen that the simulated aerosol optical depths benefit from the adjustment for several days. In Figure 6.5, the difference in aerosol optical depth just before and just after the assimilation of the ATSR-2 super-observations is shown for 20 March 9 UT. The particularly strong update in the area south of the Alps is also visible in the time series of Ispra and Modena (Figure 6.4, right panels). The assimilation improves the correlation between the AERONET observations and the simulation for Avignon from 0.39 to 0.42 and for Lille from 0.65 to 0.73 for the month of March. However, for Ispra the correlation reduces from 0.64 to 0.57. For Modena, AERONET observations were not available this month.

### 6.4.2.2 Case 2: May 2000

In the middle of May 2000, a frontal zone approached Central Europe from the west. In front of the frontal zone high aerosol optical depths are measured by ATSR-2 (Figure 6.6). However, the strong impact of assimilation of this high AOD does not last long (Figure 6.7). The frontal zone effectively removed the aerosol particles from the atmosphere within a few days (Figures 6.8). The time evolution of simulated aerosol optical depths cannot be compared against AERONET observations. Due to the sparse sunny spells, the fractions of the grid cells covered by clouds are higher than 0.9 for 16 and 17 May, AERONET does not provide an estimate of the aerosol optical depth. The correlation between the available AERONET observations and simulated aerosol optical depths for the month of May is close to zero and even slightly negative for Lille. Assimilation does not improve this correlation.

### 6.4.2.3 General results

The assimilation of ATSR-2 observations increases the mean aerosol optical depth, so that it approaches the mean optical depth observed by AERONET (Table 6.1). The standard deviations of the distributions are only marginally changed. The correlation (linear Pearson) between AERONET observations and simulated aerosol optical depths does not change either and remains 0.30. For the various stations, we find either better or worse correlation coefficients and we do not find regions that particularly benefit from the assimilation. It seems that the assimilation of ATSR-2 data merely acts as a source of aerosol optical depth and thus of aerosol mass rather than improving the spatial and temporal distribution.

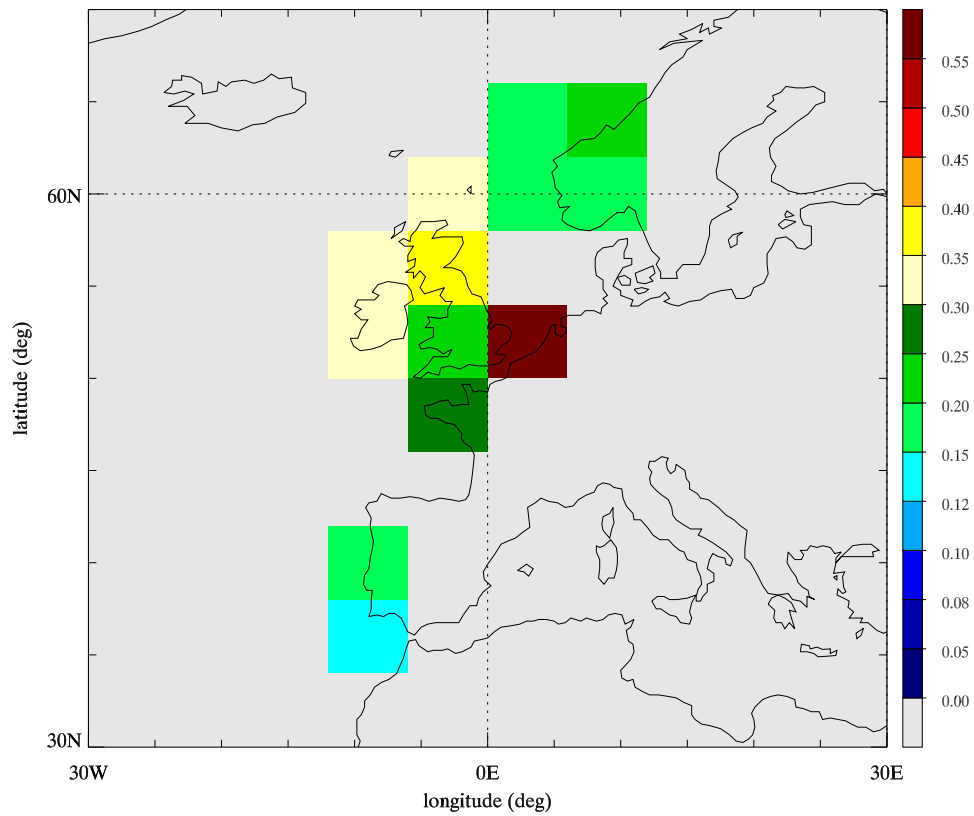


Figure 6.6 ATSR-2 super-observations for 15 May 2000, 9UT.

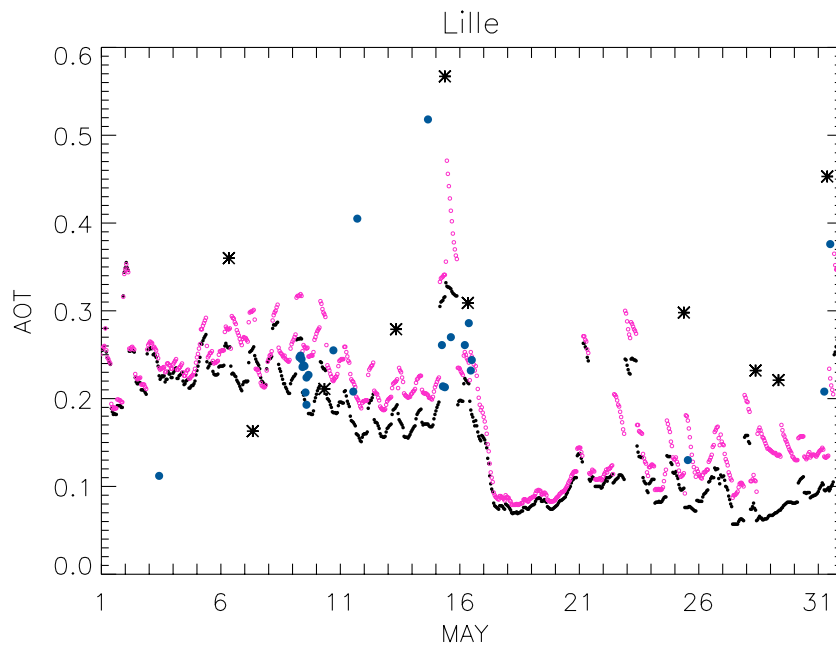
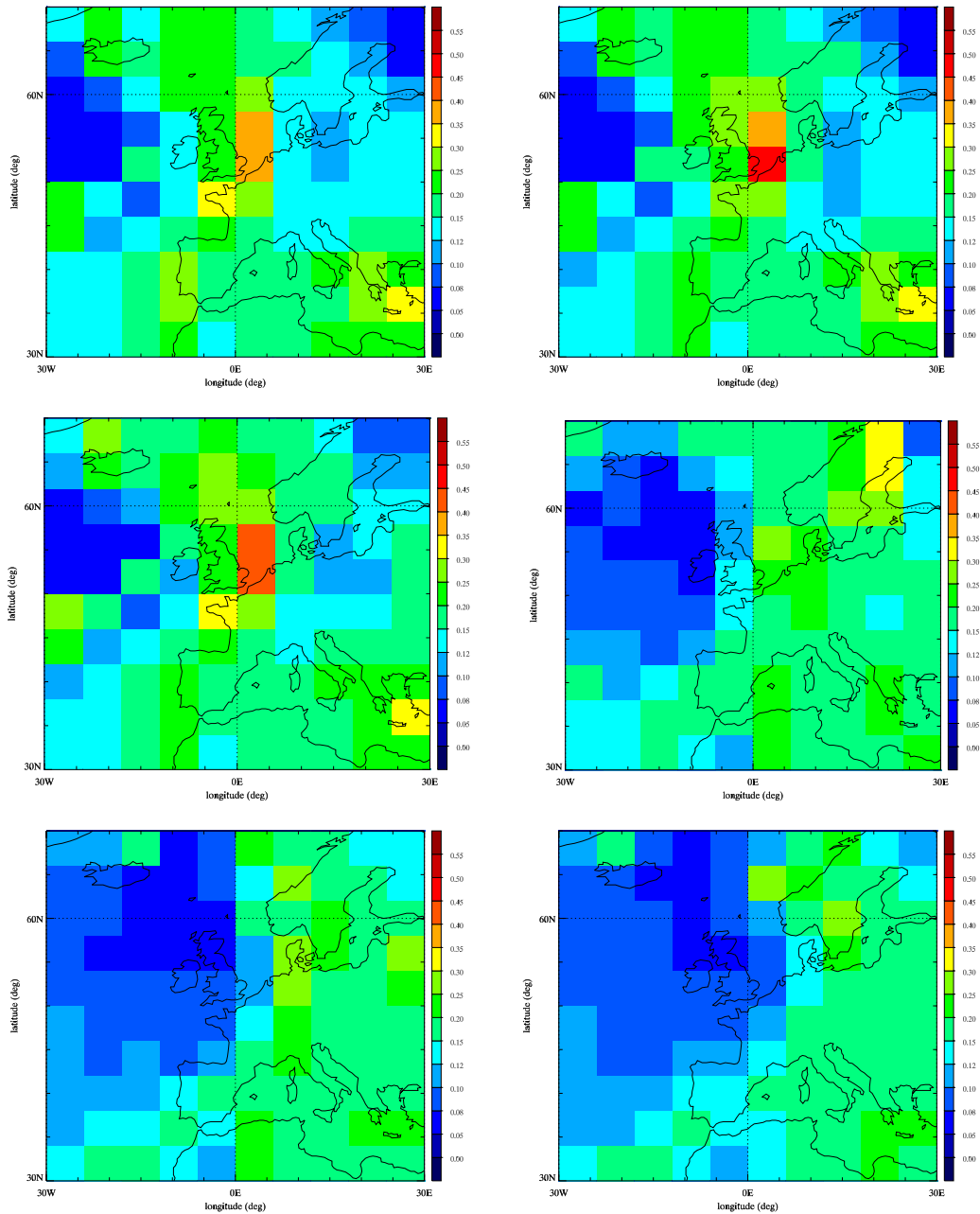


Figure 6.7 Aerosol optical depth for March 2000 for Lille. Simulations without assimilation (black), simulations with assimilation (pink), coincident ATSR-2 observations (black asterisks), and AERONET observations (blue circles)



**Figure 6.8** Aerosol optical depth over Europe (left top) 15 March 2000, 9UT before assimilation (right top) 15 March 2000, 9UT after assimilation (left middle) 15 March 2000, 15UT (right middle) 16 May 15 UT (left bottom) 17 May 9 UT (right bottom) 17 May 15 UT.

## 6.5 Discussion and conclusions

An operational system for the assimilation of aerosol optical depth is developed and applied to Europe using ATSR-2 observations. On average, the assimilation acts as a source of aerosol mass and aerosol optical depth. This results in a better agreement between the mean simulated (TM4) and observed (AERONET) aerosol optical depths. The temporal correlation, on the other hand, does not benefit from the assimilation. A possible reason for this may be that the assimilation of aerosol optical depth is not the best way to improve simulated aerosol concentrations, and thus aerosol optical depth. The variability of aerosol optical depth is to a large extent caused by the spatial and temporal variability of water vapor. Uncertainties in the water vapor fields may therefore lead to large uncertainties in the simulated aerosol optical depth. A discrepancy between the simulated and assimilated aerosol optical depth, then leads to an adjustment of the aerosol concentration fields. If the simulated aerosol optical depths deviate from their true values because of relative humidity errors instead of wrongly simulated aerosol concentration fields, this adjustment is erroneous. The improvement of the model caused by the assimilation is also limited because of the poor quality of the ATSR-2 data. The correlation between all simultaneous AERONET observed and ATSR-2 retrieved aerosol optical depth is negligible (0.03). The reason for this weak correlation is not the compilation of super-observations. The correlation of the original  $0.1^\circ \times 0.1^\circ$  data set is also very weak (0.13). We believe that aerosol simulations can benefit from the assimilation of aerosol optical thickness when more accurate observations become available in the future.

# Summary and conclusions

## Chapter 1

In chapter 1, a brief overview on observed and projected climate changes was given to underline the relevance of this thesis.

## Chapter 2

In chapter 2, the question how aerosols impact on temperature and precipitation is discussed. For temperature this is done using the concept of radiative forcing. We discuss the shortcomings of this concept when applied to aerosols. The essential of the radiative forcing concept is that comparison of forcings caused by different agents directly provides the relative importance of the forcing agents considered. For scattering aerosols, such as sulfate, climate sensitivities similar to those for greenhouse gases are found, so that the concept of radiative forcing is useful. When studying the first indirect aerosol effects, many of the forcing estimates given in the literature include some dynamical and water vapor feedbacks, and the estimates can therefore not be considered radiative forcings. Estimates of the second aerosol indirect effect include feedbacks to the liquid-water path and cloud amount by definition. Radiative forcing of the second indirect effect is therefore an erroneous concept. If the earth-troposphere system is in a state of radiative-convective equilibrium, the conclusion is that the direct effect of absorbing aerosols on the global yearly-mean temperature is small. However, absorbing aerosols change the surface-atmosphere coupling significantly so that the lapse rate is perturbed. We conclude that for absorbing aerosols the traditional radiative forcing is an erroneous metric for the impact of aerosol forcing on the surface temperature as well. The additional climate feedback of absorbing aerosol on the lapse rate has important implications due to subsequent changes in clouds, the so called semi-direct aerosol effect. Based on process studies provided in literature, we conclude that the semi-direct effect is an underexposed subject and that the current widely accepted assumption that the semi-direct effect is always positive may not be true. Because of the potentially small radiative forcing of absorbing aerosol and its semi-direct effect on clouds, we argue that the basic condition that climate response has to have a fixed proportionality to the aerosol radiative forcing comparable to other forcings, is violated. Discussion of alternative concepts of forcings, led to the conclusion that no alternative is as good that it can fully replace the current radiative forcing definition. The overall conclusion is that some aerosol-impacts on climate are not well captured by the current definition of radiative forcing and that an alternative is not readily available.



The traditional radiative forcing concept is inappropriate to predict the magnitude or even the sign of the global mean precipitation changes that are caused by aerosols. In a warmer climate the atmosphere will most likely contain more water vapor. As there is no compelling evidence of systematic changes in the dimensions and frequency of occurrence of precipitating systems, moisture increases will likely lead to more intense precipitation. Moreover, additional latent heat release may further invigorate the most intense precipitating systems. Based on theoretical considerations and supporting evidence from several case studies, we expect that the overall effect of aerosols is to efficiently suppress formation of precipitation in small cloud systems but to invigorate the more intense systems. The energy available for evaporation mainly comes from solar insolation. For the period 1964-1993, considerable (and significant) global dimming is observed. Since the late 1980s a transition from dimming to brightening is observed. Whether the globe is brightening or dimming has important consequences for the hydrological cycle. A major fraction of the reduction or increase in surface solar radiation is balanced by a change in evaporation. On the long term the changed evaporation will have to be balanced by a change in rainfall; consequently the hydrological cycle can become stronger or it spins down. The very few model studies that contain all relevant aerosol-climate interactions, simulated a slow down of the hydrological cycle. From observations the simulated slowing down can not be confirmed. It is essential to understand the reason of the exaggerated (aerosol-induced) slowing down of the simulated hydrological cycle, because future projections are of reduced use if these mechanisms are not well understood. It is likely that in the future atmospheric aerosol concentrations increase over parts of the globe due to increased use of energy in developing regions such as East Asia. Likewise, greenhouse gas concentrations increase and this increase will most likely be stronger than that for aerosols due the long lifetimes of most greenhouse gases. Therefore, we tend to believe that in the future the competing effect of aerosol and greenhouse gases on the hydrological cycle will be such that the hydrological cycle will be intensified .

### Chapter 3

In chapter 3 a detailed analysis of measurements and model calculations of shortwave irradiances at the surface is presented for a set of 18 cases collected during three cloudless days in the Netherlands in 2000. The analysis is focused on the influence of the optical and physical properties of aerosols on simulations of direct and diffuse downward solar irradiance at the surface. The properties of aerosols in the boundary layer are derived from surface measurements, under the assumption that all aerosol is confined to a well-mixed atmospheric boundary layer. The simulations of the irradiances are performed with the state-of-the-art radiative transfer model MODTRAN 4, version 1.1. The analysis reveals no discernable differences between model and measurement for the direct irradiance, but several significant differences for the diffuse irradiance. The model always overestimates the diffuse irradiance measurements by 7 to 44  $\text{Wm}^{-2}$  (average: 25  $\text{Wm}^{-2}$ ). On the basis of an estimated uncertainty in the differences of 18  $\text{Wm}^{-2}$ , it appears that for 13 out of 18 cases the model significantly overestimates the measurements. This number decreases if instrumental errors (e.g. pyranometer zero-offset) and assumptions on the model input (e.g. wavelength-independent surface albedo) are considered. Nevertheless, the analysis presented points to a persistent and significant positive model-measurement difference for the diffuse irradiance, which typically amounts to 1–4% of the top-of-

atmosphere irradiance. In chapter 3 it is suggested that the reason for the discrepancy may be found in the presence of ultrafine absorbing aerosol particles that were not detected by the surface instrument that was measuring aerosol absorption. Another possibility is that these ultrafine particles are not present near the surface, due to dry deposition, but rather higher up in the boundary layer, where they still contribute to the total extinction.

## Chapter 4

In chapter 4, a size dependent parameterization for the removal of aerosol particles by falling rain droplets is developed. Scavenging coefficients are calculated explicitly as a function of aerosol particle size and precipitation intensity including the full interaction of rain droplet size distribution and aerosol particles. The actual parameterization is a simple and accurate three-parameter fit through these pre-calculated scavenging coefficients. The parameterization is applied in the global chemistry transport model TM4 and the importance of below-cloud scavenging relative to other removal mechanisms is investigated for sea salt aerosol. For a full year run (year 2000), we find that below-cloud scavenging accounts for 12% of the total removal of super-micron aerosol. At mid-latitudes of both hemispheres the fractional contribution of below-cloud scavenging to the total removal of super-micron sea salt is about 30% with regional maxima exceeding 50%. Below-cloud scavenging reduces the global average super-micron aerosol lifetime from 2.47 to 2.16 days in our simulations. Despite large uncertainties in precipitation, relative humidity, and water uptake by aerosol particles, we conclude that below cloud scavenging is likely an important sink for super-micron sized sea salt aerosol particles that needs to be included in size-resolved aerosol models.

## Chapter 5

In chapter 5, the aerosol model used in Chapter 4 is further developed for the simulation of aerosol optical depth fields. The model results are compared to observations over Europe for the year 2000. The simulated mean aerosol optical thickness is slightly lower than the observed mean aerosol optical depth. The high spatial variability of water vapor that is not resolved in our model, is suggested as a possible reason for this discrepancy. The relation between aerosol mass and aerosol optical depth is strongly non-linear with respect to water vapor. For perfectly simulated aerosol mass concentrations, the homogeneous distribution of water vapor throughout grid cells thus leads to systematic under prediction of aerosol optical depths. This effect becomes increasingly important for increasing relative humidity. Another possible reason for underestimating mean aerosol optical depth in the model, is the way evaporation is treated. Precipitation formed in the clouds is scaled down to the precipitation that eventually reaches the surface. Implicitly this means that aerosols are released by evaporation in the cloudy environment, where they remain prone to effective removal by in-cloud scavenging. In the real atmosphere much of the evaporation is below the clouds, where the much less effective below-cloud scavenging is responsible for the removal of aerosols. The variance of the simulated aerosol optical depths is smaller than the variance of the observed aerosol optical depths by AERONET. We suggest that also the coarseness of the model grid may contribute to the underestimation. Averaging of aerosol mass concentrations over

large areas levels off the extreme values. Areas with fair weather, which are related to maxima in aerosol optical depth, very often do not cover an entire grid cell. At the boundaries of the grid cells wet deposition then reduces the aerosol mass of the entire grid cell due to mixing. The same holds for aerosol poor areas that always contain fair weather spells.

## Chapter 6

In chapter 6, a working system for the assimilation of aerosol optical depth is developed and applied to ATSR-2 observations retrieved over Europe. On average, the assimilation acts as a source of aerosol mass and aerosol optical depth. This results in a better agreement between the mean simulated (TM4) and observed (AERONET) aerosol optical depths. However, the temporal correlation does not benefit from the assimilation. A possible reason for this may be that the assimilation of aerosol optical depth is not the best way to improve simulated aerosol concentrations, and thus aerosol optical depth. The variability of aerosol optical depth is to large extent caused by the spatial and temporal variability of water vapor. Uncertainties in the water vapor fields may therefore lead to large uncertainties in the simulated aerosol optical depth. A discrepancy between the simulated and assimilated aerosol optical depth, then leads to an adjustment of the aerosol mass. If the simulated aerosol optical depths deviate from the true value because of relative humidity errors instead of biases in the simulate aerosol mass concentration fields, this adjustment is erroneous. The improvement of the model caused by the assimilation is also limited because of the poor quality of the ATSR-2 data. The correlation between all simultaneous AERONET observed and ATSR-2 retrieved aerosol optical depth is negligible (0.03). We demonstrate that the reason for this weak correlation is not the compilation of super-observations from the fine scale observations. The correlation of the  $0.1^\circ \times 0.1^\circ$  data set is also very weak (0.13). We believe that aerosol simulations can benefit from the assimilation of aerosol optical thickness when more accurate observations become available in the future.

## Outlook and recommendations

Atmospheric aerosol concentrations depend heavily on the removal by precipitation (Chapter 4). On the other hand the formation of clouds, the cloud lifetime, and the forming of precipitation is governed by aerosols (Chapter 2). It is not possible to study other aerosol forcings than the aerosol direct effect with an off-line model. The societal impact of changes in precipitation characteristics is arguably larger than the global mean change in temperature. The impact on precipitation and thus the hydrological cycle cannot be investigated with an offline chemistry transport model. For all above reasons, an off-line aerosol model may not be the best way to study the effect of aerosols on climate. Better alternatives would be: 1) to include an aerosol module in a numerical weather prediction model or climate model, or 2) to couple the aerosol model and a numerical weather prediction model or climate model both ways. It is strongly recommended to choose one of the alternatives in future aerosol research.

In the aerosol model developed in this study we take into account interstitial aerosol in a crude manner. We also performed a model run where we neglected the existence of interstitial aerosol (not shown). The result of this exercise was a reduction of the overall aerosol lifetime from 6 to 4 days. We therefore recommend to investigate the formation of interstitial aerosol in the future. First step would be to actually calculate the conversion of cloud water from the water phase to the ice phase and use this conversion to estimate the amount of interstitial aerosol, instead of using climatological values.

To handle the evaporation of rain droplets, precipitation formation rates are scaled with ECMWF surface precipitation in our model. This implicit treatment of evaporation will lead to an underestimation of the aerosol column mass and the aerosol profile will likely have the wrong shape. It is recommended to use precipitation formation fields that are experimentally stored by ECMWF to investigate this issue further.

The coarse model grid used in this study contributed to enlarged uncertainties in the removal mechanism of aerosols and thus in the simulated aerosol mass concentrations (Chapter 4). The coarse model may also have contributed to the underestimation of the mean aerosol optical depth (Chapter 5) via various ways. It is therefore recommended to reduce the model grid to at least  $1^\circ \times 1^\circ$  or less in the future.

The model produces 3D distributions of aerosol mass and aerosol optical depth. To study the direct effect on climate a radiation transport model should be connected to

TM4 so that global and regional forcing estimates become available. This coupling is standard and has been done several times before. It is therefore recommended to do this and perform the calculations.

The model is developed for climatic issues. In principle it is however also possible to use the model for other environmental issues such as air pollution with respect to health. The model can provide back ground concentrations of PM10 or PM2.5. For this purpose it is also necessary to increase the models resolution to at least  $1^{\circ} \times 1^{\circ}$  or less.

# References

- AeroCom, <http://nansen.ipsl.jussieu.fr/AEROCOM/>, global aerosol model Intercomparison, 2005
- Ackerman, A. S., et al., Reduction of tropical cloudiness by soot, *Science*, 288, 1042-1047, 2000
- Agbu, P. M., and M. E. James, The NOAA/NASA pathfinder AVHRR land data set user's manual. Goddard distributed active archive center, NASA, Goddard Space Flight Center, Greenbelt, Md., 1994
- Albrecht, B. A., Aerosols, cloud microphysics, and fractional cloudiness, *Science*, 245, 1227-1230, 1989
- Anderson, G. P., S. A. Clough, F. X. Kneizys, J. H. Chetwynd, and E. P. Shettle, AFGL atmospheric constituent profiles (0-120 km.), *Rep. AFGL-TR-86-0110*, US Air Force, Hanscom Air Force Base, Mass. 01731, 1986
- Andreae, M. O., et al., Smoking rain clouds over the Amazon, *Science*, 303, 1337-1342, 2004
- Andres, R. and A. Kasgnoc, A time-averaged inventory of aerial volcanic sulfur emissions, *J. Geophys. Res.*, 103(D19), 25251-25261, doi:10.1029/98JD02091, 1998
- Ansmann, A., U. Wandinger, A. Wiedensohler, and U. Leiterer, Linderberg Aerosol Characterisation Experiment 1998 (LACE 98): overview, *J. Geophys. Res.*, 107 (D21), 8129, doi: 10.1029/2000JD000233, 2002
- Apituley, A., E. P. Visser, J. B. Bergwerff, J. M. de Winter, H. de Backer, and M. A. F. Allaart, RIVM tropospheric ozone lidar routine measurements, validation and analyses, in *Advances in Atmospheric Remote Sensing*, edited by A. Ansmann et al., pp. 375-378, Springer-Verlag, New York, 1997
- Arking, A., Absorption of solar energy in the atmosphere: Discrepancy between model and observations, *Science*, 273, 779-782, 1996
- Arking, A., Bringing climate models into agreement with observations of atmospheric absorption, *J. Clim.*, 12, 1589-1600, 1999a
- Arking, A., The influence of clouds and water vapor on atmospheric absorption, *Geophys. Res. Lett.*, 26, 2729-2732, 1999b
- Atlas, D., R. C. Srivastava, and R. S. Sekhon, Doppler radar characteristics of precipitation at vertical incidence, *Rev. Geophys.*, 11, 1-35, 1973

- Balkanski, Y. J., D. J. Jacob, and G. M. Gardner, Transport and residence times of tropospheric aerosols inferred from a global three-dimensional simulation of  $^{210}\text{Pb}$ , *J. Geophys. Res.*, 98(D11), 20573-20586, 1993
- Barker, H. W. et al., Assessing 1D atmospheric solar radiative transfer models: Interpretation and handling of unresolved clouds, *J. Clim.*, 16, 2676-2699, 2003
- Bates, T., K. Kelly, J. Johnson, and R., Gammon, Regional and seasonal variations in the flux of oceanic carbon monoxide to the atmosphere, *J. Geophys. Res.*, 100, 23093-23101, 1995
- Bauer, K., R. Conrad, and W. Seiler, CO production höherer pflanzen in natürlichen standorten, *Z. Pflanzenphysiol.*, 94, 219-230, 1979
- Beljaars, A. C. M. and P. Viterbo, Role of the boundary layer in a numerical weather prediction model, in *Clear and cloudy boundary layers*, edited by Holtslag, A. A. M. and P. G. Duynkerke, pp. 287-304, NH-publishers, 1999
- Benkovitz, C., M. Scholtz, J. Pacyna, L. Tarrason, J. Dignon, E. Voldner, P. Spiro, J. Logan and T. Graedel, Global gridded inventories of anthropogenic emissions of sulfur and nitrogen, *J. Geophys. Res.*, 101 (D22), 29239-29253, doi:10.1029/96JD00126 1996
- Berk, A., and co-authors, MODTRAN4 user's manual, Air Force Research Laboratory, Hanscom Air Force Base, Mass, 2000
- Bosilovich, M. G. and S. D. Schubert, Water vapor tracers as diagnostics of the regional hydrological cycle, *J. Hydrometeor.*, 3, 149-165, 2002
- Bouwman, A, D. Lee, W. Ansmann, F van der Hoek, and J. Olivier, A global high-resolution emissions inventory for ammonia, *Glob. Biogeochem. Cycl.*, Vol 11(4), 561-587, 1997
- Bowker, D. E., R. E. Davis, D. L. Myrick, K. Stacy, and W. T. Jones, Spectral reflectances of natural targets for use in remote sensing studies, *NASA Ref. publ.* 1139, 1985
- Box, M. A. and A. Deepak, Atmospheric scattering corrections to solar radiometry, *Applied Optics*, 18 (12), 1941-1949, 1979
- Bush, B. C., F. P. J. Valero, S. A. Simpson, and L. Bignone, Characterization of thermal effects in pyranometers: A data correction algorithm for improved measurements of surface insolation, *J. Atmos. Oceanic. Technol.*, 17, 165-175, 2000
- Cachier, H., Carbonaceous combustion particles, in *Atmospheric particles*, edited by R. M. Harrison and R. E. van Grieken, pp. 295-348, John Wiley, New York, 1998
- Cess, R. D., M. H. Zhang, P. Minnis, L. Corsetti, E. G. Dutton, B. W. Forgan, D. P. Garber, W. L. Gates, J. J. Hack, E. F. Harrison, X. Jing, J. T. Kiehl, C. N. Long, J.-J. Morcrette, G. L. Potter, V. Ramanathan, B. Subasilar, C. H. Whitlock, D. F. Young,

- and Y. Zhou, Absorption of solar radiation by clouds: observation versus models, *Science*, 267, 496-499, 1995
- Cess, R. D., M. H. Zhang, Y. Zhou, X. Jing, and V. Dvortsov, Absorption of solar radiation by clouds: Interpretations of satellite, surface, and aircraft measurements, *J. Geophys. Res.*, 101, 23299-23309, 1996
- Cess, R. D., T. Qian, and M. Sun, Consistency tests applied to the measurement of total, direct, and diffuse shortwave radiation at the surface, *J. Geophys. Res.*, 105, 24881-24887, 2000
- Charlock, T. P. and T. L. Alberta, The CERES/ARM/GEWEX Experiment (CAGEX) for the retrieval of radiative fluxes with satellite data, *Bull. Am. Meteorol. Soc.*, 77, 2673-2683, 1996
- Chylek, P., G. Lesins, G. Videen, J. G. D. Wong, R. G. Pinnick, D. Ngo, and J. D. Klett, Black carbon and absorption of solar radiation by clouds, *J. Geophys. Res.*, 101, 23365-23372, 1996
- Chylek, P., G. Videen, W. Geldart, S. Dobbie, and W. Tso, Effective medium approximation for heterogeneous particles, in light scattering by nonspherical particles, in *Theory, measurements, and geophysical applications*, edited by M. Mishchenko, pp. 273-308, Academic, San Diego, Calif., 2000
- Clarke, A. D., T. Uehara, and J. W. Porter, Atmospheric nuclei and related aerosol fields over the Atlantic: clean subsiding air and continental pollution during ASTEX, *J. Geophys. Res.*, 102, 25281-25292, doi:10.1029/97JD01555, 1997
- Coakley, J. A., Jr., R. L. Bernstein and P. A. Durkee, Effect of shipstack effluents on cloud reflectivity, *Science*, 237, 1020-1022, 1987
- Collins, W. D., P. J. Rasch, B. E. Eaton, B. V. Khattatov, J-F Lamarque, and C. S. Zender, Simulating aerosols using a chemical transport model with assimilation of satellite aerosol retrievals: Methodology for INDOEX, *J. Geophys. Res.*, Vol 106(D7), 7313-7336, 2001
- Conant, W. C., V. Ramanathan, F. P. J. Valero, and J. Meywerk, An examination of the clear-sky solar absorption over the central equatorial Pacific observations versus models, *J. Clim.*, 10, 610-620, 1997
- Conant, W. C., A. M. Vogelmann, V. Ramanathan, The unexplained solar absorption and atmospheric H<sub>2</sub>O: A direct test using clear-sky data, *Tellus Ser. A*, 50, 525-533, 1998
- Cooke, W. F., C. Liousse, H. Cachier, and J. Feichter, Construction of a 1x1 degree fossil fuel emission data set for carbonaceous aerosol and implementation and radiative impact in the ECHAM4-model, *J. Geophys. Res.*, 104, 22137-22162, 1999
- Cox, S. J., W.-C. Wang, and S. E. Schwartz, Climate response to forcings by sulfate aerosols and greenhouse gases, *Geophys. Res. Lett.*, 18, 2509-2512, 1995



- De Rooij, W. A. and C. C. A. H. Van der Stap, Expansion of Mie scattering matrices in generalized spherical functions, *Astron. Astrophys.*, 131, 237-248, 1984
- Dana, M. T. and J. M. Hales, Statistical aspects of the washout of polydisperse aerosols, *Atmos. Environ.*, 10, 45-50, 1976
- Deepak, A. and M.A. Box, Forwardscattering corrections for optical extinction in aerosol media 1: Monodispersions, *Applied Optics*, 17(18), 2900-2908, 1978a
- Deepak, A. and M.A. Box, Forward scattering corrections for optical extinction in aerosol media 1: Polydispersions, *Applied Optics*, 17 (19), 3169-3176, 1978b
- Dentener, F. and P. J. Crutzen, Reaction of N<sub>2</sub>O<sub>5</sub> on tropospheric aerosols: Impact on the global distribution of NO<sub>x</sub>, O<sub>3</sub>, and OH, *J. Geophys. Res.*, 98, 7149-7163, 1993
- Dentener, F., and P. J. Crutzen, A global 3D model of the ammonia cycle, *J. Atmos. Chem.*, 19, 331-369, 1994
- Dentener, F., J. Feichter, and A. Jeuken, Simulation of the transport of Rn222 using on-line and off-line global models at different horizontal resolutions: a detailed comparison with measurements, *Tellus*, 51B, 573-602, 1999
- Deirmendjian, D., Electromagnetic Scattering on Spherical Polydispersions, Elsevier, Amsterdam, pp. 299, 1969
- Dickinson, R. E., Land surface processes and climate – Surface albedos and energy balance. *Advances in Geophysics*, 25, 305-353, 1983
- Dougle P. G. and H. M. Ten Brink, Evaporative losses of ammonium nitrate in nephelometry and impactor measurements, *J. Aerosol Sci.*, 27, S511-S512, 1996
- Dougle P. G., J. P. Veeffkind, and H. M. Ten Brink, Crystallisation of mixtures of ammonium nitrate, ammonium sulphate and soot, *J. Aerosol Sci.*, 29, 375-386, 1998
- Dutton, E. G., J. J. Michalsky, T. Stoffel, B. W. Forgan, J. Hickey, D. W. Nelson, T. L. Alberta, and I. Reda, Measurement of broadband diffuse solar irradiance using current commercial instrumentation with a correction for thermal offset errors, *J. Atmos. Oceanic. Technol.*, 18, 297-314, 2001
- Eck, T. F., B. N. Holben, J. S. Reid, O. Dubovik, A. Smirnov, N. T. O'Neill, I. Slutsker, and S. Kinne, Wavelength dependence of the optical depth of biomass burning, urban and desert dust aerosols, *J. Geophys. Res.*, 104(D24), 31333-31350, 1999
- Engelmann, R.J., The calculation of precipitation scavenging, in *Meteorology and Atomic Energy*, edited by D.H. Slade, U.S. Atomic Energy Commission, 68-60097, 1968
- Erickson, D. J. III and R. A. Duce, On the global flux of atmospheric sea salt, *J. Geophys. Res.*, 93, 14079-14088, 1988

- Erickson, D., Ocean to atmosphere carbon monoxide flux: Global inventory and climate applications, *Glob. Biogeochem. Cycl.*, 3, 305-314, 1989
- Eskes, H., P. van Velthove, P. Valks, and H. Kelder, Assimilation of GOME total ozone satellite observations in a three-dimensional tracer transport model, *Q. J. R. Meteorol. Soc.*, 129, 1663, 2003
- Feichter, J., E. Roecknes, U. Lohmann, and B. Liepert, Nonlinear aspects of the climate response to greenhouse gas and aerosol forcing, *J. Clim.*, 17, 2384-2398, 2004
- Feingold, G., H. Jiang, and J. Y. Harrington, On smoke suppression of clouds in Amazonia, *Geophys. Res. Lett.*, 32, L02804, doi:10.1029/2004GL021369, 2005
- Flowers, E. C., E. L. Maxwell, Characteristics of network measurements, *Sol. Cells*, 18, 205-212, 1985
- Folland, C. K. et al., in *Climate Change 2001: The scientific basis* [Working Group I to the Third Assessment Report of the Intergovernmental Panel on Climate Change (IPCC), Cambridge Univ. Press, Cambridge, 2001], pp. 99-182, 2001
- Fouquart Y., B. Bonnel, and V. Ramaswamy, Intercomparing shortwave radiation codes for climate studies, *J. Geophys. Res.*, 96, 8955-8968, 1991
- Fröhlich, C. and H. Quenzel, Influence of the Sun's aureole on the determination of turbidity, *WMO publication 368*, pp. 538-543, 1974
- Fröhlich, C., and J. London, Revised instruction manual on radiation instruments and measurements, *Tech. Doc. WMO/TD 149*, 140 pp, World Meteorol. Org., Geneva, 1986
- Fröhlich, C., History of solar radiometry and the world radiometric reference, *Metrologia*, 28(3), 111-115, 1991
- Fröhlich, C., R. Philipona, J. Romero, and C. Wehrli, Radiometry at the physikalisch-meteorologisches observatorium Davos and world radiation centre, *Opt. Eng.* 34, 2757-2766, 1995
- Fu, Q., G. Lesins, W. Sun, and J. Higgins, Downward surface diffuse solar irradiances in clear atmospheres: Comparison between model and observations, in *Proceedings of Eighth ARM Science Team Meeting, 23-27 March 1998, Tucson Arizona, DOE/ER0738*, pp. 271-276, U.S. Dep. of Energy, Washington, D. C., 1998
- Gardner, R. M., *ANCAT/EC2 Global aircraft emissions inventories for 1991/92 and 2015: Final Report*, EUR-18179, ANCAT/EC Working Group, ISBN-92-828-2914-6, pp. 84, 1998
- Gelencsér, A., *Carbonaceous Aerosol*, Springer, ISBN 1-4020-2886-5, Dordrecht, The Netherlands, 2004
- Gerber, H. E., Relative-humidity parameterization of the Navy Aerosol Model (NAM), *NRL Report 8956*, Naval Research Laboratory, Washington, D.C., 1985

- Gery, M, G. Whitten, J. Killus, and M. Dodge, A photochemical kinetics mechanism for urban and regional scale computer modelling, *J. Geophys. Res.*, 93, 1477-1486, 1989
- Gilgen, H., M. Wild, and A. Ohmura, Means and trends of short wave irradiance at the surface estimated from global energy balance archive data, *J. Climate*, 11, 2042-2061, 1998
- Gong S.L., L. A. Barrie, and M. Lazare, Canadian aerosol module (CAM): A size-segregated simulation of atmospheric aerosol processes for climate and air quality models 2. Global sea-salt aerosol and its budgets, *J. Geophys. Res.*, 107(D24), 4779, doi:10.1029/2001JD002004, 2002
- Gong, S.L., et al., Canadian Aerosol Module: A size-segregated simulation of atmospheric aerosol processes for climate and air quality models, 1, Module development, *J. Geophys. Res.*, 108(D1), 4007, doi:10.1029/2001JD002002, 2003
- Gong, S.L., A parameterization of sea-salt aerosol source function for sub and super-micron particles, *Global Biogeochem. Cycles*, 17(4), 1097, doi:10.1029/2003GB002079, 2003
- Grassl, H., Possible changes of planetary albedo due to aerosol particles, in *Man's impact of climate*, edited by W. Bach, J. Pankrath, and W. Kellogg, pp. 229-241, Elsevier, 1979
- Guelle, W., Y. J. Balkanski, M. Schulz, F. Dulac, and P. Monfray, Wet deposition in a global size-dependent aerosol transport model 1. Comparison of a 1 year <sup>210</sup>Pb simulation with ground measurements, *J. Geophys. Res.*, 103(D10), 11429-11445, 1998
- Guelle, W., M. Schulz, and Y. Balkanski, Influence of the source formulation on modeling the atmospheric global distribution of sea salt aerosol, *J. Geophys. Res.*, 106(D21), 27509-27524, 2001
- Guenther, A. and et al., A global model of natural volatile organic compound emissions, *J. Geophys. Res.*, 100, 8873-8892, 1995
- Gunn, R. and G.D. Kinzer, The terminal velocity of fall for water droplets in stagnant air, *J. Meteorology*, 6, 243-248, 1949
- Hao, W., M. H. Liu, and P. Crutzen, Estimates of annual and regional releases of CO<sub>2</sub> and other trace gases to the atmosphere from fires in the tropics, based on FAO statistics for the period 1975-1985, in *Fire in the tropical biota-Ecosystems processes and global challenges*, edited by J. G. Goldammer, Springer-Verlag, 1991
- Hao, W. and M. H. Liu, Spatial and temporal distribution of tropical biomass burning, *Glob. Biogeochem. Cycl.*, 8, 495-504, 1994

- Halothore, R. N., S Nemesure, S. E. Schwartz, D. G. Imre, A. Berk, E. G. Dutton, and M. H. Bergin, Models overestimate diffuse clear-sky surface irradiance: A case of excess atmospheric absorption, *J. Geophys. Res.*, 25, 3591-3594, 1998
- Halothore, R. N. and S. E. Schwartz, Comparison of model-estimated and measured diffuse downward irradiance at surface in cloud-free skies, *J. Geophys. Res.*, 105, 20165-21077, 2000
- Hansen A. D. A., and R. C. Schnell, The aethalometer, instrument manual, Magee Sci. Co., Berkeley, Calif., USA, 1991
- Hansen, J. E., M. Sato, and R. Ruedy, Radiative forcing and climate response, *J. Geophys. Res.*, 102(D6), 6831-6864, 1997
- Hansen, J. et al., Climate forcings in Goddard Institute for Space Studies SI2000 simulations, *J. Geophys. Res.*, 107(D18), 4347, doi:10.1029/2001JD001143, 2002
- Hansen, A.D.A., The aethalometer, Magee Sci. Co., Berkeley, Calif., 2002
- Hansen, J. and L. Nazarenko, Soot climate forcing via snow and ice albedo, in *Proceedings of the National Academy of Sciences*, 101(2), pp. 423-428, 2004
- Harrison, L., and J. Michalsky, Objective algorithms for the retrieval of optical depths from ground-based measurements, *Appl. Opt.*, 33, 5126-5132, 1994
- Haywood, J., R. Stouffer, R. Wetherald, S. Manabe, and V. Ramaswamy, Transient response of a coupled model to estimated changes in greenhouse gas and sulfate concentration, *Geophys. Res. Lett.*, 24, 1335-1338, 1997
- Haywood, J. and O. Boucher, Estimates of the direct and indirect radiative forcing due to tropospheric aerosols: A review, *Rev. Geophys.*, 38, 513-543, 2000
- Heimann, M., The global atmospheric tracer model TM2, *Tech. Rep. 10*, Deutsches Klimarechenzentrum, Hamburg, Germany, 1995
- Henning, S., S. Bojinski, K. Diehl, S. Ghan, S. Nyeki, E. Weingartner, S. Wurzler, and U. Baltensperger, Aerosol partitioning in natural mixed-phase clouds, *Geophys. Res. Lett.*, 31, L06101, doi:10.1029/2003GL019025, 2004
- Henzing, J. S., and W. H. Knap, Uncertainty in pyranometer and pyrhelimeter measurements at KNMI in de Bilt, *Tech. Rep TR-235*, 22 pp., Royal Netherlands Meteorological Institute, De Bilt, The Netherlands, 2001
- Henzing J. S., W. H. Knap, P. Stammes, Ten Brink, H. M., G. P. A. Kos, A. Even, D. P. J. Swart, A. Apituley, J. B. Bergwerff, The effect of aerosol on closure of the regional short-wave radiation balance, CLOSAER, *Global change Rep. 410200087*, ISBN 9058510735, Nat. Inst. For Public Health and the Environ., Bilthoven, Netherlands, 2001

- Henzing, J. S., D. J. L. Olivie and P. F. J. van Velthoven, A parametrization of size resolved below cloud scavenging of aerosols by rain, accepted for publication in *ACPD*, acpd-2005-0381, 2005
- Hess, M., P. Koepke and I. Schult, Optical properties of aerosols and clouds: The software package OPAC, *Bull. Amer. Meteorol. Soc.*, 79, 831-844, 1998
- Holben, B. N., T. F. Eck, I. Slutsker, D. Tanre, J. P. Buis, A. Setzer, E. Vermote, J. A. Reagan, Y. J. Kaufman, T. Nakajima, F. Lavenue, I. Jankowiak, and A. Smirnov, AERONET – A federated instrument network and data archive for aerosol characterisation, *Rem. Sens. of the Env.*, 66, 1-16, 1998
- Holtlag, A. A. M. and A. P. Van Ulden, A simple scheme for daytime estimates of the surface fluxes from routine weather data, *J. Clim. and Applied Meteorol.*, 22(4), 517-529, 1983
- Holtlag, A. A. M., and B. A. Boville, Local versus nonlocal boundary-layer diffusion in a global climate model, *J. Climate*, 6, 1825-1842, 1993
- Horvath, H., Experimental calibration for aerosol light absorption measurements using the integrating plate method-summary of the data, *J. of Aerosol Sci.*, 28, 1149-1161, 1997
- Houweling, S., F. Dentener, and J. Lelieveld, The impact of nonmethane hydrocarbon compounds on tropospheric chemistry, *J. Geophys. Res.*, 103, 10,673-10,696, 1998
- IPCC: Climate change 2001: The scientific basis. Contribution of working group I to the third assessment report of the Intergovernmental Panel on Climate Change [Houghton, J.T., Y. Ding, D.J. Griggs, M. Noguer, P.J. van der Linden, X. Dai, K. Maskell, and C.A. Johnson (eds.)]. Cambridge University Press, Cambridge, United Kingdom and New York, NY, USA, 881 pp. (2001)
- Jacob, D. J. et al., Radiative forcing of climate change: Expanding the concept and addressing uncertainties, 207 pp., the national academies press, [www.national-academies.org/basc](http://www.national-academies.org/basc), Washington, D.C., 2005
- Jacobson, M. J., Global direct radiative forcing due to multicomponent anthropogenic and natural aerosols, *J. Geophys. Res.*, 106(D2), 1551-1568, doi:10.1029/2000JD900514, 2001
- Jeuken, A. B. M., H. J. Eskes, P. F. J. van Velthoven, and E.V. Holm: Assimilation of total ozone satellite measurements in a three-dimensional tracer transport model, *J. Geophys. Res.* 104, 5551-5563, 1999
- Jeuken, A. B. M., Evaluation of chemistry and climate models using measurements and data assimilation, Ph.D. Thesis, Technical University of Eindhoven, Netherlands, 2000

- Johnson, B. T., K. P. Shine, and P. M. Forster, The semi-direct aerosol effect: Impact of absorbing aerosols on marine stratocumulus, *Q. J. R. Meteorol. Soc.*, 30, 1407-1422, 2004
- Joshi, M., K. Shine, M. Ponater, N. Stuber, R. Sausen, and L. Li, A comparison of climate response to different radiative forcings in three general circulation models: Towards an improved metric of climate change, *Clim. Dyn.*, 20, 843-854, 2003
- Joss, J., J. C. Thams, and A. Waldvogel, The variation of raindrop size distributions at Locarno, in *Proceedings of Internat. Conf. on cloud physics*, pp. 369-373, 1968
- Kalman, R. H. and Bucy, R. S., New results in linear filtering and prediction theory, *Basic Engineering*, 83D, 95-108, 1961
- Kato, S., T. P. Ackerman, E. E. Clothiaux, J. H. Mather, G. G. Mace, M. L. Wesely, F. Murcray, and J. Michalsky, Uncertainties in modeled and measured clear-sky surface shortwave irradiances, *J. Geophys. Res.*, 102, 25,881-25,898, 1997
- Kettle et al., A global database of sea surface dimethylsulfide (dms) measurements and a method to predict sea surface dms as a function of latitude, longitude and month, *Glob. Biogeochem. Cycl.*, 13, 399-444, 1999
- Kettle, A. and M. Andreae, Flux of dimethylsulfide from the oceans: A comparison of updated data sets and flux models, *J. Geophys. Res.*, 105, 26793-26808, 2000
- Khain, A., A. Pokrovsky, M. Punskey, A. Seifert, and V. Phillips, Simulation of effects of atmospheric aerosols on deep turbulent convective clouds using a spectral microphysics mixed-phase cumulus cloud model. Part 1: Model description and possible applications. *J. Atmos. Sci.*, 61(24), 2963-2983, 2004
- Kiehl, J. T. and K. E. Trenberth, Earth's annual global mean energy budget, *Bull. Amer. Meteorol. Soc.*, 78(2), 197-208, 1997
- Kiehl, J. T., T. L. Schneider, P.J. Rasch, M. C. Barth, and J. Wong, Radiative forcing due to sulfate aerosols from simulations with the National Center for Atmospheric Research Community Climate Model, Version 3, *J. Geophys. Res.*, 105, 1441-1457, 2000
- Kinne, S., R. Bergstrom, O. B. Toon, E. Dutton, and M. Shiobara, Clear-sky atmospheric solar transmission: An analysis based on FIRE 1991 field experiment data, *J. Geophys. Res.*, 103, 19,709-19,720, 1998
- Klein Baltink, H., H. van der Marel, and A. G. A. van der Hoeven, Integrated atmospheric water vapor estimates from a regional GPS network, *J. Geophys. Res.*, 107 (D3), doi: 10.1029/2000JD000094, 2002
- Knap, W. H. and A. Los. Sunphotometry at the Jungfrauoch, in *Activity Report 2003*, Int. Found. High Altitude Res. Stn., Jungfrauoch and Gornergrat, Switzerland, 2004.

- Koelemeijer, R. B. A., P. Stammes, J. W. Hovenier, and J. D. de Haan, A fast method for retrieval of cloud parameters using oxygen A-band measurements from the Global Ozone Monitoring Instrument, *J. Geophys. Res.*, 106, 3475-3490, 2001
- Kreileman, G., Documentation of a geographically explicit dynamic carbon cycle model, *RIVM report*, Natl. Inst. for Public Health and the Environ. (RIVM), Bilthoven, The Netherlands, 1996
- Krol, M. and M. van Weele, Implication of variation of photodissociation rates for global atmospheric chemistry, *Atmos. Environ.*, 31, 1257-1273, 1997
- Kurucz, R. L., The solar irradiance by computation, in *Proceedings of the 17<sup>th</sup> Annual Review Conference on Atmospheric Transmission Models*, edited by G.P. Anderson, R.H. Picard, and J.H. Chetwynd, *Spec. Rep.*, 274, 332 pp., Phillips Lab. Geophys. Dir., Hanscom Air Force Base, Mass., 1995
- Lacis, A. A., J. Chowdhary, M. I. Mischenko, and B. Cairns, Modeling errors in diffuse-sky radiation: Vector vs. scalar treatment, *Geophys. Res. Lett.*, 25, 135-138 1998
- Laws, J.O. and D.A. Parsons, The relationship of raindrop size to intensity, *Trans. AGU*, 24, 452-460, 1943
- Lesins, G., P. Chylek, and U. Lohmann, A study of internal and external mixing scenarios and its effects on aerosol optical properties and direct radiative forcing, *J. Geophys. Res.*, 107, doi:10.1029/2001JD000973, 2002
- Li Z., and L. Moreau, Alteration of atmospheric solar absorption by clouds: simulation and observation, *J. Appl. Meteorol.*, 35, 653-670, 1996
- Liss, P. and L. Merlivat, Air-sea gas exchange rates: Introduction and synthesis, in *The role of sea-air exchange in geochemical cycling*, edited by P. Menard, pp. 113-127, Reidel, Dordrecht, 1986
- Liou, S. C., J. E. Penner, C. Chuang, J. J. Walton, H. Eddleman and H. Cachier, A global three-dimensional model study of carbonaceous aerosols, *J. Geophys. Res.*, 101, 19411-19432, 1996
- Lohmann, U. and J. Feichter, Can the direct and semi-direct aerosol effect compete with the indirect effect on a global scale?, *Geophys. Res. Lett.*, 28, 159-161, 2001
- Marshall, J. S. and W. M. Palmer, The distribution of raindrop with size, *J. Meteorol. Soc.*, 5, 165-166, 1948
- Mätzler, C, Drop-size distributions and Mie computations for rain, *IAP research report, 2002-16*, 2002
- Menon, S., J. Hansen, L. Nazarenko, and Y. Luo, Climate effects of black carbon aerosols in China and India, *Science*, 297, 2250-2253, 2002

- Metzger, S., F. Dentener, S. Pandis, and J. Lelieveld, Gas/aerosol partitioning: 1. A computationally efficient model, *J. Geophys. Res.*, 107(D16), 4312, doi:10.1029/2001JD001102, 2002a
- Metzger, S., F. Dentener, M. Krol, A. Jeuken, and J. Lelieveld, Gas/aerosol partitioning 2. Global modeling results, *J. Geophys. Res.*, 107(D16), 4313, doi:10.1029/2001JD001103, 2002b
- Michalsky J., E. Dutton, M. Rubes, D. Nelson, T. Stoffel, M. Wesley, M. Splitt, and J. DeLuisi, Optimal measurement of surface shortwave irradiance using current instrumentation, *J. Atmos. Oceanic. Technol.*, 16, 55-69, 1999
- Minnen, J., K. K. Goldewijk, and R. Leemans, The importance of feedback processes and vegetation transition in the terrestrial carbon cycle, *J. Biogeogr.*, 22, 805-814, 1996
- Mlawer, E. J., P. D. Brown, S. A. Clough, L. C. Harrison, J. J. Michalsky, P. W. Kiedron, T. Shippert, Comparison of spectral direct and diffuse solar irradiance measurements and calculations for cloud-free conditions, *Geophys. Res. Lett.*, 27, 2653-2656, 2000
- Monahan, E. C., D. E. Spiel, and K. L. Davidson, Model of marine aerosol generation via whitecaps and wave disruption, in *Preprint Volume of 9<sup>th</sup> conference on aerospace and aeronautical meteorology*, American Meteorological Society, Boston, pp 147-152, 1983
- Monahan, E. C., D. E. Spiel, and K. L. Davidson, A model of marine aerosol generation via whitecaps and wave disruption, in *Oceanic Whitecaps*, edited by E. C. Monahan and G. Mac Niocaill, pp 167-174, D. Reidel, Norwell, Mass., 1986
- NASA <http://daac.gsfc.nasa.gov/>, 2001
- Nenes, A., C. Pilinis and S. W. Pandis, ISORROPIA: A new thermodynamic model for multiphase and multicomponent inorganic aerosols, *Aquat. Geochem.*, 4, 123-152, 1998
- Ohmura A., E. Dutton, B. Forgan, C. Fröhlich, H. Gilgen, H. Hegner, A. Heimo, G. König-Langlo. B. McArthur, G. Müller, R. Philipona, R. Pinker, C. H. Whitlock, K. Dehne, and M. Wild, Baseline surface radiation network (BSRN/WCRP), a new precision radiometry for climate research, *Bull. Amer. Meteor. Soc.*, 79, 2115-2136, 1998
- Olivier, J., A. F. Bouwman, C. W. M. van der Maas, J. J. M. Berdowski, C. Veldt, J. P. J. Bloos, A. J. H. Visschedijk, P. Y. J. Zandveld and J. L. Haverlag, Description of EDGAR version2.0: a set of emission inventories of greenhouse gases and ozone-depleting substances for all anthropogenic and most natural sources on a per country and on 1°×1° grid, *RIVM Report nr. 771060002* and *TNO-MEP Report nr. R96/119*, 1996



- Penner, J.E. et al., in Climate Change 2001: The scientific basis [Working Group I to the Third Assessment Report of the Intergovernmental Panel on Climate Change (IPCC), Cambridge Univ. Press, Cambridge, 2001], pp. 289-348, 2001
- Pilewskie, P. and F. P. J. Valero, Direct observations of excess solar absorption by clouds, *Science*, 267, 1626-1629, 1995
- Pinker, R. T., B. Zhang, and E. G. Dutton, Do satellites detect trends in surface solar radiation, *Science*, 308, 850-854, 2005
- Priestley, C. H. B. and R. J. Taylor, On the assessment of surface heat flux and evaporation using large-scale parameters, *Mon. Weather Rev.*, 100(2), 81-92, 1972
- Pruppacher, H. R., and J. D. Klett, Microphysics of clouds and precipitation, 2<sup>nd</sup> Ed., 954 pp., Kluwer Academic Publishers, 1997
- Ramanathan, V, B. Subasiler, G. J. Zhang, W. Conant, R. D. Cess, J. T. Kiehl, H. Grassl, and L. Shi, Warm pool heat budget and shortwave cloud forcing: A missing Physics ?, *Science*, 267, 499-503, 1995
- Ramanathan et al., Indian ocean experiment: An integrated analysis of the climate forcing and effects of the great Indo-Asian haze, *J. Geophys. Res.*, 106(D22), 28371-28398, 2001a
- Ramanathan, V., P. J. Crutzen, J. T. Kiehl, and D. Rosenfeld, Aerosols, climate and the hydrological cycles, *Science*, 294, 2119-2124, 2001b
- Ramaswamy, V. et al., in Climate Change 2001: The Scientific Basis [Working Group I to the Third Assessment Report of the Intergovernmental Panel on Climate Change (IPCC), Cambridge Univ. Press, Cambridge, 2001], pp. 349-416, 2001
- Randles, C. A., L. M. Russell, and V. Ramaswamy, Hygroscopic and optical properties of organic sea salt aerosol and consequences for climate forcing, *Geophys. Res. Lett.*, 31, doi:10.1029/2004GL020628, 2004
- Rasch, P. J. et al., A comparison of scavenging and deposition processes in global models: Results from the WCRP Cambridge workshop of 1995, *Tellus*, 52, 1025-1056, 2000
- Robles González, C, Retrieval of aerosol properties using ATSR-2 observations and their interpretation, PhD Thesis, University Utrecht, The Netherlands, 2003
- Roeckner, E. T., L. Bengtsson, J. Feichter, J. Lelieveld, and H. Rodhe, Transient climate change simulations with a coupled atmosphere-ocean GCM including the tropospheric sulfur cycle, *J. Climate*, 12, 3004-3032, 1999
- Roelofs, G-J and J. Lelieveld, Distribution and budget of O<sub>3</sub> in the troposphere calculated with a chemistry general circulation model, *J. Geophys. Res.*, 100(D10), 20983-20998, 1995

- Rosenfeld, D., Suppression of rain and snow by urban and industrial air pollution, *Science*, 287, 1793-1796, 2000
- Rotstayn, L. D. and J. E. Penner, Indirect aerosol forcing, quasi forcing, and climate response, *J. Clim.*, 14(13), 2960-2975, 2001
- Russell, G. L. and J. A. Lerner, A new finite-differencing scheme for the tracer transport equation, *J. Appl. Meteorol.*, 20, 1483-1498, 1981
- Schulz, M., Y. J. Balkanski, W. Guelle, and F. Dulac, Role of aerosol size distribution and source location in a three-dimensional simulation of a Saharan dust episode tested against satellite-derived optical thickness, *J. Geophys. Res.*, 103(D9), 10579-10592, 1998
- Seinfeld, J. H., S. N. Pandis, Atmospheric chemistry and physics: From air pollution to climate change, John Wiley & Sons, Inc., New York, USA, 1998
- Shettle, E. P., and R.W. Fenn, Models for the aerosols of the lower atmosphere and the effects of humidity variations on their optical properties, *Tech. Rep. AFGL-TR-79-0214*, Air Force Geophys. Lab., Hanscom Air Force Base, Mass, 1979
- Shine, K. P., J. Cook, E. J. Highwood, and M. M. Joshi, An alternative to radiative forcing for estimating the relative importance of climate change mechanism, *Geophys. Res. Lett.*, 30(20), 2047, doi: 10.1029/2003GL018141, 2003
- Simmons, A. J. and D. M. Burridge, An energy and angular-momentum conserving vertical finite-difference scheme and hybrid vertical coordinates, *Mon. Weather Rev.*, 109, 758-766, 1981
- Slinn, S. A. and W. G. N. Slinn, Prediction for particle deposition on natural waters, *Atmos. Environment*, 14, 1013-1016, 1980
- Slinn, W. G. N., Prediction for particle deposition to vegetative canopies, *Atmos. Environment*, 16, 1785-1794, 1982
- Slinn, W. G. N., Precipitation scavenging, in *Atmospheric Science and Power Production*, edited by D. Randerson, *Doc. DOE/TIC-27601*, pp. 466-532, U.S. Dep. of Energy, Washington, D.C., 1984
- Solomon, S., R. W. Portmann, R. W. Sanders, and J. S. Daniel, Absorption of solar radiation by water vapor, oxygen, and related collision pairs in the Earth's atmosphere, *J. Geophys. Res.*, 103, 3847-3858, 1998
- Spiro, P. A., D. J. Jacob, and J. A. Logan, Global inventory of sulfur emissions with  $1^\circ \times 1^\circ$  resolution, *J. Geophys. Res.*, 97, 6023-6036, 1992
- Stamnes, K., S. Tsay, W. Wiscombe, and K. Jayaweera, Numerically stable algorithm for discrete-ordinate-method radiative transfer in multiple scattering and emitting layered media, *Appl. Opt.*, 27, 2502-2509, 1988

- Stanhill, G. and S. Cohen, Global dimming: a review of the evidence for a widespread and significant reduction in global radiation with discussion on its probable causes and possible agricultural consequences, *Agric. For. Meteorol.*, 107, 255-278, 2001
- Stanhill, G., Global dimming: a new aspect of climate change, *Weather*, 60, 11-14, 2005
- Stocker, T. F. et al., in Climate Change 2001: The scientific basis [Working Group I to the Third Assessment Report of the Intergovernmental Panel on Climate Change (IPCC), Cambridge Univ. Press, Cambridge, 2001], pp. 417-470, 2001
- Sunesson, A., A. Apituley, D. P. J. Swart, Differential absorption lidar system for routine monitoring of tropospheric ozone, *Appl. Opt.*, 33, 7045-7058, 1994
- Swietlicki, E., J. Zhou, D. S. Covert, K. Hameri, B. Busch, M. Vakeva, U. Dusek, O. H. Berg, A. Wiedensohler, P. Aalto, J. Mäkelä, B. G. Martinsson, G. Papaspiropoulos, B. Mentes, G. Frank, and F. Stratmann, Hygroscopic properties of aerosol particles in the north-eastern Atlantic during ACE-2, *Tellus*, 52B, 201-227, 2000
- Tegen, I, P. Hollrig, M. Chin, I. Fung, D. Jacob, and J. E. Penner, Contribution of different aerosol species to the global aerosol extinction optical thickness: Estimates from model results, *J. Geophys. Res.*, 102, 23895-23915, 1997
- Ten Brink H. M., J. P. Veeffkind, A. Waijers-Ijpelaan, and J. C. van der Hage, Aerosol light-scattering in the Netherlands, *Atmos Environ.*, 30, 4251-4261, 1996
- Ten Brink H. M., A. Khlystov, G. Kos, T. Tuch, C. Roth, W. Kreyling, A high-flow humidograph for testing the water uptake by ambient aerosol, *Atmos. Environ.*, 34, 4291-4300, 2001
- Textor, C., M. Schulz, S. Guibert, S. Kinne, Y. Balkanski, S. Bauer, T. Berntsen, T. Berglen, O. Boucher, M. Chin, F. Dentener, T. Diehl, R. Easter, H. Feichter, D. Fillmore, S. Ghan, P. Ginoux, S. Gong, A. Grini, J. Hendricks, L. Horowitz, P. Huang, I. Isaksen, T. Iversen, S. Kloster, D. Koch, A. Kirkevåg, J. E. Kristjansson, M. Krol, A. Lauer, J. F. Lamarque, X. Liu, V. Montanaro, G. Myhre, J. Penner, G. Pitari, S. Reddy, Ø. Seland, P. Stier, T. Takemura, and X. Tie, Analysis and quantification of the diversities of aerosol life cycles within AeroCom, *Atmos. Chem. Phys. Discuss.*, 5, 8331-8420, 2005
- Thiebaux, H. J., Anisotropic correlation functions for objective analysis, *Mon. Weather Rev.*, 104, 994-1002, 1976
- Tiedtke, M., A comprehensive mass flux scheme for cumulus parameterization in large-scale models, *Mon. Weather Rev.*, 117, 1779-1800. 1989
- Trenberth, K. E., Atmospheric moisture residence times and cycling: Implications for rainfall rates with climate change, *Climatic Change*, 39, 667-694, 1998
- Trenberth, K. E., Atmospheric moisture recycling: Role of advection and local evaporation, *J. Climate*, 12, 1368-1381, 1999a

- Trenberth, K. E., Conceptual framework for changes of extremes of the hydrological cycle with climate change, *Climatic Change*, 42, 327-339, 1999b
- Trenberth, K. E., A. Dai, R. M Rasmussen, and D. B. Parsons, The changing character of precipitation, *Bull. Amer. Met. Soc.*, doi:10.1175/BAMS-84-9-1205, 2003
- Twomey, S., Pollution and the planetary albedo, *Atmos. Env.*, 8, 1251-1256, 1974
- United Nations: The United Nations energy statistics database (1991). *Tech. Rep. Stat. Div.*, New York, 1993
- Valero P. J., and B. C. Bush, Measured and calculated clear-sky solar radiative fluxes during the Subsonic Aircraft Contrail and Cloud Effects Special Study (SUCCESS), *J. Geophys. Res.*, 104, 27387-27398, 1999
- Van Aardenne, J., F. Dentener, J. Olivier, C. K. Goldewijk, and J. Lelieveld, A 1° x 1° resolution data set of historical anthropogenic trace gas emissions for the period 1890- 1990, *Glob. Biogeochem. Cycl.*, 15(4), 909-928, 2001
- Van Pul, W. A. J., A. A. M. Holtslag, and D. P. J. Swart, A comparison of ABL heights inferred routinely from lidar and radiosondes at noontime, *Boundary layer meteorology*, 68, 173-191, 1994
- Veefkind, J. P., J. C. H. van der Hage, H. M. Ten Brink, Nephelometer derived and directly measured aerosol optical depth of the atmospheric boundary layer, *Atmos. Res.*, 41, 217-228, 1996
- Veefkind, J. P. and G. de Leeuw, A new algorithm to determine the spectral aerosol optical depth from satellite radiometer measurements, *J. Aerosol Science*, 29(10), 1237-1248, 1998
- Veefkind, J. P., G. de Leeuw, and P. A. Durkee, Retrieval of aerosol optical depth over land using two-angle view satellite radiometry during TARFOX, *Geophys. Res. Lett.*, 25, 3135-3138, 1998
- Volz, F. E., Infrared refractive index of atmospheric aerosol substances, *Applied Optics*, 11, 755-759, 1972
- Vignati, E., G. de Leeuw, and R. Berkowicz, Modeling coastal aerosol transport and effects of surf-produced aerosols on processes in the marine atmospheric boundary layer., *J. Geophys. Res.*, 106(D17), 20225-20238, 2001
- Vogelezang, D. H. P. and Holtslag, A. A. M., Evaluation and model impacts of alternative boundary-layer height formulations, *Bound.-Layer Meteor.*, 81, 245-269, 1996
- Walton, J. T., M. C. MacCracken, and S. J. Ghan, A global-scale lagrangian trace species model of transport, transformation, and removal processes, *J. Geophys. Res.*, 93(D7), 8339-8354, 1988

Wang, W.-C., M. Dudek, and X-Z. Liang, Inadequacy of effective CO<sub>2</sub> as a Proxy in assessing the regional climate change due to other radiatively active gases, *Geophys. Res. Lett.*, 19, 1375-1378, 1992

Wardle, D., L. Dahlgren, K. Dehne, L. Liedquist, L. McArthur, Y. Miyake, O. Motschka, C. Velds, and C. Wells, Improved measurement of solar irradiance by means of detailed pyranometer characterization, Solar heating and cooling program Task 9, *Rep. IEA-SHCP-9C-2*, 217 pp. International Energy Agency, 1996

WCP-55., World Climate Program research report of the experts meeting on aerosols and their climatic effects. Williamsburg, Virginia, 28-30 March 1983, edited by A. Deepak and H. E. Gerber, 107 pp., 1983

Wendisch, M., A. Keil, D. Mueller, U. Wandinger, P. Wendling, A. Stifter, A. Petzold, M. Fiebig, M. Wiegner, V. Freudenthaler, W. Armbruster, W. von Hoyningen-Huene, and U. Leiterer, Aerosol-radiation interaction in the cloudless atmosphere during June 98, 1. Measured and calculated broadband solar and spectral surface insulations, *J. Geophys. Res.*, 107(D21), 8124, doi:10.1029/2000JD000226, 2002

Wesely, M. L., Parameterization of surface resistances to gaseous dry deposition in regional-scale numerical models, *Atmos. Environ.*, 23, 1293-1304, 1989

Wild, M., A. Ohmura, H. Gilgen, and E. Roeckner, Validation of general circulation model radiative fluxes using surface observations, *J. Clim.*, 8, 1309-1324, 1995

Wild, M., Discrepancies between model-calculated and observed shortwave atmospheric absorption in areas with high aerosol loadings, *J. Geophys. Res.*, 104, 27,361-27,371, 1999

Wild, M., H. Gilgen, A. Roesch, A. Ohmura, C. N. Long, E. G. Dutton, B. Forgan, A. Kallis, V. Russak, and A. Tsvetkov, From dimming to brightening: decadal changes in solar radiation at Earth's surface, *Science*, 308 847-850, 2005

Wilson R. and J. D. Spengler, *Particles in our air: concentrations and health effects*. Cambridge, MA: Harvard University Press, pp. 212, 1996

WMO, Guide to meteorological instruments and methods of observation, *Rep. WMO ISO 9060*, fifth edition, Geneva, Switzerland, 1983

WMO, Guide to meteorological instruments and methods of observation, *WMO-TR 8*, 6<sup>th</sup> edition, Geneva, Switzerland, 1996

de Wolf, D.A., On the Laws-Parsons distribution of raindrop sizes, *Radio Science*, 36, 639-642, 2001

Wyzga, E. R. Air pollution and health; are particulates the answer? In *Proceedings of the NETL Conference: PM<sub>2.5</sub> and electric power generation: recent finding and implications*, Pittsburgh, PA April 9-10, 2002

---

Yienger, J and H. Levy, Global inventory of soil-biogenic  $\text{no}_x$  emissions, *J. Geophys. Res.*, 100, 447-464, 1995

Young, A, T, Air mass and refraction, *Applied Optics*, 33(6), 1108-1110, 1994



# List of acronyms and abbreviations

<b>AeroCom</b>	global Aerosol model interComparison
<b>AERONET</b>	Aerosol RObotic NETwork, network of sunphotometers
<b>AOD</b>	Aerosol Optical Depth
<b>ATSR</b>	Along Track Scanning Radiometer
<b>AVHRR</b>	Advanced Very High Resolution Radiometer
<b>BC</b>	Black Carbon
<b>CCN</b>	Cloud Condensation Nuclei
<b>CLOSAeR</b>	The CLOSAeR project aimed to study the effects of aerosol on closure of the regional short-wave radiation balance in the Netherlands.
<b>CTM</b>	Chemistry Transport Model
<b>DNSI</b>	Direct Normal Solar Irradiance
<b>ECMWF</b>	European Centre for Medium-range Weather Forecasts
<b>ECN</b>	Energieonderzoek Centrum Nederland
<b>EQSAM</b>	simplified thermodynamic equilibrium aerosol model
<b>GCM</b>	General Circulation Model
<b>ICRCCM</b>	InterComparison of Radiation Codes used in Climate Models
<b>IN</b>	Ice Nuclei
<b>IPCC</b>	Intergovernmental Panel on Climate Change
<b>KNMI</b>	Koninklijk Nederlands Meteorologisch Instituut
<b>MMA</b>	March + May + August
<b>MODTRAN</b>	spectral band radiation transfer model with moderate spectral resolution
<b>NIR</b>	Near InfraRed electromagnetic radiation
<b>PM10</b>	Aerosol particles with aerodynamic diameter less than 10 micrometer
<b>OC</b>	Organic Carbon
<b>RH</b>	Relative Humidity
<b>RIVM</b>	RijksInstituut voor Volksgezondheid en Milieu
<b>RMS</b>	Root-Mean-Square
<b>RTM</b>	Radiation Transport Model
<b>SAR</b>	Second Assessment Report of the IPCC
<b>SIA</b>	Secondary Inorganic Aerosol
<b>SOA</b>	Secondary Organic Aerosol
<b>SPUV</b>	SunPhotometer (Ultra Violet)
<b>TAR</b>	Third Assessment Report of the IPCC
<b>TM4</b>	global chemistry Transport Model version 4
<b>TNO</b>	Nederlandse Organisatie voor toegepast-natuurwetenschappelijk onderzoek
<b>TNO-D&amp;V</b>	TNO Defensie en Veiligheid
<b>TOA</b>	Top Of Atmosphere
<b>VIS</b>	VISible electromagnetic radiation
<b>WMO</b>	World Meteorological Organization
<b>WRC</b>	World Radiation Centre
<b>WRR</b>	World Radiometric Reference
<b>WSG</b>	World Standard Group (of various radiometers)





# Dankwoord

Dit boekje is mede totstandgekomen door de betrokkenheid van vele mensen. Al deze mensen wil ik graag bedanken, een aantal mensen in het bijzonder.

Door mijn ouders ben ik de persoon geworden die ik ben. Al op jonge leeftijd kreeg ik alle vrijheid om uit te zoeken hoe ik mijn leven het liefst zou willen leiden. Hierdoor werd de onderzoeker in mij geboren. Mamma en Pa, ontzettend bedankt.

Als kind wilde ik jong vader worden. Meegenomen dat jonge vaders steeds ouder worden, is dat uitgekomen. Zonder Luc en Nena kan ik me geen zinvol leven meer voorstellen. Zij hebben natuurlijk niet bijgedragen aan dit proefschrift. Misschien horen ze ook niet in dit dankwoord, maar ze horen wel bij mij.

Grote dank ben ik ook verschuldigd aan mijn vriendin en vrouw, Caroline. Op een cruciaal moment, ergens halverwege mijn promotie, zorgde zij ervoor dat ik me realiseerde dat ik van mijn hobby mijn werk heb mogen maken (eerlijk, ik ken niemand die liever naar zijn of haar werk gaat dan ikzelf). Caroline, bedankt voor alles, en dat is meer dan jij vermoedelijk denkt.

Als laatste van mijn dierbaren wil ik mijn klimvrienden bedanken. De avonturen die wij beleefden in de Alpen, de Himalaya en de Karakoram waren een essentieel onderdeel van mijn promotie; afstand nemen is noodzaak om kritisch te blijven ten aanzien van je eigen werk.

Een promotie is niet mogelijk zonder promotoren en copromotor. Hennie Kelder ben ik bovenal dank verschuldigd voor de geboden kans en het bewaken van de tijdsplanning. Mijn copromotor Peter van Velthoven, wil ik graag bedanken voor het zinvolle commentaar op alle papers, posters, presentaties en hoofdstukken van dit proefschrift. Peter ook bedankt voor het zoeken naar de financiële middelen die overbrugging tussen twee projecten mogelijk maakte en voor de enorme onderzoeksvrijheid, een vrijheid die zeker niet vanzelfsprekend is als je bent aangenomen op projecten.

Rob van Dorland en Aad van Ulden, bedankt voor de vele discussies die hebben bijgedragen tot de totstandkoming van hoofdstuk twee van dit proefschrift. Piet Stammes, bedankt voor de geboden bescherming in mijn eerste KNMI jaren, je engelengeduld en je aandacht voor de mens achter de werknemer. Wouter Knap, bedankt dat ik altijd bij je binnen kon lopen met de meest ingewikkelde vragen. Dirk Olivié, als oud-kamergenoot wil ik je bijzonder bedanken voor alle tijd die je stopte in mijn onderzoek, terwijl jij zelf in tijdnood zat.

Mijn collega's van het KNMI wil ik bedanken voor alle prettige lunches, koffie pauzes en discussies over werk en wereld. Tenslotte wil ik de tuinmannen en de architecten van de KNMIgebouwen en -tuinen bedanken, omdat ik tijdens bezoeken aan projectpartners in binnen- en buitenland nooit een betere werkplek heb gezien.



# Curriculum vitae

Op 7 november 1973 ben ik geboren in de gemeente Alkemade. Nadat Joop Zoetemelk de Tour won, mocht ik in 1980 eindelijk naar de grote school. Het belangrijkste dat me is bij gebleven van al die jaren op de Gerardus school, is dat schooldagen te kort waren, dat het altijd te langzaam ging, dat er voor, tijdens en na schooltijd te weinig gevoetbald kon worden en dat ik ervan overtuigd was dat mijn vrienden altijd mijn vrienden zouden blijven. Toen ik de littekens, voor de rest van mijn leven, op mijn enkels schaatste, won Evert van Benthum de elfstedentocht; ik mocht niet mee, ik was te klein. Daarna begon het zoeken naar een middelbare school. Mijn oog was gevallen op de vierde vrouw van Willem van Oranje. De eerste twee jaar had ik geen tijd om huiswerk te maken. Er kon immers weer volop geschaatst worden (met weer die Van Benthum), ik moest voetballen, want ik werd nog steeds profvoetballer, ik deed aan turnen en hardlopen en ik fietste minstens 200 kilometer per week, maar dat mocht geen naam hebben. In het weekend was het flink aanpoten want ik moest een vuurtorentje kopen en er moest geïnvesteerd worden in de Amerikaanse dollar die historisch laag stond, helaas. Toen ik ongeveer 16 jaar was, stond de wereld op zijn kop, ik werd toch geen profvoetballer. Sneeuw had meer aantrekkingskracht dan gras. Ik werkte me het schompes om een alpiene uitrusting aan te kunnen schaffen en vertrok naar Oostenrijk. De wereld zou nooit meer hetzelfde zijn. Het atheneum rondde ik in 1992 succesvol af. Het belangrijkste dat me is bij gebleven van al die jaren op de Louise de Coligny, is dat mijn vrienden altijd mijn vrienden zullen blijven, zeker nadat we samen de perestrojka en glasnost van dichtbij meemaakten. Ik werd dus geen profvoetballer en ik had er nooit bij stilgestaan dat ik dan iets anders moest worden. Ik had geen 10 gehaald voor mijn scheikunde en economie examens, dus ging ik in 1992 natuurkunde studeren in Utrecht, want dan kon je nog iets met ijs en klimaat doen. Plotseling was ik iets, ik was bergbeklimmer en sociaal want ik woonde in een huis waar dak- en thuislozen een jaartje hun leven op de rails konden brengen. Het is verbazingwekkend dat ik in 1999 afstudeerde in de Meteorologie en Fysische Oceanografie terwijl er zoveel mooie bergen in de Alpen en de rest van de wereld zijn. In 2000 kwam ik als onderzoeker op het KNMI terecht. Ik wist dat alles wat ik tot nu toe in mijn leven had gedaan juist was geweest; hier was ik voor gemaakt. Toen kwam er weer iets anders voor de rest van mijn leven, mijn vriendin en ik werden een paar, een stel met een kind en vervolgens een heus gezin met een eigen huis. Mijn wilde haren raakte ik niet allemaal kwijt maar ik werd wel volwassen. Nu verlies ik 6 maart ook nog een letter van mijn titel als alles even meezit. Ik zit er niet mee. Het leven lacht mij toe.